

Dissertation
submitted to the
Combined Faculties for the Natural Sciences and for Mathematics
of the Ruperto-Carola University of Heidelberg, Germany
for the degree of
Doctor of Natural Sciences

presented by
Diplom-Physicist Thomas Fucke
born in Kiel, Germany
Oral examination: 17th October 2007

Biophysical Characterization and Simulation of Neocortical Layer 2/3 Pyramidal Neurons during Postnatal Development

Referees:

Prof. Dr. Bert Sakmann

Prof. Dr. Karl-Heinz Meier

Biophysikalische Charakterisierung und Simulation von Schicht 2/3

Pyramidenzellen in der Hirnrinde während der postnatalen Entwicklung

Pyramidenzellen der Schicht 2/3 sind der häufigste Zelltyp in der Hirnrinde (Neokortex) von Säugetieren. Trotzdem ist über ihre biophysikalischen Eigenschaften bisher wenig bekannt. In dieser Doktorarbeit wurden grundlegende Eigenschaften von Pyramidenzellen der Schicht 2/3 von 1 bis 6 Wochen alten Ratten untersucht. Hierzu wurden elektrophysiologische Messungen *in vitro* mit morphologischen Rekonstruktionen und numerischen Rechnersimulationen kombiniert. Insbesondere sollten in dieser Arbeit die Ionenkanäle, die den unterschweligen integrativen Eigenschaften dieser Zellen zugrundeliegen, und die Entwicklung der Kanalexpression bestimmt werden. Ein simulierter Erstarrungs-Algorithmus wurde eingesetzt um valide Modelle unterschiedlichen Komplexitätsgrades zur Reproduktion experimenteller Daten zu erstellen.

Zu allen Altern zeigten Schicht 2/3 Pyramidenzellen deutliche anomale Rektifizierung, die aufgrund pharmakologischer Experimente und aufgrund Simulationen auf einwärts-rektifizierende Kaliumkanäle (KIR) zurückzuführen war. Nur ein geringer hyperpolarisations-aktivierter Strom (I_h) wurde gefunden, sehr im Gegensatz zu anderen Pyramidenzelltypen. Während morphologische Veränderungen bis zur zweiten postnatalen Woche abgeschlossen waren, änderten sich die biophysikalischen Eigenschaften weiterhin bis Woche 4-6. Insbesondere der Eingangswiderstand sank mit steigendem Alter, wodurch die Zellen im reifenden kortikalen Netzwerk weniger erregbar wurden. In Computersimulationen hatten diese Eigenschaften starken Einfluss auf die Integration synaptischen Eingangs während spontaner *in vivo* Aktivität. Daraus kann geschlossen werden, dass Schicht 2/3 Pyramidenzellen biophysikalische Eigenschaften besitzen, die sich deutlich von denen anderer Pyramidenzelltypen unterscheiden, und dass die verhältnismäßig lange postnatale Entwicklung kritisch für die Entwicklung synaptischer Integration und kortikaler Aktivität *in vivo* ist.

Biophysical Characterization and Simulation of Neocortical Layer 2/3

Pyramidal Neurons during Postnatal Development

Pyramidal neurons in layer 2/3 of the mammalian neocortex constitute the most abundant neocortical cell type, yet their biophysical properties are still poorly understood. In this thesis, fundamental properties of layer 2/3 pyramidal neurons of 1-to-6-weeks old rats were investigated with an approach combining *in vitro* electrophysiological characterization, reconstruction of cell morphologies, and numerical computer simulations. A specific goal was to identify ion channel mechanisms underlying the sub-threshold integrative properties of these cells and to reveal the developmental profile of channel expression. A simulated annealing algorithm was employed to numerically simulate layer 2/3 neurons and to generate valid models of varying complexity and constrained by experimental data.

At all ages, layer 2/3 pyramidal neurons showed prominent anomalous rectification which could be attributed to inward-rectifier potassium (KIR) channels based both on pharmacological experiments and modeling. In contrast to other types of pyramidal neurons little hyperpolarization-activated current (I_h) was found. While morphological development essentially was complete at postnatal week 2, biophysical properties continued to change until week 4-6. In particular, input resistance strongly decreased with age, rendering the cells less excitable as the cortical network matures. Computer simulations showed that these properties will have a large impact on the integration of synaptic inputs during ongoing spontaneous activity *in vivo*. It is concluded, that layer 2/3 pyramidal neurons possess biophysical properties distinct from other pyramidal cells and that the prolonged postnatal development is critical for shaping synaptic integration and neocortical circuit activity *in vivo*.

Contents

1 Introduction

1.1 The mammalian neocortex	1
1.1.1 Laminar organization	2
1.1.2 Concepts of neuronal signaling	5
1.1.3 Neurons under <i>in vivo</i> conditions	7
1.1.4 Development	8
1.2 The L2/3 pyramidal neuron	10
1.2.1 Morphology	10
1.2.2 Electrophysiological properties	12
1.2.3 Input and output	14
1.3 Biophysics of neuronal computation	15
1.3.1 The passive cable equation	15
1.3.2 Voltage-dependent ion channels	17
1.4 Specific goals of this study	22

2 Experiments

2.1 Experimental methods	24
2.1.1 Electrophysiology	24
2.2.2 Data analysis	29
2.2 Experimental results	32
2.2.1 Morphological changes during development	32
2.2.2 Sub-threshold properties of L2/3 pyramidal cells	37
2.2.3 Supra-threshold properties of L2/3 pyramidal cells	42
2.2.4 Pharmacological Experiments	46
2.3 Discussion	54
2.3.1 Biophysical properties and development of L2/3 pyramidal neurons	54
2.3.2 KIR mediates anomalous rectification	59

2.3.3	Hodgkin-Huxley-fit to I-V curves	61
3	Modeling	
3.1	Modeling methods	66
3.1.1	Voltage-dependent ion channels	66
3.1.2	Compartmental modeling	69
3.1.3	Automated parameter search	71
3.1.4	Simulating UP/DOWN-states	78
3.2	Modeling results	79
3.2.1	Testing the simulated annealing (SA) algorithm	80
3.2.2	Reproduction of experimental data	84
3.2.3	Full morphology models	91
3.2.4	Simulation of <i>in vivo</i> activity	96
3.3	Discussion	100
3.3.1	Automated parameter search by simulated annealing	100
3.3.2	Age-dependent L2/3 pyramidal cell model	102
3.3.3	UP- and DOWN-states	105
3.3.4	Expanding the model towards supra-threshold behavior	106
4	Conclusion and Outlook	110
5	References	113
6	Acknowledgments	131
7	List of Abbreviations	132

1 Introduction

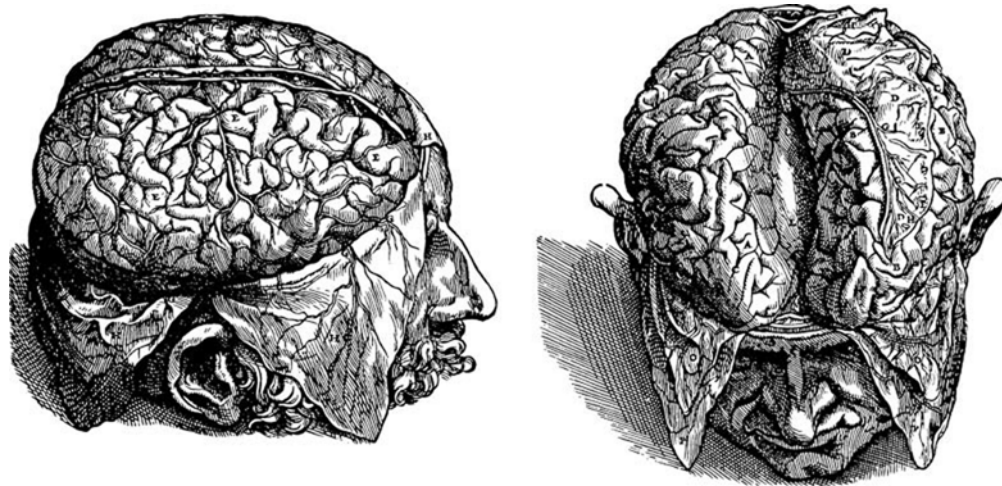
During the last century, a growing number of scientists from all disciplines have become interested in the field of biological neuroscience. Besides more practical results like the better understanding of neurological and mental diseases on the cellular and molecular level, the ultimate driving force for the neuroscientific research field is the expectation that by understanding the biological mechanisms in the brain, one might one day understand what makes the human being “tick”, i.e. what the biological basis is of emotions, percepts, attention, qualia and consciousness. Paradoxically, the object of interest –the human brain – is the very organ that allows the scientist to perform his research and in the end the question remains whether the human brain will be able to truly understand itself.

For ethical considerations, of course, experiments on the cellular level cannot simply be performed in humans (with the few exceptions of patients undergoing brain surgery). Thus, most knowledge about neuronal mechanisms in the brain has been inferred from central nervous systems (CNS) of other organisms. Depending on the question at hand, the complexity of the model organism may vary, ranging from very simple animals like the fruit fly *Drosophila melanogaster*, the sea snail *Aplysia californica* and the worm *Caenorhabditis elegans* over amphibians like *Xenopus laevis*, fish (zebrafish) and birds (zebra finch) to mammals up to our next evolutionary relatives, the primate monkey. For the purpose of this study, the rat (*Rattus norvegicus*) with its well characterized CNS has been chosen as the appropriate model system to investigate the mammalian brain in general and a specific cell type in the neocortex in particular.

In this introductory part of the thesis an overview of the research topic will be given. During the following chapters, neuroscientific terms will be explained *en passant* for those readers who are not familiar with the topic’s terminology. A list of abbreviations can be found at the end of this thesis.

1.1 The mammalian neocortex

The neocortex is a structure common to all mammals although similar structures are at least partly present in other vertebrates. It can also be considered the brain structure defining us as humans since *homo sapiens* seems to be the animal with the best developed neocortex in respect to cortical versus total brain volume. The term *neocortex* stems from its being relatively young in evolutionary terms.



Copyright © 2002, Elsevier Science (USA). All rights reserved.

Fig. 1.1 Historical drawing of the human brain (1543, by Andreas Vesalius). Taken from Squire et al., 2003.

1.1.1 Laminar organization

In the mammalian brain, the neocortex is a shell-like structure of a few millimeters thickness engulfing most of the cerebrum. In humans as well as in other primates it is heavily folded, with its outer appearance reminiscent of a walnut. The structure of the surface, although appearing random, is conserved from brain to brain within a species. Anatomical and functional studies of the neocortex date back to the works of Santiago Ramon y Cajal (Nobel prize in 1906), who described cellular structures and anatomical organization of cortical tissue in great detail (reprinted in Ramon y Cajal, 1995).

The neocortex contains a variety of cell types. A common feature of neurons is their general structure: From a cell body (soma) several thin protrusions stretch out into the surrounding tissue. These thin structures of which neurons often grow several are termed dendrites. In addition, each neuron possesses one axon, which establishes the connections to target neurons. While dendrites stretch out from the soma a few millimeters at most, axons can become meters in length. Both structures often show pronounced arborizations, which have characteristic morphological features in different neuronal subtypes and thus allow distinguishing cell types.

Neocortex comprises six laminar layers

In stained tissue a clear organization of the neocortex into layers with different cell types and of different packing densities is obvious. In most cortical areas there are six layers (Brodmann, 1909). Nomenclature simply numbers them, starting at the pial surface of the cortex. Layer 1 (L1), the most superficial layer, contains few neurons, but axonal and dendritic structures. The two next layers, L2 and L3, are often not clearly distinguishable and combined to one layer, L2/3. The largest population of L2/3 cells consists of pyramidal cells, named after their pyramid-shaped somata. Pyramidal cells show two classes of dendrites: (1) the basal dendrites that originate from the base of the pyramid-shaped soma and reaching out within the same layer; (2) the apical dendrite that originates from the pyramid's tip and often crosses all layers to the pia. In most cases, the apical dendrite shows a tree-like structure, with a trunk from which only few, so-called oblique dendrites stretch out, and a spreading terminal tuft with thin distal branches in L1. The majority of excitatory cells in L4, in contrast, are more isotropic in their distribution of dendrites, hence their name "spiny stellate cells". Finally, the two deepest layers, L5 and L6, host the largest cells in the neocortex,

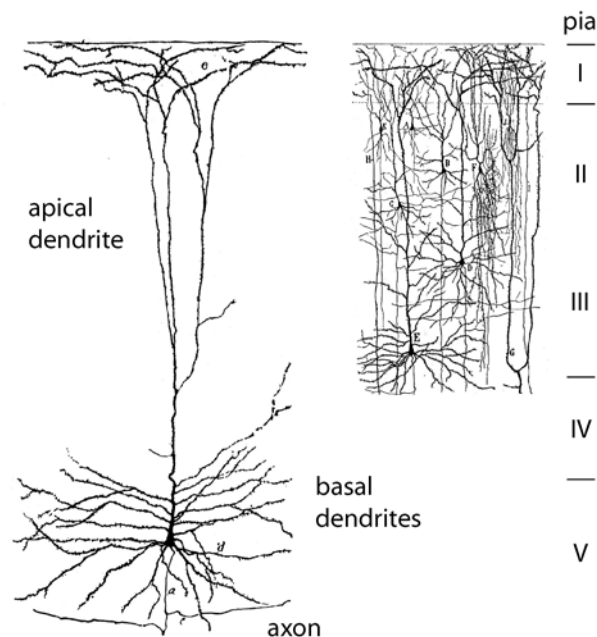


Fig. 1.2 Drawings of cortical neurons from Cajal. Left, single pyramidal cell from layer 5. Right, layers 1-3 with heavily intertwined dendritic trees of pyramidal cells. Note that only a small fraction of cells is actually stained. (Figure adapted from Ramon y Cajal, 1995).

again pyramidal cells. In between all of these excitatory neurons one finds a wide range of inhibitory interneurons of different shapes and electrophysiological behavior. In general, interneurons mediate inhibition on a rather local spatial scale due to constrained axonal extension (Ahissar & Kleinfeld, 2003; Buzsaki et al., 2004; Somogyi & Klausberger, 2004; Yuste, 2005).

In addition to neurons involved in signal processing all layers contain additional cell types called glial cells. This class of cells comprises astrocytes, oligodendrocytes, and microglial cells. They are responsible for supporting neurons and repairing damage that the organism's immune system cannot reach due to the blood-brain barrier (Nimmerjahn et al., 2005). They also might be involved in slow modulation of neuronal activity (Hirrlinger et al., 2004).

Other principles of cortical organization

In addition to the laminar structure, other structural features have been identified on different spatial scales:

Columns: In addition to the laminar organization a vertical organization of the neocortex into so-called radial columns has been found (Mountcastle, 1957; Hubel & Wiesel, 1962). Anatomical proof for a columnar organization of the brain is sparse, however, except in a few somato-sensory areas, such as the so-called barrel cortex of rodents, which is associated with the snout whiskers (Woolsey & Van der Loos, 1970). Most importantly, the cortical column is considered a functional unit for cortical processing with the idea that similar local neuronal circuits with similar processing capacities repeat themselves across the heavily interconnected neocortex.

Areas: Already about a hundred years ago it was suggested that certain brain areas are responsible for well defined sensations, movements, or mental tasks (Brodmann, 1909). Recent studies, using functional magnetic resonance tomography (fMRI), revealed in greater detail which parts of the neocortex are active during specific tasks (Shibasaki, 1993; Ashe & Ugurbil, 1994; Ungerleider, 1995). For the somato-sensory cortex and the motor areas a clear topographic organization is present for which the concept of the homunculus was introduced (Penfield & Rasmussen, 1950). As the somato-sensory cortex is one of the best understood cortical areas, it was chosen for this study. All following chapters refer to this cortical area.

1.1.2 Concepts of neuronal signaling

Basics of signal generation in the single neuron

Neurons generate an electric potential across their outer cell membrane by maintaining concentration gradients of several ion species like Na^+ , K^+ , Ca^{2+} and Cl^- (see chapter 1.3.2). The resting membrane potential V_{rest} (intracellular potential versus grounded extracellular space) is negative, usually around -60 to -90 mV. Hyperpolarization causes V_{rest} to shift to more negative values, while depolarization leads to an increase in V_{rest} .

The neuron's output signal is a strong depolarization called an action potential (AP, see also chapter 1.3.2), which has a stereotypical fast time-course. An AP is elicited near the soma in the axon only if the membrane potential V_m crosses a depolarized threshold voltage V_{thresh} , usually in the range of -40 mV. The AP wave-form comprises three phases: (1) a very fast rising phase with a slope of several hundred mV/ms, which elevates V_m to a positive value of around +30 mV; (2) a fast decay phase repolarizing the cell to V_{thresh} ; and (3) an after-hyperpolarization (AHP) phase during which V_m is kept hyperpolarized relative to V_{thresh} and the neuron is prevented from eliciting another AP.

The AP then travels away from the soma along the axon, where it is transmitted via contacts called synapses to the following neurons. The cell in which the AP is elicited is called the pre-synaptic cell, the cell receiving the synaptic signal is called post-synaptic. In addition, APs also actively travel back into the dendrite (back-propagating action potential, BPAP), a mechanism thought to mediate a "hand-shake" for output-dependent synaptic plasticity (Debanne et al., 1998; Bi & Poo, 1998).

Synaptic transmission

All chemical synapses (we neglect here electric synapses or gap-junctions) work following similar principles: Upon arrival of a presynaptic AP, the intracellular free Ca^{2+} concentration in the presynaptic terminal is increased. Calcium sensors then initiate a signal cascade which ultimately leads to release of a chemical compound called neurotransmitter into the extracellular space between pre- and postsynaptic membrane (synaptic cleft). Once the neurotransmitter reaches the postsynaptic membrane, it binds to membrane-bound neurotransmitter receptor proteins, which in turn either (1) change their electric conductance and therefore can be understood as a conductance in parallel to a battery mediating the electric driving force E_{rev} (ionotropic receptors); or (2) initiate an postsynaptic

signal cascade which leads to conductance change or alteration of postsynaptic properties (metabotropic receptors).

For ionotropic receptors, the postsynaptic cell experiences a local change in membrane potential upon activation of a synapse. Excitatory synapses mediate a depolarization (excitatory post-synaptic potential, EPSP), thereby shifting the membrane potential towards V_{thresh} , while inhibitory synapses either hyperpolarize the cell (inhibitory post-synaptic potential, IPSP) or, if E_{rev} is close to V_{rest} , effectively shunt the cell's membrane without eliciting a post-synaptic potential PSP (so-called shunting inhibition).

Dendritic integration

PSPs at the synaptic sites are not simply summed at the soma, as synapses are located all over the dendritic tree and thus PSPs experience changes in shape and amplitude due to global and local dendritic properties. Waveform and amplitude of single PSPs are changed primarily by the dendrite working as a low-pass filter, a result from linear cable theory (see chapter 1.3.1), broadening PSPs and reducing their amplitude the further away from the soma the synapse is located (for a review, see Koch, 1999). Additionally, non-linear properties of dendrites influence integration of PSPs to a yet unknown extent:

- AP back-propagation: In cortical pyramidal neurons as well as in other cells of the CNS, APs elicited in the axon initial segment not only travel down the axon but also the dendrite in an active manner. This implies that voltage-dependent ion channels are also present in dendritic structures, which also has been shown experimentally (Stuart & Sakmann, 1994; Häusser et al., 1995; Stuart et al., 1997). Additionally, AP waveform introduces a refractory period to the dendrite, thereby inhibiting further synaptic excitation.
- A couple of voltage-gated ion channels mediate local integration in dendrites. Threshold events similar to axonal APs have been observed experimentally in dendrites (Ca^{2+} - or NMDA-spikes; Schiller et al., 1997; Schiller & Schiller, 2001), which are elicited upon concomitant activation of clusters of synapses. These effects amplify distal input otherwise invisible at the soma. In cortical pyramidal cells, the primary bifurcation of the apical dendrite often works as a kind of integration node. Interaction of axonal APs and Ca^{2+} -spikes initiated in this node has been shown to lead to altered AP-firing behavior (BAC-firing; Larkum et al., 2001).

- The hyperpolarization-activated current I_h has been shown experimentally to have a high impact on dendritic integration. Especially in cortical L5 pyramidal cells, in which the channel density is high, I_h has been shown to govern voltage attenuation along the dendrite (Stuart & Spruston, 1998; Berger et al., 2001) uncouple dendritic and somatic compartments efficiently (Berger et al., 2003). Complementary experiments in pyramidal cells in the CA1 region of the hippocampus showed a high impact of I_h current on dendritic integration (Maccaferri et al., 1993; Magee, 1998).

All the above-mentioned features of dendritic signal integration critically depend on the cell's membrane properties like distribution and voltage-dependence of ion channels. Yet, in most cell types these properties still remain to be elucidated.

1.1.3 Neurons under *in vivo* conditions

According to the “neuron doctrine”, neurons are morphologically independent cellular units. These units are heavily interconnected via synapses forming complex biological neuronal networks. Consequently, activity in one neuron will have an effect on large parts of the surrounding network, leading to complex population activity patterns when actual computations take place. In order to understand this complex network activity we not only need to know the electrical and biochemical properties of the individual cell types, but also according to which rules and how these excitable circuits are activated under natural conditions in the intact brain (*in vivo*).

UP- and DOWN states

In vivo measurements of cortical cells reveal slow oscillations of membrane potential with frequencies <1 Hz (Steriade et al., 1993; Cowan & Wilson, 1994). During anesthesia and quiet wakefulness, this spontaneous activity takes the form of so-called UP- and DOWN-states. While during the DOWN-state V_m stays close to V_{rest} , during UP-states the cell is depolarized by around 15 mV (Stern et al., 1997; Lampl et al., 1999; Steriade, 2001; Petersen et al., 2003b).

Many studies have been performed on UP/DOWN-states, most of them assuming high activation frequencies of synapses of >1 Hz during UP-states (Pare et al., 1998; Destexhe et al., 2001; Destexhe, 2003). This concept has

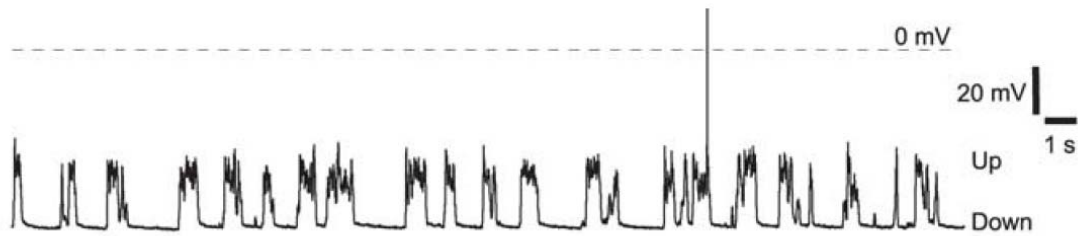


Fig. 1.3 UP- and DOWN-states recorded in vivo in somato-sensory cortex of an anesthetized rat. (Figure taken from Waters & Helmchen, 2006).

been pursued in several experimental as well as modeling studies, having lead to the conclusion that, during UP-states, the neuron's input resistance is significantly reduced compared to DOWN-states due to an increase in synaptic conductance all over the dendritic tree (for a theoretical derivation see Koch, 1999; Barrett, 1975; Rudolph & Destexhe, 2003).

However, in a recent study (Waters & Helmchen, 2006) it was shown that in cortical L2/3 pyramidal neurons, R_{in} was increased by around 20% during UP-states, with an equivalent increase in the cell's time-constant (see chapter 1.3.1). Furthermore, they could show that the L2/3 pyramidal neurons' voltage response upon current injection (either synaptic or through an electrode during electrophysiological measurement) is supra-linear and can be well described by a second-order polynomial (see chapter 2.2.2). This effect of supralinearity is known as anomalous rectification (AR) and has been described previously (Katz, 1949; Wilson, 1992; Johnston & Wu, 1999; see chapter 1.3.2). In respect to UP/DOWN-states, Waters & Helmchen (2006) showed that due to AR the numbers of active synapses needed to generate UP-states in L2/3 pyramidal neurons is much smaller (around 5 active synapses per ms) than assumed in previous studies, a finding which very well fits into the emerging picture of sparse activity in neocortex (Kerr et al., 2005; Lee et al., 2006). This strongly supports the notion that intrinsic neuronal properties have a strong impact on how the cell responds to the *in vivo* situation.

1.1.4 Development

At birth, the brain is not fully matured, but in a state where it first has to learn to make sense out of sensory input and how to react in an appropriate manner.

Most of the “wiring” of neuronal networks occurs while the animal starts exploring its surroundings, interacts with other animals, searches for food, etc. Additionally, not all sensory organs are fully available at birth: For example, rats are born blind, and their eyes open fully around 12 days after birth. As we have chosen the rat as model system for this study, the following paragraphs refer to developmental changes in these rodents.

Postnatal maturation of the neocortex

The cortex is assembled from neurons with an exceptionally long and complex life history (for a more thorough introduction see Squire et al., 2003; Tan et al., 2002). This includes migration over long distances from two separate germinal zones into specific layers. Here, superficial layers are assembled later than deep layers, meaning with respect to cortical pyramidal cells that L2/3 neurons only reach their layer after L5 and 6 have been established (Sidman & Rakic, 1973). During this migration process, cortical neurons exhibit strong interaction with glial cells, which work as migration guides (Rakic, 1971, 1972; Edmondson, 1987). In addition, axons and dendrites have to be guided such that cortical areas are established and innervated and projections from these areas reliably target deeper brain areas (Erzurumlu & Jhaveri, 1990; Cohen-Tannoudji et al., 1994). This requires continuous re-structuring by axon growth and –elimination (O’Leary, 1992; Katz & Crowley, 2002), as well as building and elimination of synapses (Wiesel, 1982; Mariani, 1983).

Not only is network connectivity incomplete at birth, but single neurons are immature themselves. During the first postnatal weeks cells not only change their morphology but undergo large changes in gene expression profile, which in the case of ion channels can lead to strong modifications of the intrinsic electrophysiological properties. These range from reversal of ionic gradients (Cherubini et al., 1991) to pronounced changes of channel kinetics and –densities (e.g. Fukuda & Prince, 1992; Kaplan et al., 2001).

Although these changes markedly slow down when the animal reaches adulthood, particularly following critical periods (see below), it is clear that the brain maintains a certain amount of plasticity, both regarding morphology and synaptic connectivity as well as homeostatic changes in the gene expression patterns.

The critical period

During postnatal development, the animal undergoes sensitive periods during which its brain is particularly sensitive to modifications due to experience. Some periods are crucial for the proper development of neuronal circuits and are thus termed critical periods.

The critical period in respect to sensory neuronal networks has been shown in the calibration for sound localization in barn owls (Knudsen et al., 1945), in birdsong learning in the zebra finch (Konishi, 1985; Doupe & Kuhl, 1999), in binocular vision in cats (Wiesel & Hubel, 1963; Hubel & Wiesel, 1970) and in rats (Toldi et al., 1996), and in filial imprinting leading to recognizing own parents in human babies (Hess, 1973).

In rats, the critical period with respect to the somato-sensory cortex takes place during the second postnatal week. During this time, L2/3 dendritic arbors elaborate (Maravall et al., 2004), as do the projections from L4 to L2/3 (Bender et al., 2003). Simultaneously, the density of cortical synapses (Micheva & Beaulieu, 1996) and the amplitude of stimulus-evoked postsynaptic potentials measured in L2/3 neurons *in vivo* increase several-fold (Stern et al., 2001). With the end of postnatal week 2, these developmental changes are mostly complete.

1.2 The L2/3 pyramidal neuron

The object of this study is the principal neuron located in cortical L2/3, the L2/3 pyramidal cell. In the following sections, the properties of these cells will be described, starting with their morphological particularities.

1.2.1 Morphology

L2/3 pyramidal cells are the most superficial excitatory neurons in the neocortex. In rat somatosensory cortex, L2/3 is the layer comprising the largest number of neurons per column (De Kock et al., 2007; Beaulieu, 1993). Their sheer number (40000-60000 mm⁻³) suggests that L2/3 provides a huge amount of computational power within the brain.

As all pyramidal cells, L2/3 pyramids possess an elongated soma, from the pia-oriented tip of which the apical dendrite originates. The basal dendrites grow from the “base” of the pyramid, whereby the oval soma shape is distorted into a pyramid-like shape. Size of L2/3 pyramidal somata in adult rats is around 20 µm in

height and 16 μm in diameter, with a mean aspect ratio (height/width) of around 1.2 and surface area of 270 μm^2 (Schroder & Luhmann, 1997).

Morphological parameters concerning dendrites have to be considered with care, since most of the data have been obtained from *in vitro* slice experiments, where it is likely that basal dendrites and part of the apical tuft and obliques are cut off during slicing. The apical dendrite of L2/3 pyramidal cells invariably extends to the pial surface. The main trunk becomes thinner as distance to soma increases. Close to L1, the apical dendrite bifurcates into the apical tuft, with a projected receptive area of around $26 \cdot 10^{-3} \text{ mm}^2$, while the remaining apical dendrite (trunk and obliques) covers approximately $40 \cdot 10^{-3} \text{ mm}^2$. On average, 5 basal dendrites originate at the soma, and cover an area of around $60 \cdot 10^{-3} \text{ mm}^2$ (Schroder & Luhmann, 1997). Complexity of basal dendrites seems to be larger than of the apical, as judged by the number of branch points. Morphological variability is very high for this cell type (Larkman, 1991a; Larkman & Mason, 1990).

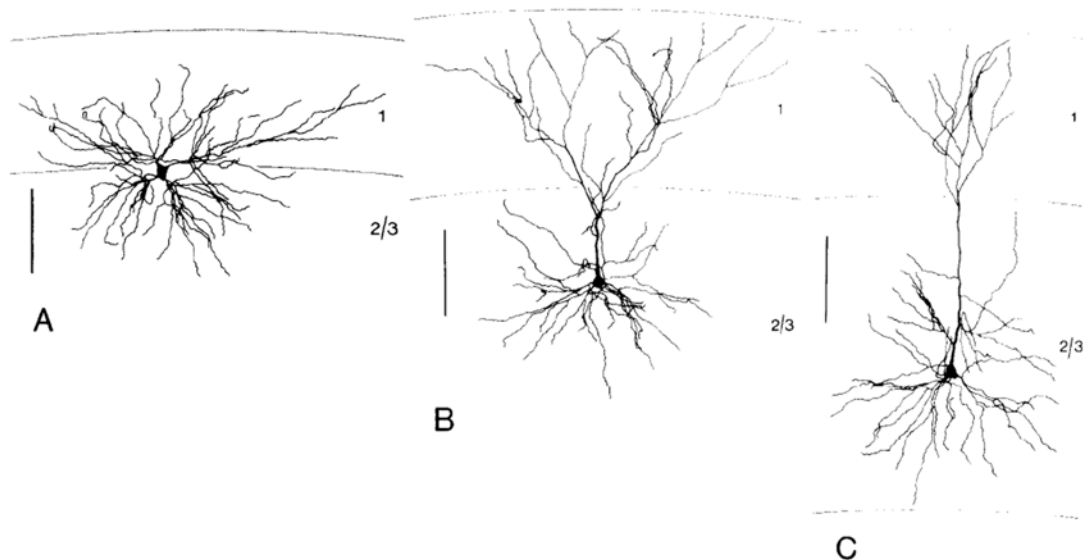


Figure 1.4 Example morphologies of L2/3 pyramidal neurons. A-C, cells with increasing depth of soma relative to pial surface. Layers 1 and 2/3 are indicated. Taken from Larkman & Mason, 1990.

Differences between L2 and L3 pyramidal cells arise when the shape of the apical dendrite is related to soma position within L2/3 (Feldmeyer et al., 2006; Larkman & Mason, 1990). It was shown that pyramidal cells from L3 have a long apical dendrite which bifurcates close to L1 and forms a structurally simple (i. e.

few branch points) apical tuft. The apical dendrite of cells from L2, in contrast, bifurcates close to the soma and shows a much more complex tuft in respect to dendritic length and number of branch points. Also, in L2 cells, the apical tuft extends further laterally than the basal dendrites, with the other way round in L3 pyramids (Dirk Feldmeyer, personal communication).

Distribution of spines

Larkman (1991c) counted spine distributions on dendrites of L2/3 cells in dependence of dendritic path length from the soma. He assessed a total number of around 8000 spines per cell, leading to a total of 9400 excitatory synapses. Here, the assumption was used that 85% of all excitatory synapses are located on spines, while the rest sits directly on dendritic segments (Peters, 1987). The mean spine density was 1.4 per μm dendritic length for basal dendrites, $2.5 \mu\text{m}^{-1}$ on the apical trunk, $1.3 \mu\text{m}^{-1}$ in obliques and $0.6 \mu\text{m}^{-1}$ in the apical tuft segments.

In addition, the number of inhibitory synapses was estimated to be 13% of all synapses (Peters, 1987), leading to a total number of between 1400 (Larkman, 1991c) and 2000 (DeFelipe & Farinas, 1992) per L2/3 neuron. The distribution of these synapses is not that easily measurable, as only few are located on spines. Most inhibitory synapses directly target dendritic shafts of the soma, where IPSPs show a higher impact on dendritic integration (see chapter 1.3.3).

1.2.2 Electrophysiological properties

L2/3 pyramidal cells are not as easily accessible with electrophysiological methods as the much larger L5 or L6 pyramids. This has led to the situation that L2/3 pyramids, although very numerous within the neocortex, have been characterized systematically in terms of their electrophysiological properties only very recently. Most of these data were obtained from adult animals and experimental studies addressing the development of L2/3 neurons are scarce.

Sub-threshold properties

Several studies exist, in which the basic sub-threshold properties, namely input resistance R_{in} and resting membrane potential V_{rest} , of L2/3 pyramids have been examined: Values found *in vitro* range from $R_{\text{in}} = 26\text{-}30 \text{ M}\Omega$ (Hwa & Avoli, 1991;

Larkum et al., 2007) to around $R_{in} = 45 \text{ M}\Omega$ (Traub et al., 2003; Waters et al., 2003), while resting potential was found to lie between -80 mV (Schroder & Luhmann, 1997) and -68 mV (Traub et al., 2003). Values from *in vivo* experiments obtained during DOWN-states lie in the same range (Waters et al., 2003; Waters & Helmchen, 2004; Waters & Helmchen, 2006)

One of the basic findings in the study of Waters & Helmchen (2006) was that L2/3 pyramidal neurons show pronounced anomalous rectification under *in vivo* conditions, an effect, which had been described for cortical pyramidal neurons in several previous *in vitro* studies (Connors et al., 1982; Stafstrom et al., 1982; Sutor & Zieglgänsberger, 1987; Hwa & Avoli, 1991; Cowan & Wilson, 1994). Hwa & Avoli (1991) reported that high concentrations of 3 mM Ba^{2+} and the intracellular blocker QX 314 abolished AR, leading to the conclusion that in L2/3 pyramids it is not Ih which is responsible for AR, but an unknown voltage-dependent K^+ conductance. In particular, these findings also show one of the main differences between L2/3 and L5 pyramidal neurons: In L5 pyramids, sag is very prominent (30-40%; Zhu, 2000), indicating higher densities of HCN channels (Kole et al., 2006), while in L2/3 pyramids, little sag has been observed (Larkman, 1991b; Larkum et al., 2007). The effect of nonlinear I-V relationships and their effect on firing behavior also has been attributed to persistent Na^+ currents (Traub et al., 2003), but with sparse experimental evidence. Hence, a detailed knowledge of the ionic currents shaping sub-threshold membrane potential changes is still lacking.

Supra-threshold properties

L2/3 pyramidal neurons were found to be regularly spiking, i.e., upon constant depolarizing current injection of arbitrarily long duration, the spike frequency stays constant. This is in contrast to L5 pyramids, among which around 15% are able to generate intrinsic bursts (Connors et al., 1982). Nevertheless, also in L2/3 pyramids doublets of APs can be elicited by stimulus onset (Schroder & Luhmann, 1997; Larkum et al., 2007).

AP waveform is similar to that found in L5 pyramids, with an amplitude of around 120 mV relative to V_{rest} *in vitro* and *in vivo* (Waters et al., 2003) and a rising flank 2.5 times faster than the falling (Schroder & Luhmann, 1997). APs propagate actively into the dendrites, as was shown by calcium imaging and dual somatic and dendritic recordings (Waters et al., 2003; Waters & Helmchen 2004; Larkum et al., 2007). Voltage attenuation is comparably weak, such that the AP

might be sensed by the whole dendritic tree, despite a distortion of the waveform as the AP propagates along the dendrite.

In a very recent study (Larkum et al., 2007), dendritic properties of L2/3 pyramidal neurons were examined. Although properties were found, which were qualitatively similar to those found in L5 pyramidal neurons (e.g. the ability of the apical dendrite to generate regenerative potentials), these properties also clearly differed quantitatively from L5 neurons. While in L5 neurons interaction of somatically generated APs and long-lasting dendritic calcium spikes leads to firing of several additional APs at the soma (Larkum et al., 1999), dendritic spikes in L2/3 pyramids were shorter and typically caused only one additional AP when paired with somatic spikes (Larkum et al., 2007).

1.2.3 Input and output

The following considerations of synaptic input and output of L2/3 pyramidal neurons are mainly based on data from rat barrel cortex. As input from different layers or brain areas arrive at different locations of the dendritic tree, integration of these inputs will strongly depend on the local morphological and electrophysiological properties of these dendritic compartments.

Main translaminal input into L2/3 arrives from spiny stellate cells and star pyramids in L4. The synapses from L4 onto L2/3 pyramidal cells are invariably located on the basal dendrites (85%) and proximal apical obliques (15%) (Feldmeyer et al., 2002). In somatosensory cortex, these projections are restricted to single columns (Petersen et al., 2003; Lubke et al., 2003). L4 to L2/3 connections are unidirectional with close to no activity arriving in L4 from L2/3 (Feldmeyer et al., 2002). Additionally, several L4 cells project onto one given L2/3 pyramidal cell. This leads to a broader receptive field (the region of space in which the presence of a stimulus will alter the neuron's AP output) in L2/3 pyramidal cells in comparison to L4 neurons (Brecht et al., 2003). Synaptic strength depends on distance of the L2/3 target cell from L4, with a decrease in strength the further away the L2/3 pyramidal cell (Feldmeyer et al., 2002).

Connections from L2/3 onto L2/3 cells were examined within single cortical columns of rat barrel cortex (Feldmeyer et al., 2006). Here, comparable convergence and divergence was found, suggesting that in L2/3 signals are amplified before being distributed to neighboring columns. Again, practically all

synapses are located on the basal dendrites, with the innervation domain being almost identical to that of L4 to L2/3 connections.

Additional input arrives at the apical tuft from thalamus and higher order sensory areas. It seems that, together with L5 pyramidal neurons, L2/3 pyramids are through their apical tree the only cortical cells receptive to these inputs (Cauller & Kulics, 1991). Taken together with a second integrative centre near the apical tuft (Ca^{2+} spike initiation zone) these inputs might strongly shape the neuron's response *in vivo*.

Output from L2/3 pyramidal neurons

L2/3 pyramidal cells receive input from many different areas and other cortical layers. These inputs are integrated in a complicated, non-linear manner, since it was shown that the dendrites of these cells host a variety of voltage dependent channels. However, most of the mechanisms involved have not been completely understood, requiring a lot more experimental effort to decipher the cells' behavior. In addition, many questions have not been addressed at all, like how these cells mature during postnatal development.

A complimentary tool for understanding experimental results and guiding further experiments are numerical computer simulations of neurons, the conceptual basis of which will be described in the remaining paragraphs of this introductory section.

1.3 Biophysics of neuronal computation

In the following section a short introduction to basic concepts of a more physical view on single cells will be given. These concepts will be presented in a general way applicable to practically all cell types, while the particular methods utilized in this study will be described in detail in the modeling methods section (chapter 3.1).

1.3.1 The passive cable equation

Dendrites and axons of neurons can be considered as electrical cables with a conductive core represented by an axial resistance R_{ax} and an outer membrane represented by a parallel circuit consisting of a membrane resistance R_m and a

capacitance C_m (Jack et al., 1983). The core conductor – the intracellular medium of the cell – is an electrolytic solution, the electrical conductivity of which is determined by the concentration of mobile intracellular ions such as potassium and chloride and by the excluded volume taken up by intracellular organelles such as mitochondria. Typical values for the specific resistivity of the intracellular medium R_{ax} in neurons of the mammalian central nervous system range from 70 to 150 $\Omega\cdot\text{cm}$ (Roth & Häusser, 2001). The capacitance of the membrane is determined by the effective thickness and the effective dielectric constant of the lipid bilayer. Both are not exactly known because of proteins embedded into the cell membrane at unknown density. Following voltage changes these proteins experience partial charge movements and thus add to unknown extent to the membrane capacitance. Direct measurements of C_m yield values of 1 $\mu\text{F}/\text{cm}^2$ for various cell types (Gentet et al., 2000). Membrane resistance is mainly mediated by ion-conducting channel proteins. One can divide R_m into an “active” part for voltage-dependent ion channels and a “passive” part for voltage-independent leak conductances. The latter usually lead to a specific passive membrane resistance of 10 to 100 $\text{k}\Omega\cdot\text{cm}^2$ (Koch, 1999).

Locally, between branch points, the geometry of the dendrite or axon can be approximated by a cylinder. This cylinder is sufficiently long and thin, and the membrane resistance is large compared to the intracellular resistivity such that most of the electric current inside the structure flows parallel to its longitudinal axis. This allows the reduction of the problem from three dimensions to one: One does not need to consider the radial flow of currents inside the cylinder but only the component along one spatial dimension x along the longitudinal axis. Furthermore, capacitive effects inside the intracellular medium can be neglected on a millisecond timescale, as well as inductive effects (Jack et al., 1983). Finally, for considering single cells, one may assume the extracellular medium as having negligible resistivity and being virtually isopotential (which might not hold anymore when considering cells in intact tissue *in vivo*).

These simplifications allow the application of the linear cable equation, which was first formulated by William Thomson, later Lord Kelvin, in 1854 with respect to transatlantic telegraph cables. This equation governs the development of voltage in space and time along a one-dimensional cable of diameter d :

$$\lambda^2 \frac{\partial^2 V(x,t)}{\partial x^2} = V(x,t) - V_{rest} + \tau_m \frac{\partial V(x,t)}{\partial t} - R_m I_{ext}(x,t) \quad (1.1)$$

Here, injection of external currents I_{ext} has been added. The electrotonic length constant λ is given by

$$\lambda = \sqrt{\frac{d R_m}{4 R_{ax}}} \quad (1.2)$$

and the time constant τ by

$$\tau = R_m C_m \quad (1.3)$$

The linear cable equation is a partial differential equation of the parabolic type similar to the diffusion equation. Buffered diffusion of calcium ions, an important intracellular messenger, indeed follows a similar mathematical equation.

For analysis of a passive dendritic tree, Wilfried Rall developed a method of collapsing dendrites into a single equivalence cylinder of varying diameter (Rall, 1962; Rall, 1964). That way, the calculation of voltages at branching points can be circumvented. Of course, for calculating synaptic signaling in branched dendritic trees with synapses distributed over the whole structure, this method is unfeasible, and numerical simulation of the tree have to be performed. To this end, the branched dendritic tree is discretized into compartments such that in equation 1.1 the differentials become differences, which allows numerical approaches (see chapter 3.1.2).

1.3.2 Voltage dependent ion channels

If the cell membranes of neurons where passive only, one crucial feature for performing computations would be missing: nonlinearities. Fortunately, nature came up with the means to make life more interesting, namely voltage-dependent ion channels, which allow a current of one or several ion species to pass through the membrane in a voltage dependent manner. These mechanisms mediate most of the neuron's nonlinearities, the most prominent of which is the action potential.

Ion species and reversal potentials

For each ion species X , the reversal potential E_{rev} can be defined as that voltage across the membrane, for which the net ion current vanishes, given the concentration gradient across the membrane. E_{rev} is determined by the Nernst-equation:

$$E_{rev,X} = \frac{zF}{RT} \ln\left(\frac{[X]_o}{[X]_i}\right) \quad (1.4)$$

Here, z denotes the valence of that ion species, $[X]_o$ and $[X]_i$ its outside and inside concentrations, respectively, F Faraday's constant, R the universal gas constant and T the absolute temperature. Equation 1.4 describes an electrochemical equilibrium, meaning that, given a certain concentration difference across an impermeable membrane a counter-balancing electric potential will build up; vice versa, a given potential difference across a permeable membrane will lead to an according concentration gradient. Only a small number of ion species govern the electric activity in cortical principal neurons. Each of these species is driven by their own reversal potential as calculated in equation 1.4. Estimate values for neurons are shown in Table 1.1.

Ion species	$[X]_i$ / mM	$[X]_o$ / mM	$E_{rev,X}$ / mV
Na^+	18	150	+56
K^+	135	3	-102
Cl^-	7	120	-76

Table 1.1 Concentrations and reversal potentials of the main ion species governing electrical behavior of neurons.

For several ion species and partially permeable membranes, the total equilibrium potential V_{rest} is described by the Goldman-Hodgkin-Katz (GHK) equation (Goldman, 1943; Hodgkin & Katz, 1949):

$$V_{rest} = \frac{RT}{F} \ln \frac{\sum P_{cat} [X_{cat}]_o + \sum P_{an} [X_{an}]_i}{\sum P_{cat} [X_{cat}]_i + \sum P_{an} [X_{an}]_o} \quad (1.6)$$

with a similar nomenclature as in equation 1.5. Here, $[X_{cat}]$ and $[X_{an}]$ denote concentrations of cations and anions, respectively. Sums run over all ion species present. The coefficients P_{cat} and P_{an} are the respective permeabilities.

Rectification

The term rectification denotes a non-ohmic, i.e. non-linear, behavior of the cell's I-V relationship. In analogy to equation 1.6, the current through the membrane of a given ion species is given by the GHK current equation:

$$I = P \frac{z^2 F^2}{RT} V \frac{[X]_i - [X]_o e^{\frac{zFV}{RT}}}{1 - e^{\frac{zFV}{RT}}} \quad (1.7)$$

Nomenclature is as in equation 1.5. This model is derived with the Nernst-Planck equation for electrodiffusion under the assumption of a constant electric field across the membrane and independent movement of ions. Even without voltage-dependent permeability, equation 1.7 predicts non-linear voltage-dependent currents if $[X]_i$ and $[X]_o$ are different (Fig. 1.5). For cations, currents inwardly rectify for $[X]_o/[X]_i > 1$ and outwardly rectify for $[X]_o/[X]_i < 1$.

Since the conductance through passive membranes is mainly mediated by voltage-independent K^+ -channels, following equation 1.7 an outward rectifying I-V-relationship would be expected. Any deviation from this behavior implies the presence of other, presumably voltage-dependent channels, the theory of which will be covered in the following paragraph.

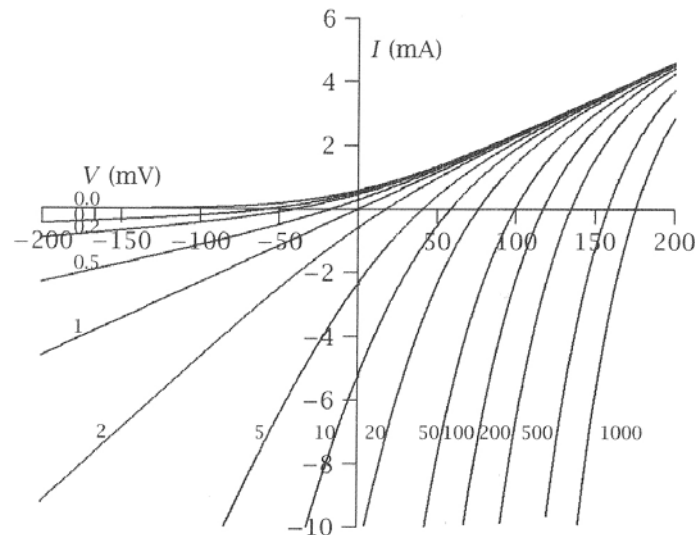


Fig. 1.5 Cationic currents in dependence of membrane potential for various values of $[X_{cat}]_o/[X_{cat}]_i$ (given in numbers at respective curve). Figure taken from Johnston & Wu, 1997.

The Hodgkin-Huxley (HH) model

The most common description of channel gating is the formalism proposed by Hodgkin & Huxley (1952 a-d). They assume that for a channel to conduct an

electric current a series of independent, voltage-dependent gating particles have to be opened. The state dynamics of each particle x is described by first order kinetics:



The forward and backward rates, $\alpha(V)$ and $\beta(V)$, respectively, introduce the voltage dependency of the gating.

Taking x as the probability of the particle being open, one obtains the associated differential equation:

$$\begin{aligned} \frac{dx}{dt} &= \alpha(V)(1-x) - \beta(V)x \\ &= \frac{x_{\infty}(V) - x}{\tau_x(V)} \end{aligned} \quad (1.9)$$

with the steady state value of x , $x_{\infty}(V)$, and the time constant, $\tau_x(V)$, given by $\alpha(V)$ and $\beta(V)$ as:

$$\begin{aligned} x_{\infty} &= \frac{\alpha(V)}{\alpha(V) + \beta(V)} \\ \tau_x &= \frac{1}{\alpha(V) + \beta(V)} \end{aligned} \quad (1.10)$$

In addition to voltage dependence the rate constants can also depend on other signals, like e. g. the intracellular concentration of free calcium, $[Ca^{2+}]_i$.

The probability p of the channel being open is the product of the open probabilities of the channel's gating particles:

$$p(V, t, \dots) = \prod_i x_i^{n_i}(V, t, \dots) \quad (1.11)$$

Here, the x_i denote the different types of gating particles (e. g. one activation and one inactivation particle) and n_i is the number of a certain particle associated with the channel. The current I_X through a given channel then is:

$$I_X = \bar{g}_X (V - E_X) \prod_i x_i^{n_i} \quad (1.12)$$

For example, in the original HH model, the fast sodium channel responsible for the fast rising phase of the action potential was modeled as having three activation particles, n , and one inactivation particle, h (Fig. 1.6):

$$p(V,t) = n(V,t)^3 h(V,t) \quad (1.13)$$

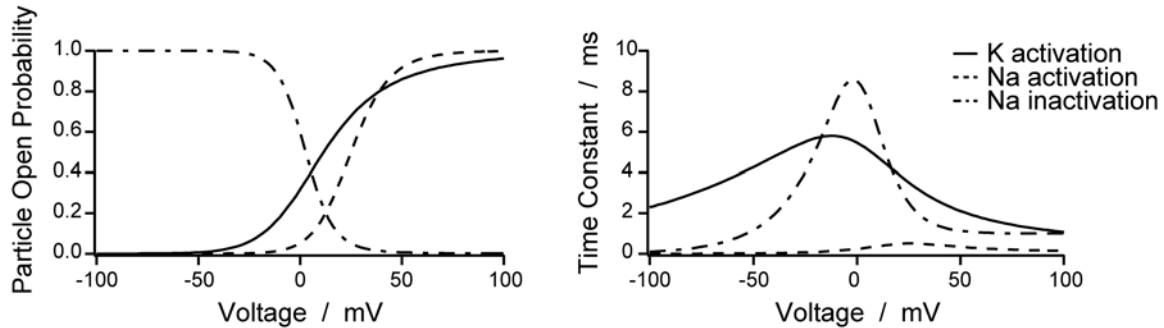


Fig. 1.6 Kinetics of the original Hodgkin-Huxley model of membrane excitability of the squid giant axon (Hodgkin & Huxley, 1952d). Left panel: Voltage-dependent steady state open probability $x_o(V)$ of activation and inactivation particles. Right panel: Time constants τ_x for reaching steady state.

Incorporating currents through voltage-gated ion channels into the cable equation 1.1 is done simply by adding the currents to the right-hand side to I_{ext} . Nevertheless, as channel activation and inactivation is governed by $V(x,t)$, a system of coupled differential equations has to be solved in order to calculate the development of $V(x,t)$ in time and space. Usually, this is done numerically (see chapter 3.1.2)

The n_i in equation 1.11 (the number present of a given gating particle) can be considered as another free parameter of the channel kinetics. It accounts for the observation that some channels show sigmoidal activation behavior under voltage clamp conditions arising from the time course $(1 - \exp(-t))^n$ for $n > 1$. This introduces a delay to the closed-to-open transition, which is important for e. g. again the fast sodium channel.

One has to be cautious, though, when one compares the predictions and structure of the HH-model with actual channel proteins. Although these macromolecules do possess voltage sensors and selectivity filters for certain ion species, structures representing the predicted number of gating particles have not been found. Thus, the HH-model has to be viewed as a purely mathematical tool for a phenomenological description of ion channel behavior. Nevertheless, a more physically relevant description based on the HH-model and concepts of enzyme kinetics will be introduced in chapter 3.1.1.

Types of ion channels

Based on equation 1.9, two principal types of voltage-dependent ion channels can be identified: channels with no inactivation particle mediating persistent currents, and inactivating channels mediating transient currents. A good overview of most known channel types can be found in Hille (2001).

The transient class comprises the fast Na⁺-channel responsible for the fast rising phase of the AP in the squid giant axon (Hodgkin & Huxley, 1952 a-d), which is sensitive to tetrodotoxin (TTX; Catterall, 1992); the A-type K⁺-channel shaping the delay of AP initiation after stimulus onset and AP waveform (Hagiwara et al., 1961; Connor & Stevens, 1971); and the T-type Ca²⁺-channel (Nilius et al., 1985).

Persistent channels are the delayed rectifier K⁺-channel responsible for repolarization from AP (Hodgkin & Huxley, 1952 a-d); the M-type K⁺-channel responsible for firing frequency adaptation (Brown, 1988; Wang et al., 1998; Jentsch, 2000); the persistent Na⁺-channel (Chandler & Meves, 1970; Llinas, 1988; Goldin, 2001); the L-type Ca²⁺-channel (Nilius et al., 1985); and the HCN-channel mediating the hyperpolarization activated or “queer” current I_h (Yanagihara & Irisawa, 1980; DiFrancesco, 1981; McCormick & Pape, 1990; Lüthi & McCormick, 1998).

Additionally, a couple of K⁺-channels are not only voltage-dependent, but gating also depends on $[Ca^{2+}]_i$. This class comprises the SK and BK channels, responsible for AP after-hyperpolarization (AHP) on different timescales and AP frequency adaptation upon Ca²⁺-accumulation (Meech, 1974; Blatz & Magleby, 1987; Garcia et al., 1997; reviewed in Sah, 1996).

1.4 Specific goals of this study

In this study, the integrative and sub-threshold properties of L2/3 pyramidal neurons will be investigated by combined experimental and computer modeling approaches. The main questions are:

- (1) How do the biophysical properties like input resistance, anomalous rectification and action potential properties of L2/3 pyramidal cells change during postnatal development?
- (2) How can the effect of anomalous rectification be explained in terms of molecular mechanisms (ionic conductances)?

(3) Can these properties be incorporated into a consistent model for the aged-dependence of L2/3 pyramidal neurons?

(4) What is the cells' response to modeled *in vivo*-like activity at different ages?

To address these questions, *in vitro* electrophysiological experiments applying the whole-cell patch-clamp technique in acute brain slices of rat neocortex were performed. During these experiments, several channel-blocking drugs were applied in order to elucidate the mechanisms underlying anomalous rectification in L2/3 pyramidal cells. Biocytin-labeling during patch-clamp experiments allowed retrieval of cell morphologies.

Using the obtained experimental data, age dependent computer models of varying complexity were build, starting with single compartment cells up to full-morphology neurons with non-homogenous channel distributions. In order to find near-optimal parameter sets to reproduce experimental data, an automated parameter search algorithm was written and employed. This permitted not only to build a high number of single cell models with objective constraints, but also to give an estimate of the variability of parameters in these cells. These age dependent models were then exposed to stochastic synaptic input as it is presumably found during UP-states *in vivo*, such that the effect of non-linear synaptic integration due to anomalous rectification could be assessed.

2 Experiments

2.1 Experimental methods

Whole cell patch-clamp recordings were obtained from L2/3 pyramidal neurons in acute brain slices prepared from animals of different ages. Cell morphologies were histologically reconstructed and sub- and suprathreshold electrical properties were characterized. The currents underlying anomalous rectification (AR) were dissected pharmacologically. In the following paragraphs we describe the experimental setup and procedures as well as the data analysis procedures in detail.

2.1.1 Electrophysiology

Brain slice preparation

Parasagittal slices of the rat cortex were prepared from 8 to 45 days old (p8-p45) Wistar rats according to standard procedures (Edwards et al., 1989; Blanton et al., 1989). All procedures were in accordance with the German animal protection law. Rats were anesthetized with Isoflurane and decapitated. The two hemispheres of the brain were quickly removed and transferred to ice cold slice solution. One hemisphere was glued with its cut surface onto a block of stainless steel in a slice chamber and quickly covered with ice cold slice solution. The top 2.5 to 3.5 mm of tissue (depending on age) were removed. Then 300 μm thick slices were cut using a custom-built vibratome (Max-Planck-Institute for Medical Research, Heidelberg) equipped with a standard razor blade. Brain slices were immediately removed from the slice chamber and transferred onto a gaze net in a beaker containing slice solution at room temperature (about 20°C). Slices could be stored between 4 and 8 hours (longer for younger animals) with most of the cells still intact. For experiments brain slices were chosen in which the apical dendrites of pyramidal neurons were parallel to the slice surface or running into the slice at a small angle in order to ensure that the apical tuft was intact.

The patch-clamp technique

The patch-clamp technique, originally developed by Neher and Sakmann (Neher & Sakmann, 1976; Hamill et al., 1981; Sakmann & Neher, 1984) for measuring electric currents through single ion channels, can be adopted for measuring the

electric activity of single neurons using the so-called “whole-cell” configuration. The basic principle is to establish a tight seal of a glass micropipette with a tip diameter of around 1 μm with the outer membrane of the cell forming an electric resistance of above 1 $\text{G}\Omega$ between pipette interior and extracellular space (thus the term “gigaseal”), while the intracellular space is connected to the pipette interior via a relatively low access resistance R_{acc} of a few $\text{M}\Omega$. In current clamp (CC) mode, the current through the cell membrane is kept close to a preset command current by adjusting voltage by a feedback circuit. With no external command current, the measured voltage is the resting membrane potential. All data presented in this thesis were measured using the CC mode. In voltage clamp (VC) mode, the voltage is kept to command level by injecting appropriate currents through the micropipette.

Patch-clamp setup

All experiments were performed using an AxoClamp-2 B amplifier (Axon Instruments, Molecular Devices, CA, USA) operated in CC mode. In addition, voltage signals were monitored on an oscilloscope screen (5113, Tektronix, TX, USA). Analogue input signals were digitized and analogue control signals generated with a PCI-MIO-16E-1 AD/DA-converter board (National Instruments, TX, USA). The preamplifier headstage (HS-2A, Axon Instruments, CA, USA) holding the patch pipette was mounted on a motorized 3-axis micromanipulator (Luigs&Neumann, Ratingen, Germany) allowing positioning of the pipette tip with sub-micron precision and good stability (i. e., little drift during recordings). Continuous pressure (positive or negative) was applied to the pipette manually using a syringe. Brief suction pulses (-200 to -600 mbar, duration 200 ms) for breaking into the cells were generated with a Suction Pulser (Sigmann Elektronik, Hüffenhardt, Germany).

The patch-clamp setup was built around a fixed-stage Zeiss Axioscope 2 microscope equipped with a water immersion 40x objective (Achromplan, NA 0.75; Zeiss, Jena, Germany). Individual neurons were visualized using infrared (IR) differential interference contrast (DIC) microscopy (Stuart et al., 1993) using an IR sensitive camera (C2400, Hamamatsu, Japan). The brain slice chamber was mounted on a manual x-y microscope stage (independent of the fixed-stage microscope) to allow movement of the slice relative to the electrodes once these were in place. In order to avoid movement of the brain slice during recordings it was fixed with a grid made of a platinum frame and spanned with single nylon strings. In all experiments the chamber was perfused with extracellular solution

(see below), which was heated to 35°C by a flow heater (Sigmann Elektronik, Hüffenhardt, Germany). The bath was grounded with an Ag/AgCl electrode (World Precision Instruments, Florida, USA), which in turn was connected to the reference input of the preamplifier. Intracellular solution (see below) in the pipette was connected electrically to the preamplifier via a chlorided silver wire. Patch pipettes with a tip diameter of about 1.2 µm (4-7 MΩ tip resistance) were pulled from borosilicate glass tubes with a horizontal multistep puller (Sutter Instruments, CA, USA).

Solutions

All solutions were filtered to not contain particles bigger than 0.2 µm. The extracellular solution for preparing brain slices contained (in mM) 125 NaCl, 25 NaHCO₃, 2.5 KCl, 1.25 NaH₂PO₄, 3 myo-Inositol, 2 Na-pyruvat, 0.4 Vitamine C, 1 CaCl₂, 5 MgCl, 25 glucose. Solution was bubbled to pH 7.2 with a mixture of 95% O₂ and 5% CO₂ (“carbogen”). The bath solution (Biometra, Göttingen, Germany) contained (in mM): 125 NaCl, 25 NaHCO₃, 2.5 KCl, 1.25 NaH₂PO₄, 1 MgCl, 2 CaCl₂ and 25 glucose. Solution was bubbled with carbogen to pH 7.2. The intracellular solution contained (in mM): 135 K-gluconate, 10 Hepes, 10 Phosphocreatin-Na, 4 KCl, 4 ATP-Mg, 0.3 GTP; pH was adjusted to 7.2 with KOH. 3 mg/ml biocytine (Sigma-Aldrich, Switzerland) were added in all experiments to allow histological reconstruction of cell morphologies. Normal rat Ringer solution (NRR) contained: 135 NaCl, 5.4 KCl, 1.8 CaCl₂, 1 MgCl₂ and was buffered to pH 7.2 with 5 Hepes. 0.1 M Phosphate buffer (PB) contained Na₂HPO₄ and NaH₂PO₄ in a ratio of 3:1 (pH 7.2).

Whole cell recordings from L2/3 pyramidal neurons

The standard “blow-and-seal”-technique (Blanton et al., 1989) was used to obtain whole-cell recordings from pyramidal neurons (Fig. 2.1). A small positive pressure (around 30 mbar) was applied to the patch pipette while approaching the target neuron identified with IR-DIC microscopy. This ensured that other cells and cell debris (which usually is generated during slicing) were blown out of the pipette’s way, preventing a clog of the pipette tip. This approach is crucial for a successful formation of a GΩ-seal. While approaching the cell the amplifier was set to CC mode (with $I_{inj} = 0$ nA) to adjust the voltage measured at the tip to 0 mV. Small current testpulses of about 20 ms length and 20 pA amplitude were applied to measure pipette resistance. Once the pipette tip touched the neuron’s surface, a small dimple appeared on the cell’s surface due to the positive

pressure. At this moment the pressure was reduced to 0 mbar and the amplifier switched to VC mode and set to a hyperpolarized voltage (around -80 mV). Often this procedure was sufficient to achieve a seal resistance of above 1 G Ω , while in cases where the gigaseal did not form immediately a small negative pressure was applied until the resistance reached a sufficiently high value. Following successful gigaseal formation small negative suction pulses were applied through the patch pipette in order to break through the cell's outer membrane without disrupting the gigaseal. Establishment of the whole cell configuration was evident on the oscilloscope when larger transients appeared due to the cell's input resistance and membrane capacity. The amplifier was then switched back to current clamp mode, and the cell was given at least 10 minutes time to equilibrate with the internal solution contained in the patch pipette.

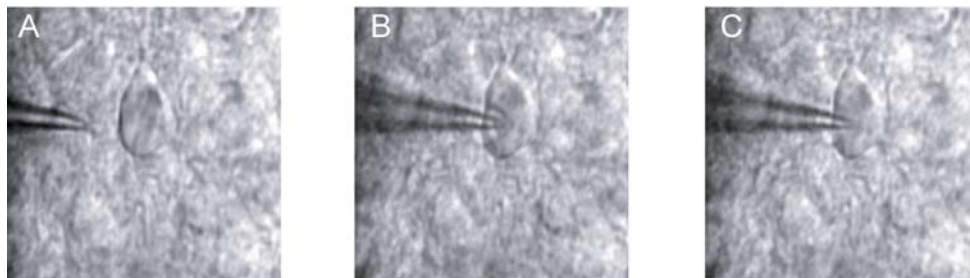


Fig. 2.1 Blow-and-seal technique. DIC images of the different steps described in the text. A, approaching the selected cell. B, the pipette touches the cell's surface. A small dimple is visible around the pipette's tip. C, sealing by removing the positive pressure from the pipette.

Before each measurement the access resistance (usually around 15-20 M Ω) was measured and counterbalanced using the bridge mode of the amplifier. With the command current set to 0 nA the measured voltage then corresponds to the resting membrane potential (see results section). Junction potential at the pipette tip was not taken into account in order to make results compatible with previous publications, but can be estimated to be around 10 mV based on the composition of intra- and extracellular solutions (Adam et al., 1995).

Voltage-current relationships were determined by injecting a series of 500 ms long current pulses preceded by 200 ms long baseline and followed by 500 ms for repolarization. The interpulse-interval was 5 s. Injected currents ranged from -800 pA to +800 pA, usually in steps of 50 pA. Minimal and maximal values were age-dependent and chosen such that a complete V-I curve and the cell's

firing behavior could be retrieved. Signals were not pre-filtered by the amplifier and digitized with a sampling frequency of 10 kHz.

Drugs

Drugs for pharmacological experiments were applied to the cell through the bath solution. Inward rectifier potassium channels were suppressed with 50 μM BaCl_2 . Hyperpolarization-activated channel I_h was blocked by 50 μM ZD7288 (4-ethylphenylamino-1,2-dimethyl-6-methylaminopyrimidinium chloride, Tocris, MO, USA). Sodium channels were nonspecifically blocked by 1 μM tetrodotoxin (TTX; Sigma, MO, USA); persistent sodium channels were blocked with 200 μM phenytoin (5,5-diphenylhydantoin-Na; Sigma, MO, USA).

Slice fixation and reconstruction of cell morphologies

Cells were filled with biocytin through the patch pipette for retrieval of cell morphologies (Horikawa & Armstrong, 1988). Following recording, slices were fixed at 4°C for at least 24 h in 100 mM phosphate-buffered saline (PBS, pH 7.4) containing 4% paraformaldehyde (PFA). After quenching in PBS containing 3% H_2O_2 for 25 min and permeabilization with 2% Triton in PBS for 1 h, slices were incubated overnight at 4°C in PBS-avidin-biotylated horseradish peroxidase (ABC Kit; Vector Labs, CA, USA) containing 1% Triton X100. Slices were then reacted using 3,3-diaminobezidine (DAB) as a chromogen under light microscopic control until dendritic arborisation was clearly visible. After several rinses in PBS they were mounted on slides, embedded in Moviol (Clariant, Sulzbach, Germany) and enclosed with a coverslip.

Morphological reconstructions were performed using a NeuroLucida system (MicroBrightField Inc., VT, USA). In brief, stained cells were viewed through a high magnification (100x, NA 1.25, plan oil immersion; Olympus, Tokyo, Japan) objective mounted on an Olympus BX40 bright field microscope (Olympus, Tokyo, Japan). Dendritic protrusions were traced by hand. The NeuroLucida software acquires the xy-position of the mouse pointer and the z-position via the focal position. Also, for every traced segment the thickness was measured. Cell morphologies were saved as ASCII files and converted to HOC format using a custom written converter program (kindly provided by Stefan Lang). Sholl analysis (Sholl, 1953) was performed using the NeuroExplorer software package (MicroBrightField Inc., VT, USA).

2.1.2 Data Analysis

All electrophysiological data were analyzed using customized routines written in Igor Pro 4.0 (Wavemetrics, OR, USA). Fitting routines for nonlinear functions utilize the Levenberg-Marquardt algorithm (Marquardt, 1963). All data (if not noted otherwise) are displayed as mean \pm standard error (sem). Number of cells n is given as $n(m)$, where m denotes the number of different animals the cells were measured from.

Significance tests

In pharmacological data, e. g. measurements from the same cell before and after application of drugs, the effectiveness of the applied drugs was tested using a paired t-test:

$$t = \frac{\overline{\Delta y} \sqrt{N}}{\sigma_{\Delta}} \quad (2.1)$$

Here, $\overline{\Delta y}$ is the mean difference between pairs of data points y , σ_{Δ} the standard deviation of that mean difference, and N the total number of data pairs. The criterion used for significance was $p < 0.05$; data were considered highly significant if $p < 0.01$. This test was chosen as the most rigorous. However, we have not shown that data points are normally distributed.

Monotonic functional correlations between parameters were tested using Spearman's correlation coefficient:

$$r_{SP} = \frac{\sum_i (rg(x_i) - \overline{rg_x})(rg(y_i) - \overline{rg_y})}{\sqrt{\sum_i (rg(x_i) - \overline{rg_x})^2 \sum_i (rg(y_i) - \overline{rg_y})^2}} \quad (2.2)$$

$rg()$ denotes the rank of the x or y data-point, respectively; bars denote averaged values.

Electrophysiological data

From a series of voltage traces, resting membrane potential V_{rest} was determined for each trace as average over the first 200 ms (2000 points) without current injection. Only cells with a drift of less or equal 1 mV were taken for analysis. Steady state voltage values used for V-I curves were computed as average of the last 100 ms (last 20%) of each trace during the current injection pulsed. Steady

2 Experiments

state voltage deflections ΔV were then calculated for each trace as the difference between steady-state voltage and V_{rest} . Relative sag in percent (a measure for Ih current; see chapter 2.2.2) was determined as difference between steady state voltage and minimum or maximum of the voltage trace (depending on whether hyper- or depolarizing currents were used), divided by the steady state voltage (Fig. 2.2A):

$$relative\ sag = \frac{extremum - steady\ state}{steady\ state} \quad (2.3)$$

Sag values associated with steady-state polarizations between -10 mV and +10 mV were not further analyzed since small amounts of noise (or spontaneous postsynaptic potentials) caused erroneous high sag values (Fig. 2.2B, grey bar).

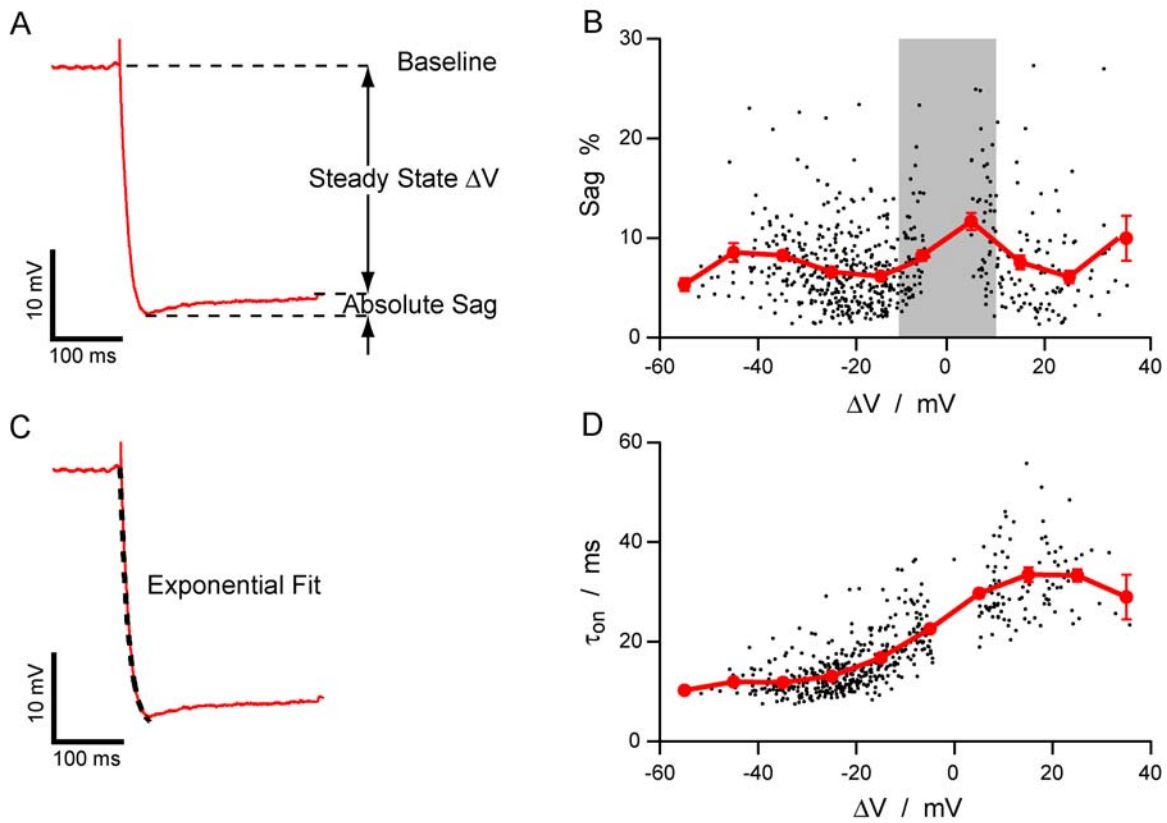


Fig. 2.2 Analysis of relative sag and onset time constant. **A**, example voltage trace showing quantities used in formula 2.3 (baseline $V_{rest} = -76$ mV). **B**, resulting relative sag plotted versus steady state ΔV . Values between -10 and +10 mV (grey bar) were excluded. Mean values (red) were derived by averaging values in 10 mV bins. **C**, exponential fit (black broken line) to voltage trace between stimulus onset and minimum of trace. **D**, onset time constants plotted τ_{on} versus steady state polarization. Mean values (red) were derived by averaging values in 10 mV bins.

Onset time constants τ_{on} were measured by fitting an exponential function to the voltage trace between current onset and minimum or maximum of hyperpolarized and depolarized traces, respectively. Here, the first 0.5 ms after stimulus onset were excluded because of the stimulation artifact (Fig. 2.2C). Note that, due to the activation of I_h -current, a systematic error is included into the measurement of τ_{on} , leaving it as an upper estimate of the cell's onset time constant. Steady state voltages, τ_{on} and sag values of traces with action potential (AP) were not considered for analysis of sub-threshold properties.

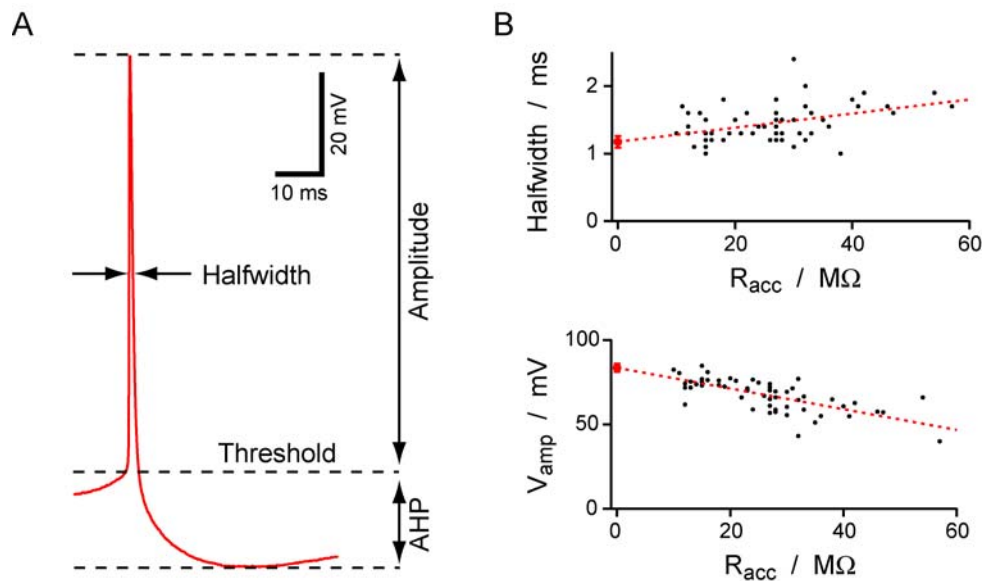


Fig. 2.3 Measuring action potential (AP) parameters. **A**, single AP and derived values. Threshold V_{thresh} was defined as absolute voltage at the inflection point. **B**, example plot of AP halfwidth (upper panel) and amplitude (lower panel) plotted versus access resistance for the p14 age group. Broken red lines show linear regression fits. Y-axis intercepts were accepted as halfwidth and amplitude V_{amp} for further analysis.

AP parameters were measured for the first AP elicited ever in a series of current injections except in cases when a doublet was fired first, as the second AP makes it impossible to determine the after-hyperpolarization. Instead, in these cases the first singular AP was used. Threshold voltage V_{thresh} was measured at the inflection point (point of largest second derivative before AP peak); amplitude V_{amp} was measured as the difference between V_{thresh} and the peak voltage of the AP; halfwidth was measured at half voltage difference between V_{thresh} and maximum of AP; after-hyperpolarization V_{AHP} was measured as the difference between V_{thresh} and the voltage minimum following an AP (Fig. 2.3A). Because

we observed a clear dependency of V_{amp} and halfwidth on access resistance R_{acc} , values were pooled for each age group and subsequently extrapolated to $R_{acc} = 0 \text{ M}\Omega$ using linear regression. Error bars at $R_{acc} = 0 \text{ M}\Omega$ were determined from the linear regression (Fig. 2.3B).

2.2 Experimental results

2.2.1 Morphological changes during development

We first analyzed to what extent L2/3 pyramidal neurons change their overall morphology during the first weeks of postnatal development. During whole-cell recordings, L2/3 cells were filled with biocytin and histologically reconstructed.

The main distinguishing feature of L2 from L3 cells are their respective morphologies and their position within the neocortex. Fig. 2.4 shows a series of example cells from different ages, marked as L2 and L3 cells based on the shape of their apical dendrite: While L2 cells usually only had a short apical trunk, their apical tuft reached out farther laterally compared to their basal dendrites, while

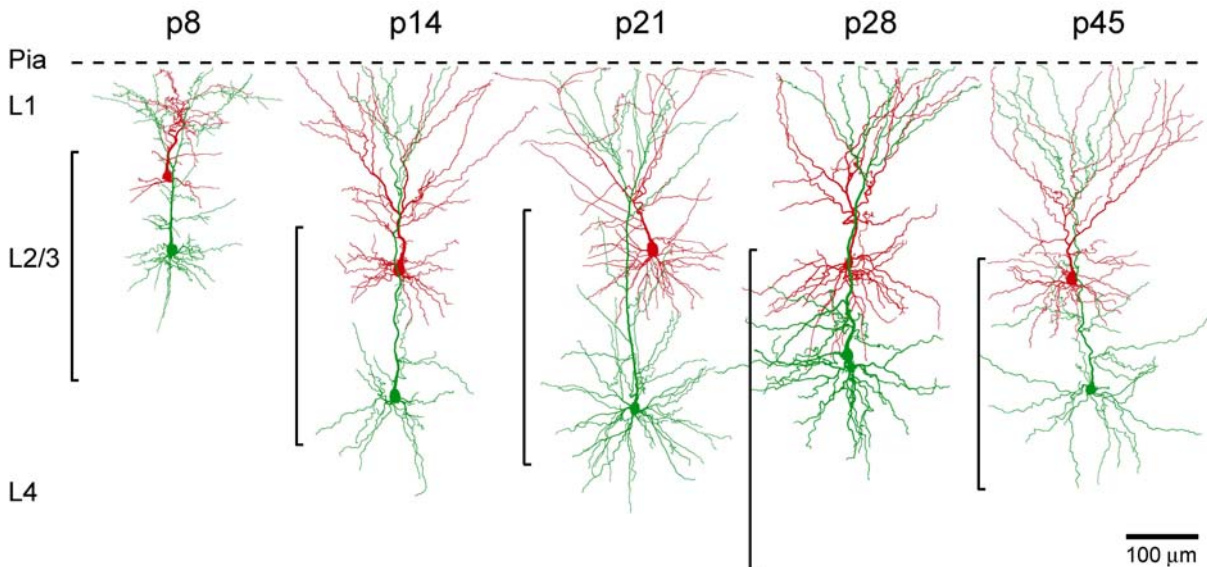


Fig. 2.4 Examples of reconstructed morphologies. L2 cells are shown in red, L3 cells in green, based on shape of apical dendrite. Broken black line shows pial surface of the cortex. Black bars show range of depth of measured cells.

the opposite was true for L3 pyramidal cells (Feldmeyer, personal communication). Variability in morphological appearance was high though, especially when determining the layer from depth beneath pial surface.

In order to quantify morphological changes due to development, morphologies were converted to hoc-files and read into the NEURON program. Fig. 2.5 shows changes in dendritic lengths (basal and apical), which is important for estimating the total synaptic input onto the dendritic tree, and changes in surface area, which allows an estimate of current densities. Measuring surface area is difficult, though, as obtaining diameters by brightfield light microscopy is bound to errors due to resolution, and spines add their surface at least partially to that of the respective dendritic arbor.

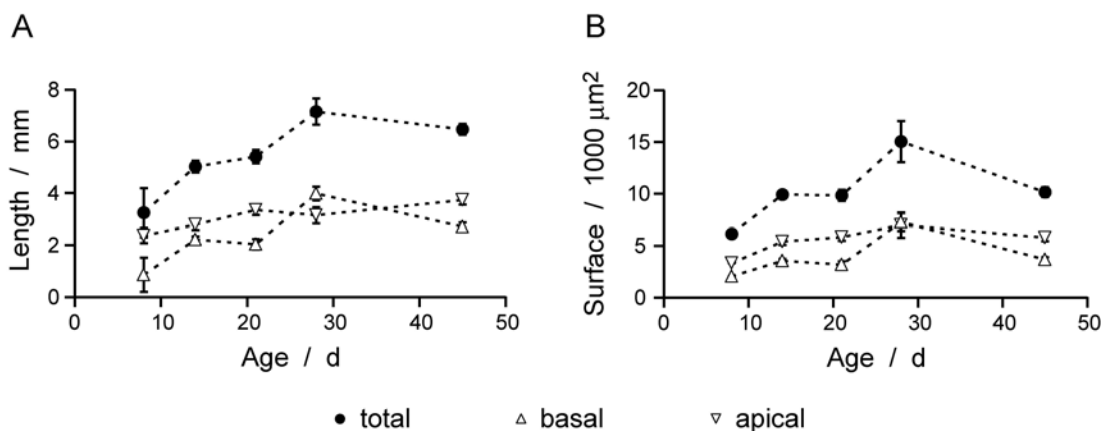


Fig. 2.5 Morphological parameters measured in NEURON from all reconstructed cells. A, length of dendritic protrusions. B, surface areas. See legend at bottom of graph.

As can be seen from Fig. 2.5, morphological maturation took place until p28, judged by dendritic length. There was no significant difference between total length of basal and apical dendrites. Dendritic surface area did change accordingly compared to dendritic length. One has to keep in mind, though, that some dendrites might be cut during the slicing procedure. The length of basal dendrites in particular might have been underestimated since somata were invariably close to the slice surface. This is especially true for p45-cells, as imaging using IR-DIC becomes more difficult due to myelination of axons as age increases. This makes it more likely that more basal dendritic processes of p45 cells were cut as somata lay closer to the slice surface.

Sholl analysis

For a more detailed analysis of morphologies, we performed a Sholl analysis (Sholl, 1953) utilizing the NeuroExplorer software package (MicroBrightField Inc., VT, USA). Briefly, a series of concentric spheres of increasing radius r (difference $\Delta r = 10 \mu\text{m}$) were placed around the center of the soma, and the number of nodes (branchpoints), endings and total dendritic length per sphere volume were measured as a function of r .

The results of the Sholl analysis are shown in Figs. 2.6 and 2.7. Consistent with the analysis of total dendritic length (Fig. 2.5), most morphological changes take place between p8 and p14. All values show a bimodal distribution for apical dendrites, while for basal dendrites only one mode was observed. Complexity (as measured of total numbers of nodes and endpoints) stayed constant for basal dendrites, while for apical dendrites the complexity seems to decrease from p8 to p14. However, reconstruction of p8 cells was difficult because of stained neighboring L2/3 pyramidal cells. The staining of nearby cells can have different reasons: (1) as a small positive

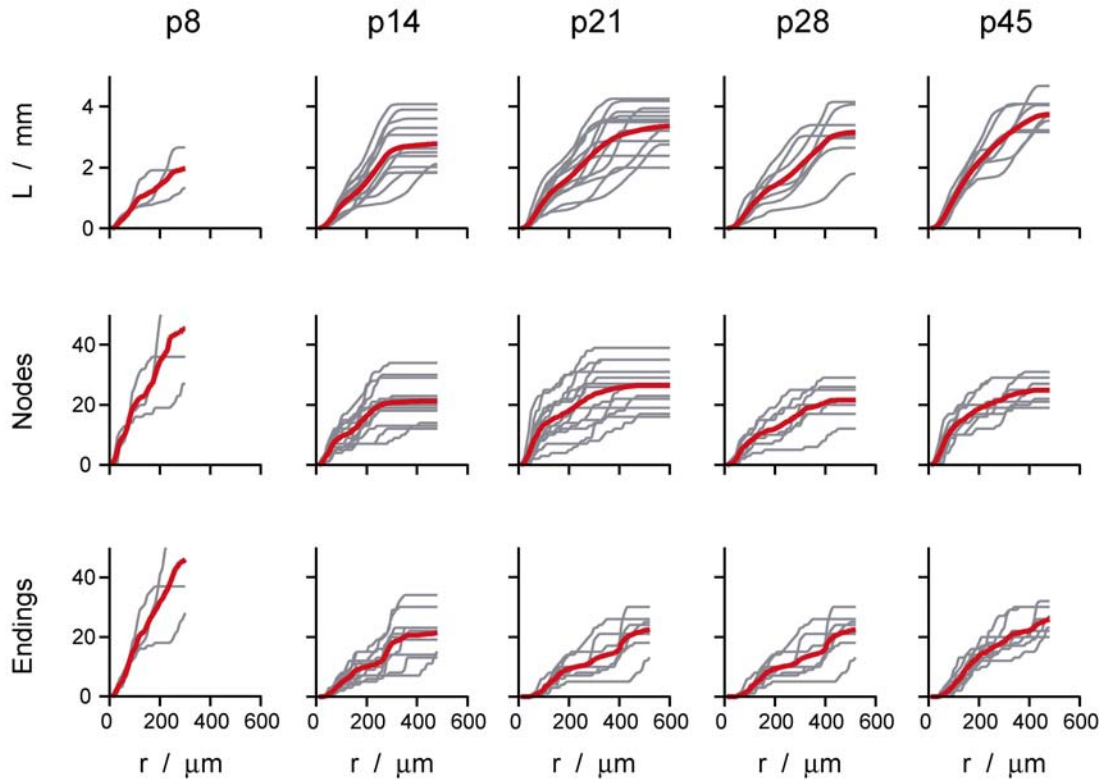


Fig. 2.6 Results of Sholl analysis for apical dendrites. Cumulative plot of total dendritic length L , number of nodes and number of endings versus sphere radius r . Grey, values for single cells; red, averages for each age-group. Error bars were omitted for clearness.

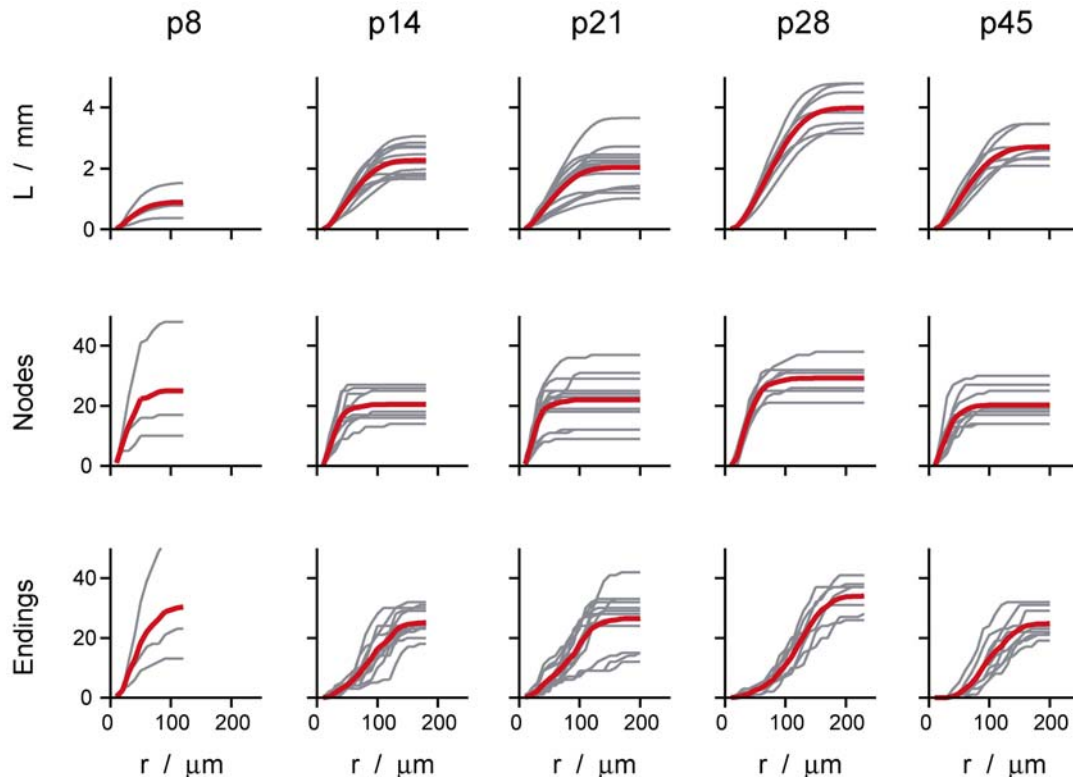


Fig. 2.7 Results of Sholl analysis for basal dendrites. Cumulative plot of total dendritic length L , number of nodes and number of endings versus sphere radius r . Grey, values for single cells; red, averages for each age-group. Error bars were omitted for clearness.

pressure is applied at the pipette's tip when it is moved into the slice, in very young animals this might be sufficient to slightly disrupt the cell membrane so that small amounts of biocytin may enter the cell; (2) biocytin is transported via gap junctions, which are present with an increased number in young animals (Connors et al., 1983; Rorig et al., 1995; Yuste et al., 1995; for a review see Bruzzone & Dermietzel, 2006), from the primarily stained cell to neighboring cells. One way or the other, disentangling of dendrites was difficult and small dendritic processes from other cells might have been accidentally appended to the cell under investigation, thereby artificially increasing the complexity. Also, filopodia might have been mistaken for small dendritic processes.

As the Sholl analysis of dendritic length and complexity did not disclose a clear difference between L2 and L3 pyramidal cells, an additional analysis was performed based on the number of intersections per sphere of basal dendrites (Sholl, 1953). Empirically, different cell types can be distinguished by calculating the slope b of a logarithmic plot of the number of intersections N_{Int} of a given sphere, divided by the volume V of that sphere:

2 Experiments

$$\log \frac{N_{Int}}{V} = a + br \quad (2.4)$$

The results are shown in Fig. 2.8. While the y -axis intercept stayed constant with age (Fig. 2.8C), the slope became shallower (Fig. 2.8B). The analysis did not reveal two populations. We therefore conclude that based on their basal dendritic morphology L2 and L3 pyramidal cells cannot be distinguished. However, we cannot exclude differences based on apical tuft morphologies.

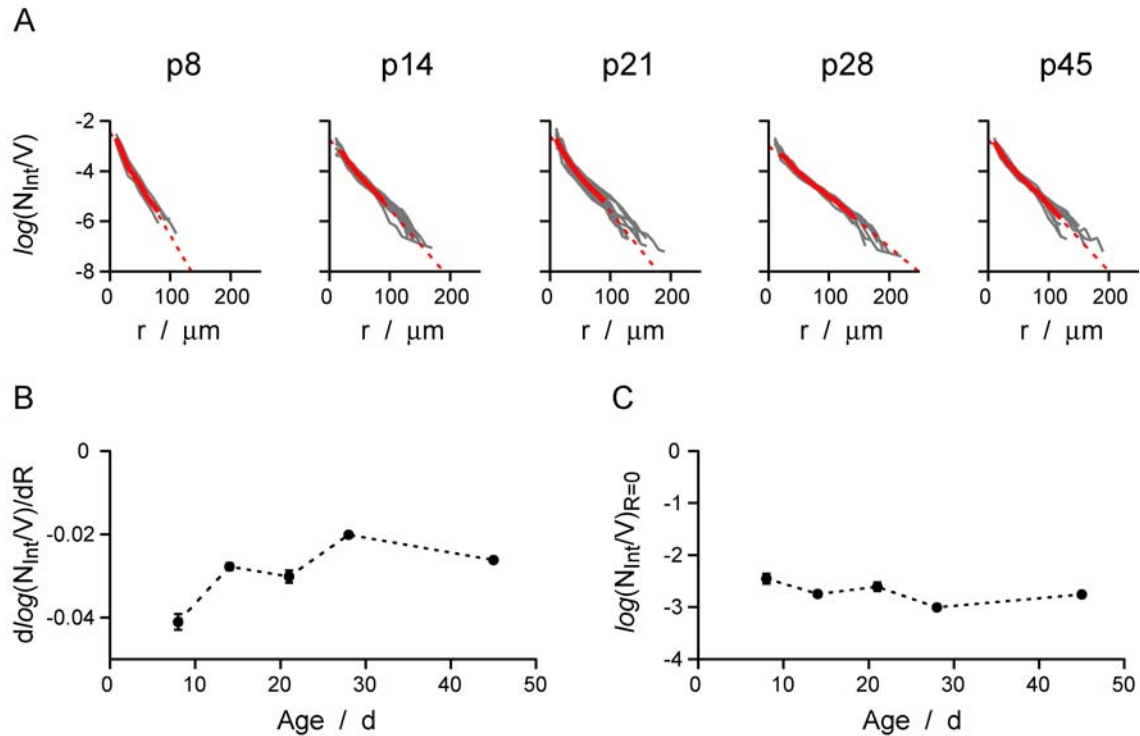


Fig. 2.8 Analysis of intersections per volume for basal dendrites. **A**, log-plot of intersections per volume against radius of respective sphere for different age groups. Thick red line, average of single cells (grey lines); broken red line, linear regression fit to average. **B**, slope of linear fits versus ages. **C**, y -axis intercepts of linear fits versus ages.

In conclusion, most morphological changes are finished between p14 and p21. These changes effect dendritic length and thereby the receptive volume, but not the complexity of the dendritic sub-trees. In all age groups, no clearly quantifiable differences were found between L2 and L3 pyramidal cells.

2.2.2 Sub-threshold properties of L2/3 pyramidal cells

Age-dependence of input resistance and anomalous rectification

We next characterized the sub-threshold voltage-current (V-I) relationship of L2/3 pyramidal neurons using long (500 ms) somatic current injections. Fig. 2.9 shows examples of original data obtained from whole-cell recordings of cells at different developmental stages. The corresponding steady-state V-I relationships are plotted as the steady-state voltage deflection versus injected current.

We analyzed the cell's input resistance R_{in} , which is the slope of the V-I relationship at resting membrane potential V_{rest} , and the rectification properties. Equally spaced current injections did not elicit equally spaced voltage responses at the soma of L2/3 pyramidal cells. Instead of outward rectification as would be appropriate for the ion concentration gradients across the membrane and a K^+ leak current, we generally observed inward rectification. Because this behavior is contradictory to a passive scenario following equation 1.7, it is termed anomalous rectification (AR).

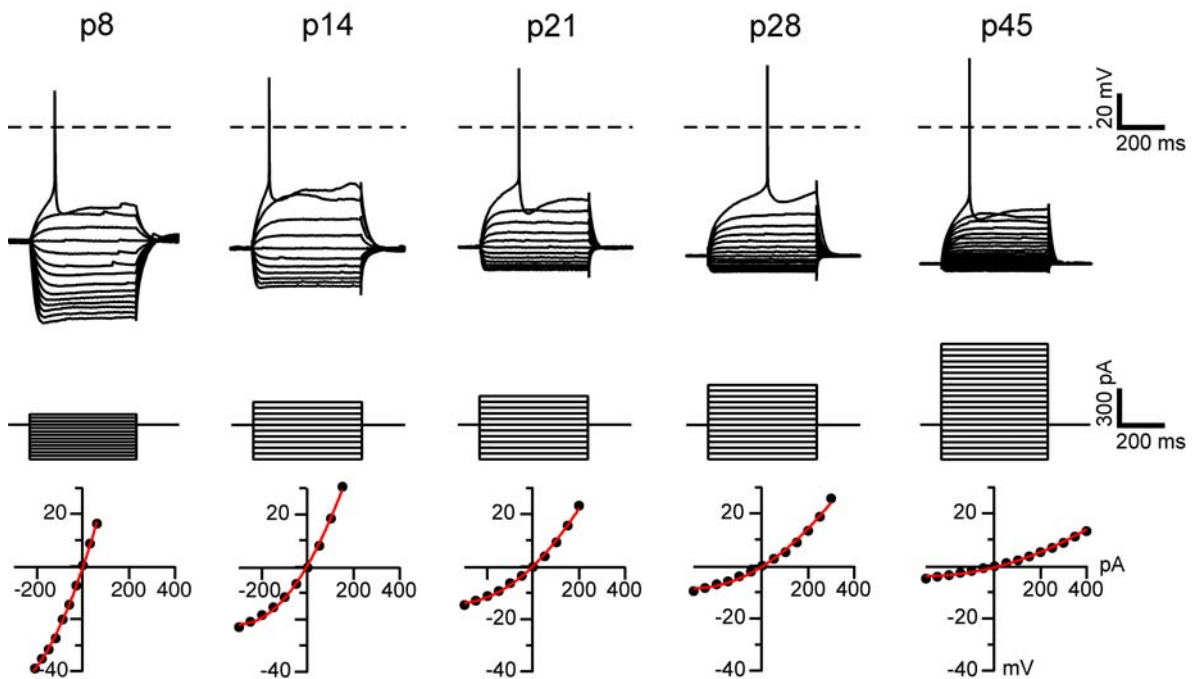


Fig. 2.9 Sub-threshold properties of L2/3 pyramidal cells during development. Upper row, examples of whole-cell recordings from cells at different ages. Broken line is 0 mV. Middle, somatic current injections leading to the voltage traces in upper row. Bottom, steady-state voltage deflections from resting potential following current injections. Axis intercept at 0 mV and 0 pA. Red line is the best fit using equation 2.5.

2 Experiments

In order to quantitatively assess AR, V-I-curves were fitted by the simplest non-linear function, a second order Taylor series expansion around resting potential (Waters & Helmchen, 2006):

$$\Delta V(I) = R_{in} I + c_{AR} I^2 \quad (2.5)$$

where ΔV is the voltage deflection from resting membrane potential. R_{in} denotes the somatic input resistance at resting membrane potential and c_{AR} is a rectification parameter, i. e. the deviation from ohmic behavior. Positive values of c_{AR} correspond to a V-I-relationship with positive curvature (increasing slope resistance, i.e. inward rectification) as observed in L2/3 pyramidal neurons.

To quantify in detail the age dependency of R_{in} and c_{AR} in L2/3 pyramidal cells, we performed the experiments described above for rats at ages postnatal day 8 (p8) ($n = 27$ (from 5 animals)), p14 ($n = 57$ (16)), p21 ($n = 16$ (3)), p28 ($n = 33$ (13)) and p45 ($n = 9$ (3)). A strong decrease of R_{in} from $217 \pm 15 \text{ M}\Omega$ to $60 \pm 7 \text{ M}\Omega$ was observed between p8 and p45 ($p < 0.01$). This decrease could be well approximated by an exponential curve with a time constant of around ten days (9.4 ± 2.7 days). The curve levels out at $47 \pm 16 \text{ M}\Omega$ (Fig. 2.10A, red curve). During the same period of development, c_{AR} also showed a large reduction: While at p8 the c_{AR} -value is $171 \pm 27 \text{ M}\Omega/\text{nA}$, it decreased over a period of a few days around p21 to a steady value of $39 \pm 4 \text{ M}\Omega/\text{nA}$ ($p < 0.01$, Fig. 2.10B).

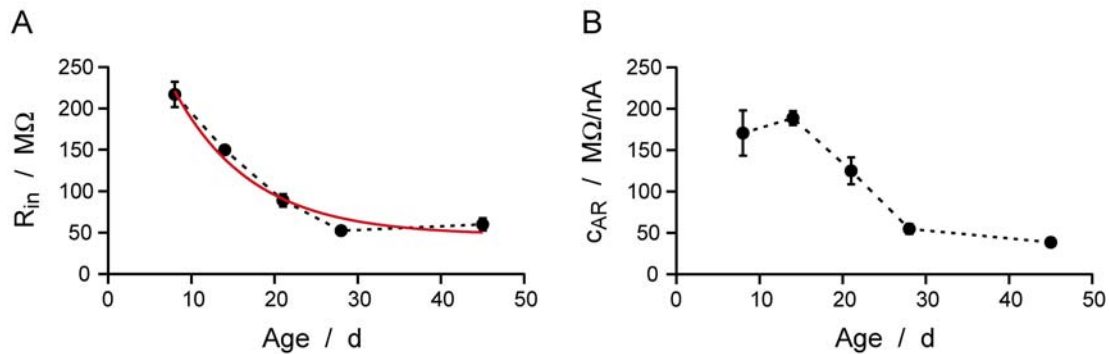


Fig. 2.10 Age dependencies of input resistance and anomalous rectification. **A**, R_{in} versus age. Exponential fit in red. **B**, c_{AR} versus age.

We showed here that L2/3 pyramidal neurons markedly change their basic biophysical properties during the first postnatal weeks. As will be further discussed throughout the thesis, these changes should have pronounced influence on how L2/3 pyramids act within their local networks.

Cells become more hyperpolarized as they mature

The resting membrane potential V_{rest} shifted to more hyperpolarized values as the L2/3 cells matured: -64 ± 1 mV at p8 and -80 ± 2 mV at p45 ($p < 0.01$). Again, this can be fitted by a single exponential with a steady state value of -80 ± 1 mV and a decay time constant of 8 ± 1 days (Fig. 2.11). A change in V_{rest} may indicate changes in the density and composition of ion channels in the membrane, which would be consistent with the changes in input resistance (see chapter 2.3.3).

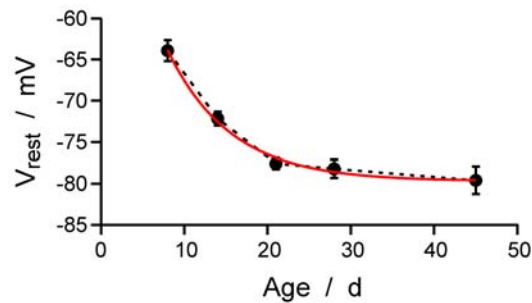


Fig. 2.11 Resting membrane potential versus age. Red line depicts best fit using a mono-exponential function.

	p8	p14	p21	p28	p45
V_{rest} / mV	-64 ± 1	-72 ± 1	-78 ± 1	-79 ± 1	-80 ± 2
R_{in} / M Ω	217 ± 15	150 ± 4	89 ± 8	55 ± 4	60 ± 7
c_{AR} / M Ω /nA	171 ± 27	189 ± 8	125 ± 16	53 ± 5	39 ± 4

Table 2.1 Basic sub-threshold properties of L2/3 pyramidal cells at different ages.

The time constant of voltage response is not constant

The observed change in slope resistance should lead to a change in membrane time constant, τ_m . Since this time constant was not measured exactly the onset time constant at the soma, τ_{on} , was taken instead (see Fig. 2.1). Exact measurement requires the separation of all contributions of longer time constants that stem from the fact that neurons, mainly due to dendritic protrusions, do not behave like a single, isopotential compartment (“peeling method”; Koch, 1999). Since the time constant of an RC circuit is given by $\tau = R \cdot C$, a decrease in τ

2 Experiments

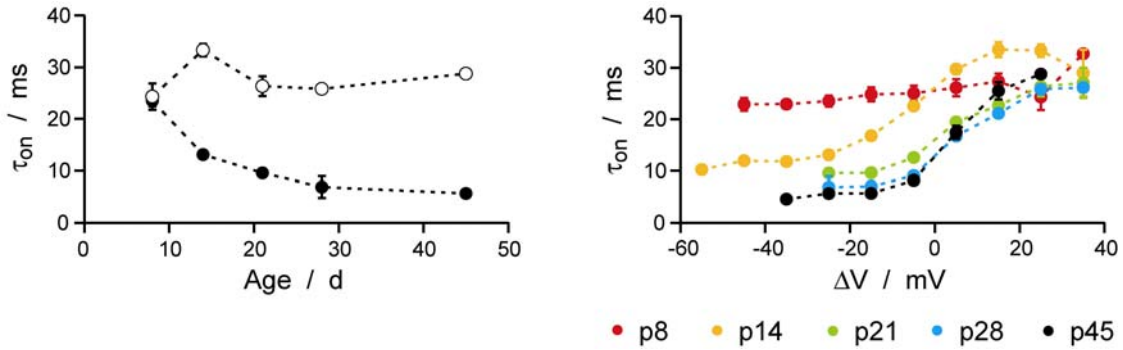


Fig. 2.12 Onset time constant τ_{on} versus polarization. Left panel, τ_{on} from the bins $-30 \text{ mV} < \Delta V < -20 \text{ mV}$ (filled circles) and $20 \text{ mV} < \Delta V < 30 \text{ mV}$ (open circles) versus age. Right panel, τ_{on} versus ΔV for all ages (color-coded).

indicates a decrease in either R or C . The membrane capacity can be considered as constant, leaving only a change in membrane resistance. The sigmoidal shape of the curves depicted in Fig. 2.12 thus are consistent with the decrease in R_{in} observed in the V-I relationships in the hyperpolarized regime. Note that for the youngest animals this behavior is almost not present whereas for animals older than p21 the data settle to the same curve. The decrease in R_{in} and τ_{on} with hyperpolarization would be consistent with a voltage-dependent channel that activates as membrane potential moves to more hyperpolarized values. One obvious candidate would be the Ih current, which will be examined in the next paragraph.

Little sag in L2/3 pyramidal cells

Another characteristic of subthreshold voltage responses is the so-called sag, a small hyperpolarization preceding steady-state polarization following negative current injections. This effect is attributed to the rather slow activation of the hyperpolarization-activated or “queer” current, Ih, which mediates a partial repolarization of the cell towards resting potential.

We found that relative sag is not very prominent in L2/3 pyramidal cells (usually between 5 to 10 %). Fig. 2.13 shows the development of the sag as the cells mature. The two values around $\Delta V = 0$ are to be considered with caution since polarizations are small and the way the sag is analyzed does not distinguish real sag from noise. Our finding is consistent with previous studies on L2/3 neurons and suggests that, unlike L5 pyramidal neurons – Ih is not expressed to a high level in L2/3 pyramidal cells (see chapters 2.3.2 and 3.2.2).

Sag in the depolarizing regime might have two different causes: First, Ih deactivates rather slowly, thus following the membrane voltage with a delay, and second, partial activation of Na⁺ currents not sufficient for AP generation might lead to a positive initial “bump” superimposed on the depolarization timecourse.

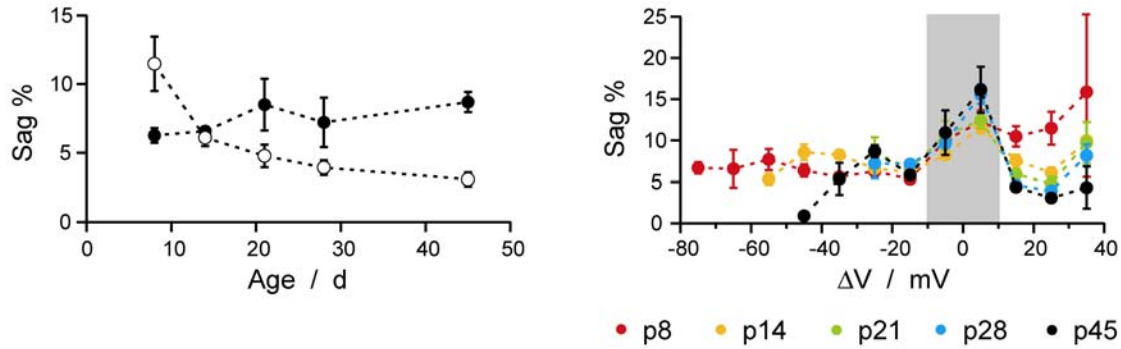


Fig. 2.13 Relative sag versus polarization. Left panel, relative sag from the bins $-30 \text{ mV} < \Delta V < -20 \text{ mV}$ (filled circles) and $20 \text{ mV} < \Delta V < 30 \text{ mV}$ (open circles) versus age. Right panel, relative sag versus ΔV for all ages (color-coded). Points around resting potential ($\Delta V = 0$, grey area) are difficult to interpret due to noise.

Pyramidal cells from L2 and L3 do not differ in their subthreshold properties

As was shown in chapter 2.2.1, L2 and L3 cells do not differ significantly in their shape. However, this does not exclude differences in their electrophysiological behavior. In order to address this question a Spearman’s rank test (eq. 2.2) was performed, comparing sub-threshold electrophysiological parameters with the soma’s distance to pial surface d_{pia} . At age p14, a highly significant negative correlation between c_{AR} and d_{pia} was found ($r_{SP} = -0.44$, $p = 0.0049$) and a significant ($p = 0.0141$) negative correlation between R_{in} and d_{pia} ($r_{SP} = -0.39$). At p45, V_{rest} was highly significantly correlated to d_{pia} ($r_{SP} = -0.93$, $p = 0.0008$). Additionally, a significant negative correlation was found for R_{in} ($r_{SP} = -0.82$, $p = 0.0108$) and for c_{AR} ($r_{SP} = -0.75$, $p = 0.0255$). These correlations at p45 might be due to small sample size, though. No significant correlations were found at other ages examined (Table 2.2).

In conclusion, no consistent (similar r_{SP} and significance) correlations between electrophysiological and morphological parameters were found over the ages examined, meaning that L2 and L3 pyramidal cells cannot be distinguished by their sub-threshold properties alone and will behave the same way in respect to somatic integration. Nevertheless, we observe the trend that R_{in}

2 Experiments

and C_{AR} decrease with d_{pia} . This notion is coherent with the idea that proximal apical diameter increases with depth, thereby adding additional current drain to the cell and decreasing R_{in} .

	p8	p14	p21	p28	p45
V_{rest}	-0.1256	-0.0437	0.415	0.239	-0.9333
	0.5325	0.789	0.1099	0.1734	0.0008
R_{in}	-0.2569	-0.3854	-0.3782	-0.838	-0.8167
	0.1958	0.0141	0.1486	0.6374	0.0108
C_{AR}	-0.2438	-0.4363	-0.4371	-0.1526	-0.75
	0.3204	0.0049	0.0905	0.389	0.0255

Table 2.2 Correlation coefficients and p-values for Spearman’s rank test of sub-threshold electrophysiological parameters versus d_{pia} . Significant ($p < 0.05$) correlations are marked in orange, highly significant ($p < 0.01$) correlations are marked in red.

2.2.3 Supra-threshold properties of L2/3 pyramidal cells

Action potentials become larger and sharper as the cells mature

Besides the sub-threshold properties we also examined the overall firing behavior of L2/3 pyramidal cells. The first question here was whether the waveform of action potentials (APs) changes while the cells mature. Several AP properties were examined: Threshold V_{thresh} for AP firing, AP amplitude V_{amp} , AP halfwidth and after-hyperpolarization V_{AHP} . Age-dependent changes of these properties are summarized in Fig. 2.14.

While resting membrane potential and the threshold for AP generation shifted in parallel to more hyperpolarized values as age increased, the absolute peak voltages of APs increased. These two effects lead to an increase in AP amplitude from 66 ± 1 mV at p8 to 94 ± 2 mV at p45 (Fig 2.14A). The after-hyperpolarization increases only slightly during this time span (Fig. 2.14C). Additionally, the AP half-width decreases by a factor of almost two: (1.4 ± 0.2) ms at p8 to (0.8 ± 0.1) ms at p45 (Fig. 2.14B). APs thus become larger and sharper as L2/3 pyramidal cells mature.

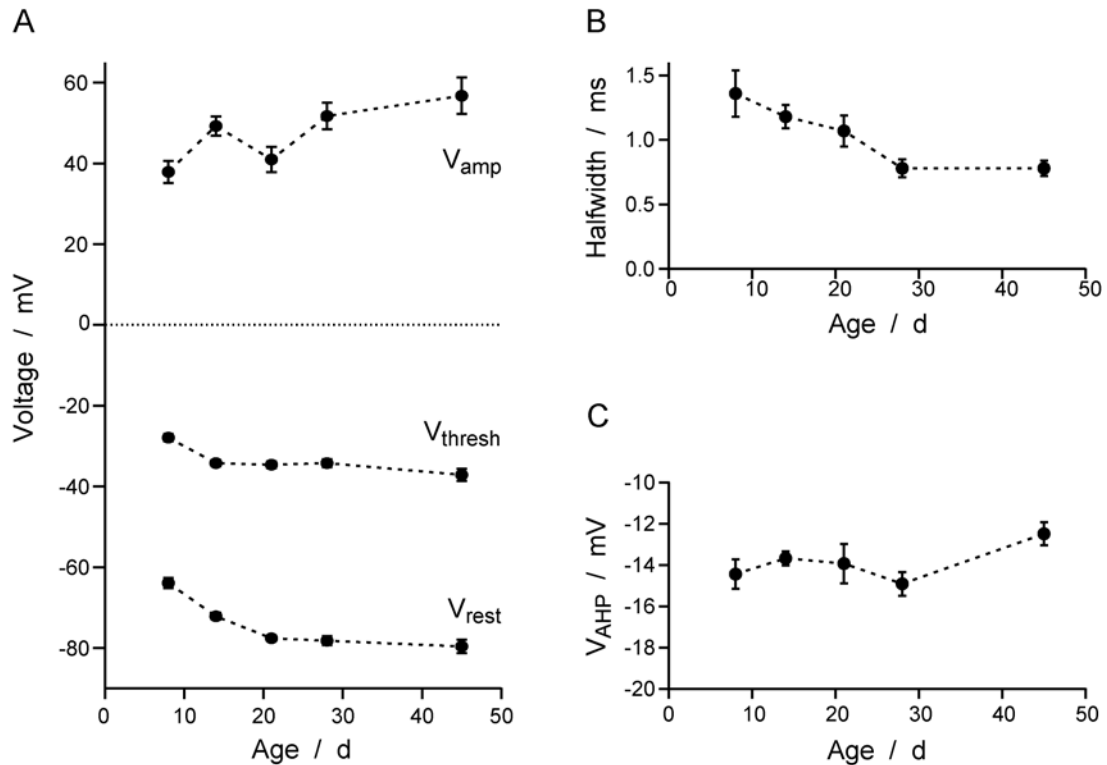


Fig. 2.14 Age-dependency of action potential properties. **A**, V_{rest} , V_{thresh} and V_{amp} plotted versus age. Error in peak amplitude is standard deviation, since the values stem from linear regression. **B**, AP halfwidth versus age. Displayed are means \pm standard deviation, since the values were obtained from linear regression. **C**, V_{AHP} versus age.

	p8	p14	p21	p28	p45
V_{thresh} / mV	-28 ± 1	-34 ± 1	-35 ± 1	-35 ± 1	-37 ± 2
V_{amp} / mV	66 ± 1	84 ± 0	76 ± 1	86 ± 1	94 ± 2
halfwidth / ms	1.4 ± 0.0	1.2 ± 0.0	1.1 ± 0.0	0.8 ± 0.0	0.8 ± 0.0
V_{AHP} / mV	-14 ± 1	-14 ± 0	-14 ± 1	-15 ± 1	-13 ± 1

Table 2.3 Supra-threshold properties of L2/3 pyramidal neurons at different ages

Firing behavior

In order to characterize the cell's ability to fire APs, steady state firing frequency was determined by calculating the inverse of the inter-spike interval (ISI) of the last two APs of an AP train. Only trains of more than three APs were taken into account, for the occurrence of doublets at the beginning of a train inevitably leads

to an overestimation of frequency. In Fig. 2.15, AP frequencies are displayed versus the current injected at the soma (so-called f-I curves). Variability is very high, seems to be non-Gaussian and most probably originates from two sources: (1) the steady state firing frequency might differ between cells; (2) variability in R_{in} and c_{AR} leads to different depolarization upon current injection and thus to different AP frequencies.

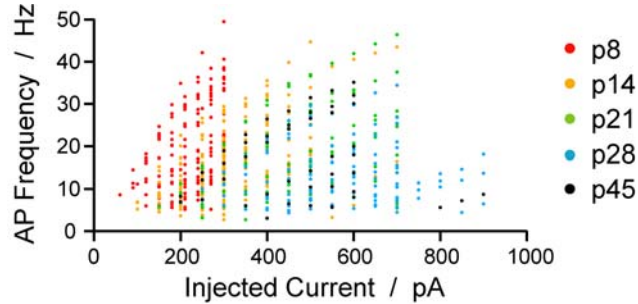


Fig. 2.15 AP frequencies versus somatically injected currents. Ages are color coded.

The f-I curves were analyzed using an exponential function of the form

$$f(I) = f_{\max} \left(1 - e^{-\frac{I-I_0}{I_c}} \right) \quad (2.6)$$

where f_{\max} is the saturation frequency, I_0 the minimal current needed for a single AP, and I_c the space constant. Results are shown in Fig. 2.16. While the saturation frequency f_{\max} stayed almost constant (40.2 ± 4.1 Hz at p8 and 31.2 ± 4.9 Hz at p45, $p = 0.28$), the minimal current needed to evoke an AP, I_0 , increased by a factor of roughly 3 from 124 ± 10 pA at p8 to 336 ± 81 pA at p45 (highly significant, $p < 0.01$). This increase is attributable to the decrease in R_{in} and c_{AR} . The space constant I_c shows a trend towards higher values as age increases (153 ± 21 pA at p8 versus 246 ± 49 pA at p45, $p = 0.057$) but with a maximum at p21 of 381 ± 49 pA which is highly significant versus the value at p8 ($p < 0.01$) but not p45 ($p = 0.099$).

Thus, f-I curves generally shift to the right and become steeper during development. This developmental profile indicates that the way L2/3 pyramidal cells integrate synaptic input as well as the resulting AP patterns *in vivo* will largely change during this period.

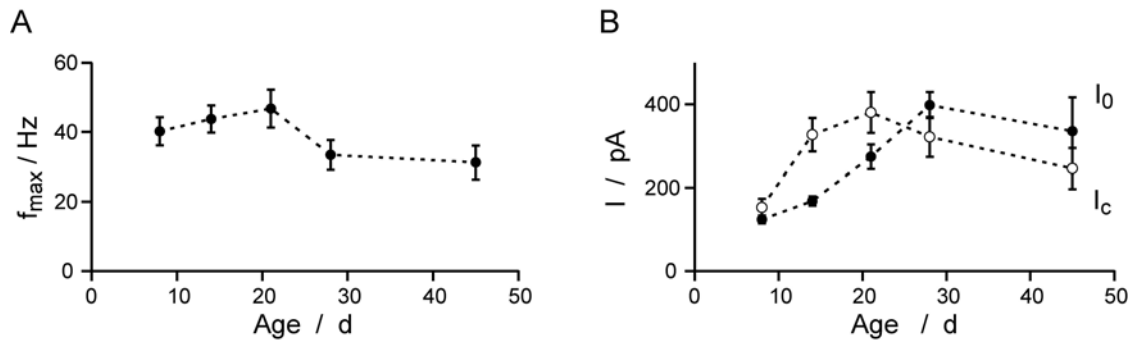


Fig. 2.16 Analysis of f-I curves using equation 2.6. **A**, saturation frequency f_{max} versus age. **B**, minimal current I_0 (closed circles) and space constant I_c (open circles) versus age.

L2 and L3 pyramidal cells do not differ in their supra-threshold properties

In order to assess whether AP waveforms differ between L2 and L3 pyramidal cells, we again calculated the Spearman correlation coefficients between supra-threshold parameters and d_{pia} . The results are listed in Table 2.4. Except for V_{thresh} at p45 ($r_{SP} = -0.85$, $p = 0.0061$), no significant correlations were found.

	p8	p14	p21	p28	p45
V_{thresh}	-0.044	0.127	-0.0015	0.044	-0.85
	0.8274	0.435	0.9957	0.8051	0.0061
V_{amp}^*	0.0293	0.2135	0.1179	-0.1645	0.1667
	0.8845	0.1858	0.6636	0.3524	0.6777
V_{AHP}	0.0509	-0.2948	-0.078	-0.1626	-0.0333
	0.8010	0.0648	0.774	0.3584	0.9484
$Halfwidth^*$	-0.0975	-0.1158	-0.0548		-0.4895
	0.6285	0.4767	0.8402		0.1828

Table 2.4 Correlation coefficients and p-values for Spearman's rank test of supra-threshold electrophysiological parameters versus D_{pia} . Significant ($p < 0.05$) correlations are marked in orange, highly significant ($p < 0.01$) correlations are marked in red.* V_{amp} and halfwidth are also correlated to R_{acc} .

In conclusion, during postnatal development L2/3 pyramidal cells show enhanced temporal fidelity in their responses to somatic current injection, with

reduced somatic time constant and sharper AP waveform. On the other hand, L2/3 cells become less excitable as they mature, which is reflected in the decrease in R_{in} and c_{AR} . Thus, more synaptic input is required to raise the membrane potential above V_{thresh} .

2.2.4 Pharmacological Experiments

We found that L2/3 pyramidal neurons display prominent anomalous rectification at all ages. Such rectifying properties can only be explained by the presence of voltage-gated channels, indicating that L2/3 neurons even near resting potential are not passive electric compartments. These non-passive properties may have a strong influence on how synaptic inputs are integrated in these cells, and we therefore next investigated which type of voltage-dependent current underlies AR. We tested three potential candidate currents, namely persistent sodium current (NaP), nonspecific hyperpolarization-activated current (Ih), and an inward-rectifying potassium current (KIR). Pharmacological experiments were performed at two postnatal ages, p14 and p28, to show that the same mechanism is responsible for anomalous rectification at different levels of cell maturation.

Persistent Na-channels are not responsible for anomalous rectification

One type of channel that could contribute to AR is the persistent Na-channel (NaP) (reviewed in Taylor, 1993). This channel is a non-inactivating channel that activates as the membrane is depolarized. Thereby the channel changes R_{in} in the depolarizing regime, whereas in the hyperpolarizing regime the neuron would exhibit a nearly passive behavior. Since the channel's reversal potential is well above 0 mV (equation 1.4), activation of NaP would lead to a constant influx of sodium ions, generating a current that further depolarizes the membrane, i. e. increasing the voltage deflection following current injection.

To test for this channel, the specific NaP-blocker phenytoin (PT, also used as an anti-epilepticum; Woodbury, 1980) was applied using a concentration of 200 μ M (Lampl et al., 1998). No significant changes in R_{in} and c_{AR} were observed (Fig. 2.17): R_{in} remained unchanged at age p14 (137 ± 14 M Ω versus 132 ± 13 M Ω , $p > 0.05$, paired t-test, $n = 5$ (from 2 animals)) and increased slightly at p28 (60 ± 14 M Ω versus 70 ± 16 M Ω , $p > 0.05$, $n = 6(3)$) while c_{AR} did decrease

slightly at p14 from $146 \pm 36 \text{ M}\Omega/\text{nA}$ to $120 \pm 25 \text{ M}\Omega/\text{nA}$ ($p > 0.05$, $n = 5(2)$) but increased at p28 from $76 \pm 15 \text{ M}\Omega/\text{nA}$ to $81 \pm 20 \text{ M}\Omega/\text{nA}$ ($p > 0.05$, $n = 6(3)$).

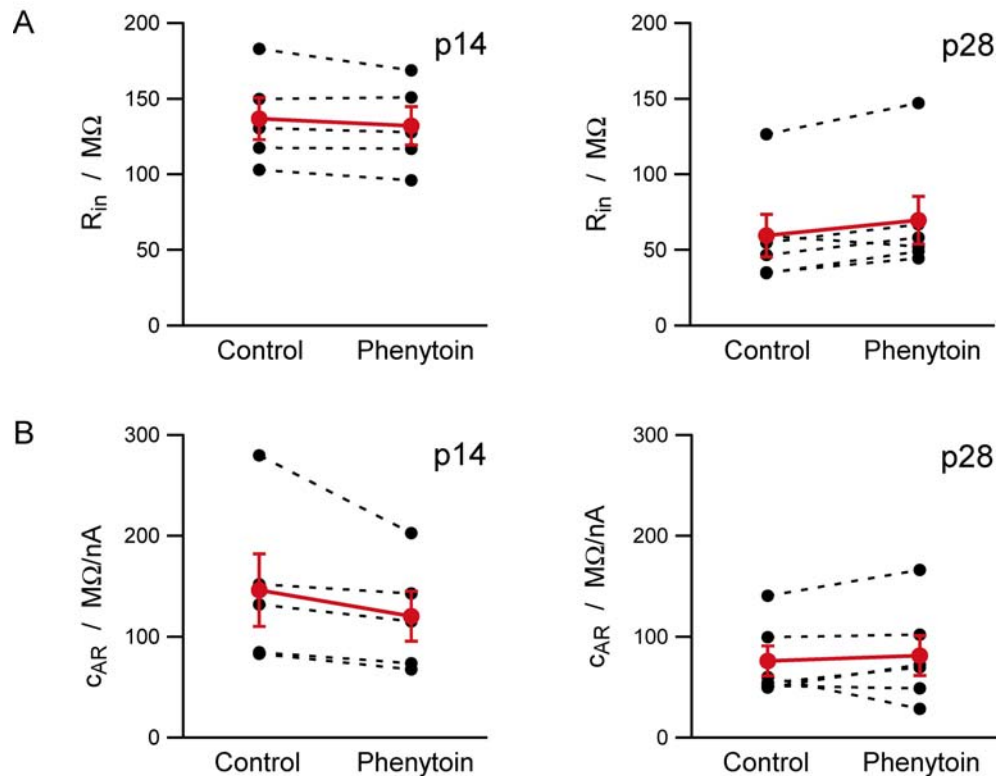


Fig. 2.17 Changes in sub-threshold behavior following application of $200 \mu\text{M}$ phenytoin. **A**, changes in R_{in} . **B**, changes in c_{AR} . Averaged data are displayed in red.

In order to check whether other, perhaps phenytoin-insensitive Na-channel might contribute to anomalous rectification, we also extracellularly applied $1 \mu\text{M}$ TTX (tetrodotoxin, a very potent Na-channel blocker extracted from the blowfish (fam. Tetraodontidae)) during recordings (reviewed in Marban et al., 1998; Fozzard & Hanck, 1996). The effectiveness of TTX-application was judged by the absence of APs even at high depolarizing current injections.

Application of TTX also did not show any significant effect on anomalous rectification as well as input resistance (Fig. 2.18): R_{in} decreased from $153 \pm 10 \text{ M}\Omega$ to $147 \pm 12 \text{ M}\Omega$ ($p > 0.05$, $n = 7(3)$) at p14 and from $40 \pm 3 \text{ M}\Omega$ to $38 \pm 2 \text{ M}\Omega$ ($p > 0.05$, $n = 7(2)$) at p28 while c_{AR} decreased at p14 from $147 \pm 17 \text{ M}\Omega/\text{nA}$ to $140 \pm 15 \text{ M}\Omega/\text{nA}$ ($p > 0.05$, $n = 7(3)$) and from $27 \pm 3 \text{ M}\Omega/\text{nA}$ to $22 \pm 2 \text{ M}\Omega/\text{nA}$ ($p > 0.05$, $n = 7(2)$) at p28. These results show that subthreshold activation of

2 Experiments

sodium currents is not a major determinant of rectification in L2/3 pyramidal neurons.

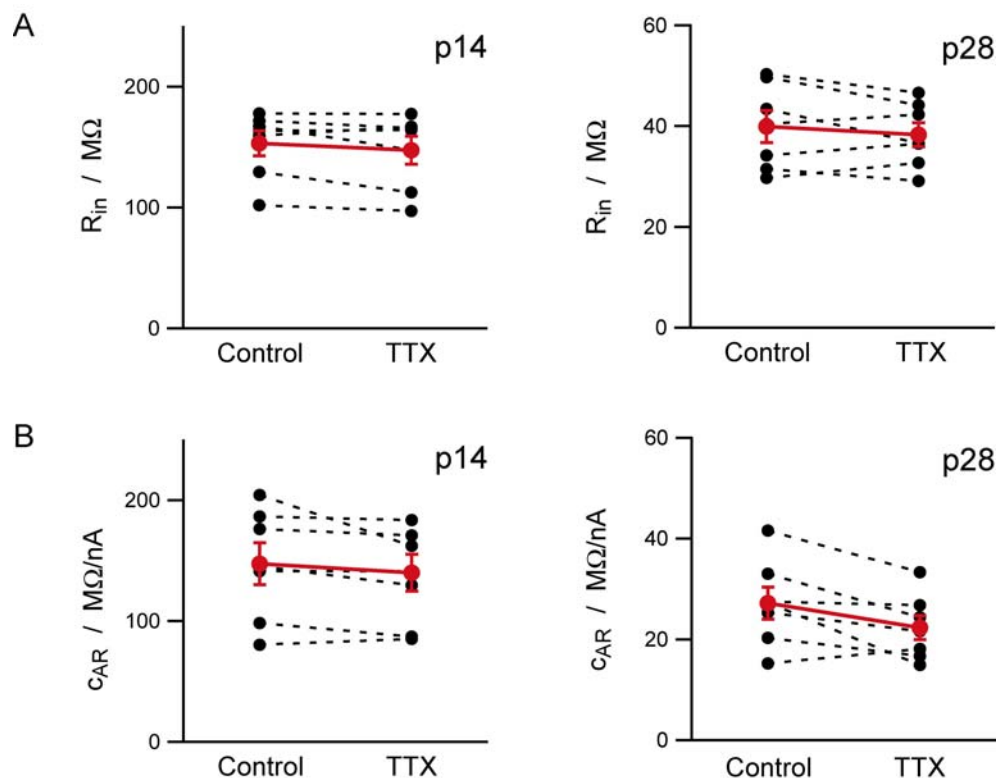


Fig. 2.18 Changes in subthreshold behavior following application of 1 μ M TTX. **A**, changes in R_{in} . **B**, changes in c_{AR} . Averaged data are displayed in red.

Application the of I_h blocker ZD7288 does not abolish anomalous rectification

Although hyperpolarization activated current I_h – as judged from the amount of sag – is less prominent in L2/3 compared to L5 pyramidal neurons it could still play a role in mediating anomalous rectification. In order to test this hypothesis the I_h blocker ZD7288 (BoSmith et al., 1993; Lüthi et al, 1998a) was applied in the bath solution. Effectiveness was judged by the absence of sag following hyperpolarizing current injections. However, in some cases it was difficult to judge whether sag was absent, since even after prolonged application of ZD7288 a kink seemed to be superimposed on the exponential curve expected for a merely passive cell (see Fig. 2.19A). While R_{in} increased following application of ZD7288 (at p14 from $157 \pm 17 M\Omega$ to $213 \pm 16 M\Omega$ ($p < 0.01$, $n = 6(3)$) and at p28 from $64 \pm 10 M\Omega$ to $114 \pm 5 M\Omega$ ($p > 0.05$, $n = 6(2)$); Fig 2.20A), no

significant changes in anomalous rectification could be observed after application of ZD7288: At p14, c_{AR} decreased from $163 \pm 23 \text{ M}\Omega/\text{nA}$ to $133 \pm 31 \text{ M}\Omega/\text{nA}$ ($p > 0.05$, $n = 6(3)$) but at p28 it increased from $44 \pm 5 \text{ M}\Omega/\text{nA}$ to $63 \pm 7 \text{ M}\Omega/\text{nA}$ ($p > 0.05$, $n = 6(2)$; Fig 2.20B). Note that the V-I curves are not completely linear (Fig. 2.19B). Instead, the curves seem to decompose into two linear components which meet at around 20 mV below resting potential. This effect makes the quadratic fit much worse than in the control situation, such that the values for R_{in} and c_{AR} have to be considered with caution.

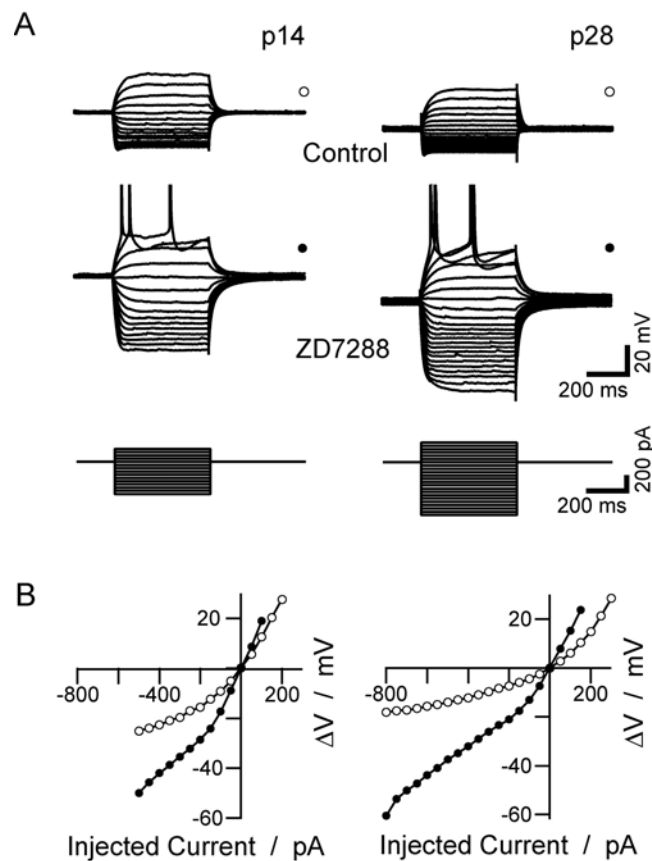


Fig. 2.19 Effect of $50 \mu\text{M}$ ZD7288 on sub-threshold voltage response at two different ages (p14 and p28). **A**, raw data traces before and after application of ZD7288 (APs are cut off at 0 mV) and current injections. **B**, steady-state VI-curves derived from raw traces (open circles: control; filled: $50 \mu\text{M}$ ZD7288).

Although ZD7288 seems to have an effect (if not significant) on the subthreshold behaviour of L2/3 pyramidal cells, interpretation of the data presented in Fig. 2.19 is not that straight forward: In addition to changes in R_{in}

2 Experiments

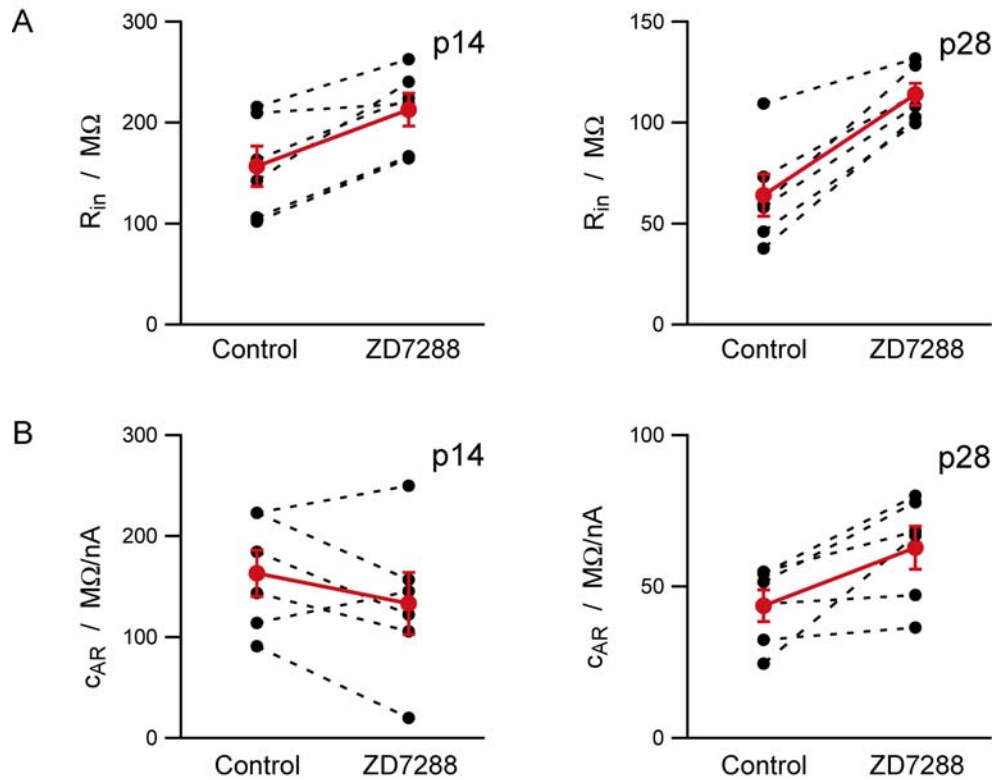


Fig. 2.20 Changes in subthreshold behavior following application of 50 μ M ZD7288. A, changes in R_{in} . B, changes in c_{AR} . Averaged data are displayed in red.

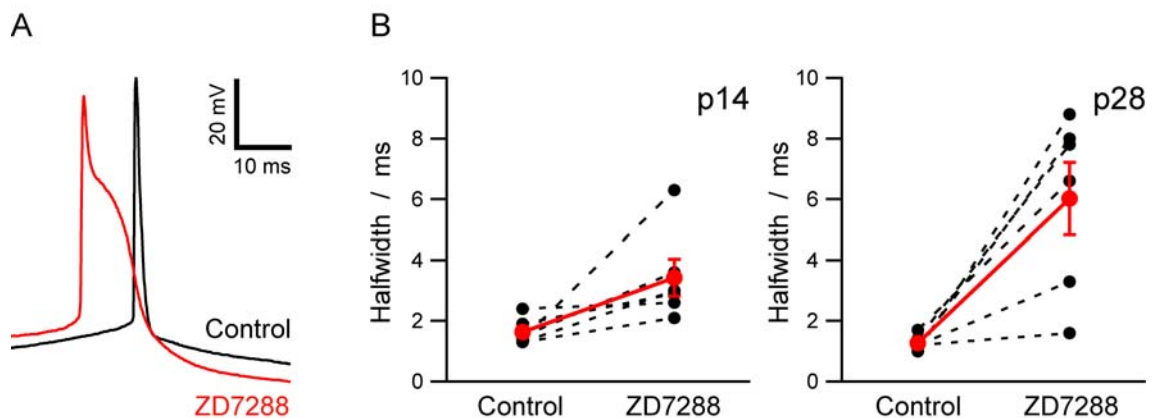


Fig. 2.21 Effect of 50 μ M ZD7288 on AP waveform. A, example of APs before (black) and after (red) application of ZD7288 (p28). Note that besides the effect on AP halfwidth the amplitude and shape in general is effected. B, effect of ZD7288 on AP halfwidth.

and c_{AR} a broadening of action potentials was observed (Fig 2.21). At p14, AP halfwidth increased from 1.6 ± 0.3 ms to 3.4 ± 0.6 ms ($p < 0.05$, $n = 6(3)$) and at p28 from 1.3 ± 0.1 ms to 6 ± 1.2 ms ($p = 0.01$, $n = 6(2)$). Thus, besides the well-known blocking of Ih, ZD7288 might also exert unspecific effects on other channels in L2/3 pyramidal cells, like delayed rectifier K-channels that are largely responsible for AP repolarization.

Blockage of KIR with 50 μ M BaCl₂ abolishes anomalous rectification

Following a publication by Day et al. (2006) one remaining candidate for mediating anomalous rectification was the inward rectifying K-channel (KIR). In order to test the hypothesis that KIR is responsible for anomalous rectification in

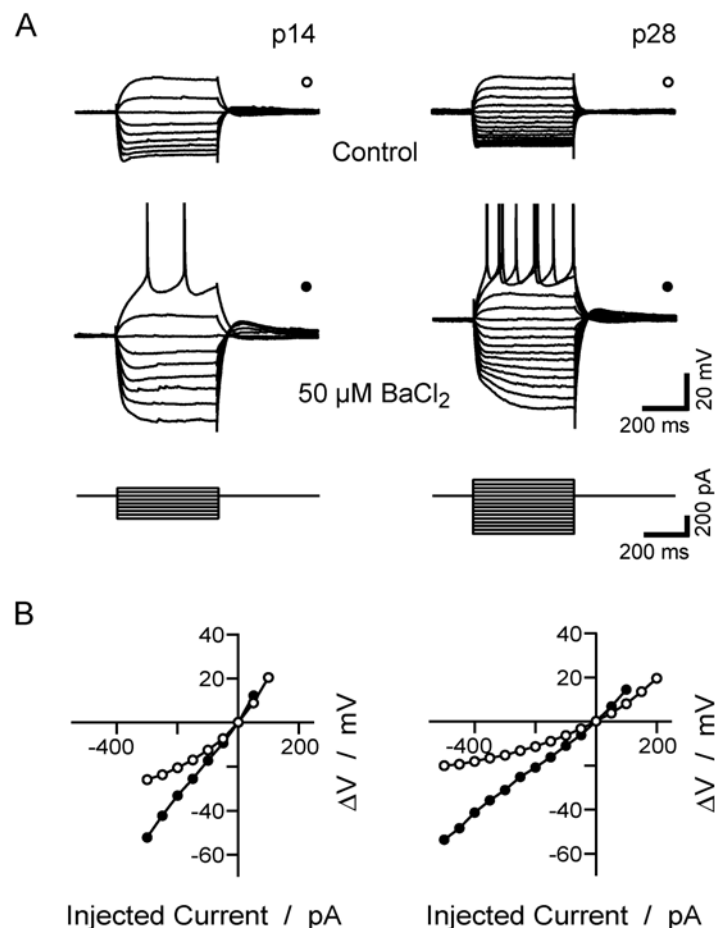


Fig. 2.22 Effect of 50 μ M BaCl₂ on sub-threshold voltage response at two different ages (p14 and p28). **A**, raw data traces before and after application of BaCl₂ and current injections (APs are cut off at 0 mV). Lower row, steady-state VI-curves derived from raw traces (open circles: control; filled: 50 μ M BaCl₂).

2 Experiments

L2/3 pyramidal neurons low concentration of Barium chloride (BaCl_2) was applied during current clamp experiments (Coetzee et al., 1999).

As can be seen in Fig. 2.23B, c_{AR} was significantly reduced for p14 from $243 \pm 13 \text{ M}\Omega/\text{nA}$ to $17 \pm 22 \text{ M}\Omega/\text{nA}$ ($p < 0.001$, $n = 16(5)$). For p28 the same tendency was observed although the change was not significant (from $43 \pm 5 \text{ M}\Omega/\text{nA}$ to $31 \pm 6 \text{ M}\Omega/\text{nA}$ ($p = 0.21$, $n = 10(3)$). This might be due to the fact that already in control experiments anomalous rectification is not very pronounced in p28 cells and thus a change to even smaller values is difficult to observe. In some experiments at p14 c_{AR} became negative, meaning the V-I-curve was bent into the opposite direction. At the same time, R_{in} increased for both ages: p14: from $161 \pm 7 \text{ M}\Omega$ to $206 \pm 10 \text{ M}\Omega$ ($p < 0.001$, $n = 16(5)$); p28: from $50 \pm 4 \text{ M}\Omega$ to $93 \pm 6 \text{ M}\Omega$ ($p < 0.005$, $n = 10(3)$; Fig. 2.23A).

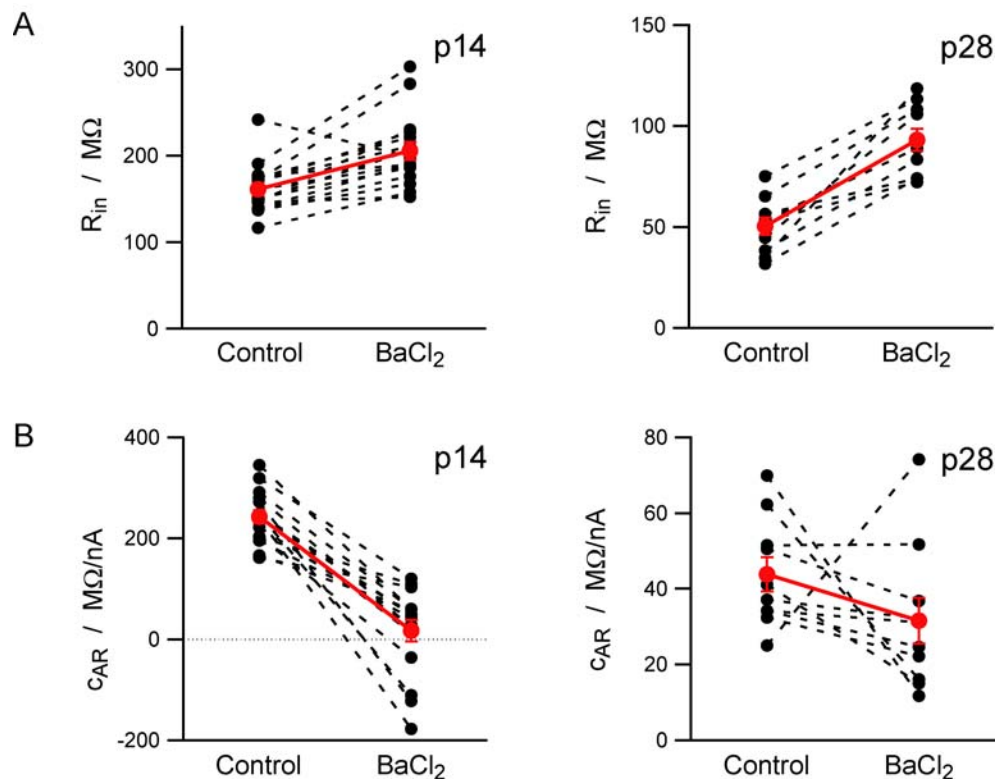


Fig. 2.23 Changes in sub-threshold behavior following application of $50 \mu\text{M}$ BaCl_2 . A, changes in R_{in} . B, changes in c_{AR} . Averaged data are displayed in red.

Spermine does not effect anomalous rectification

Connecting a cell's interior to a large reservoir of solution with a different ion and molecule composition – e.g. a patch pipette - leads to so-called wash-out effects: Fast diffusing molecules are washed out of the cell into the patch pipette where they are not present at the beginning. One type of these molecules are small polyamides that might be responsible for the voltage-dependent block of KIR channels (Bichet et al, 2003). Thus, in a series of control experiments in cells of two weeks old animals (p14) the polyamide spermine was added to the intracellular solution at a concentration of 100 μM (Ficker et al., 1994).

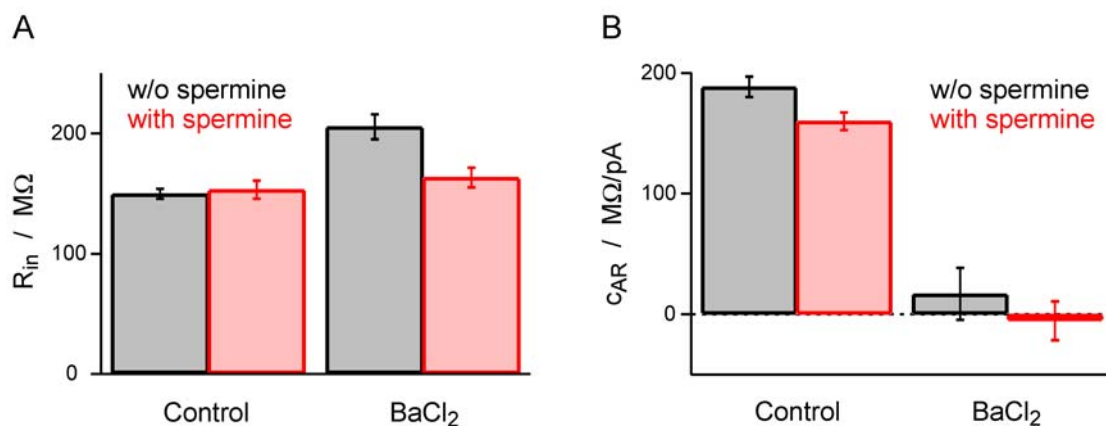


Fig. 2.24 Effect of 100 μM spermine (intracellular) on R_{in} (left) and c_{AR} (right) in two weeks old animals. Red, with spermine; black comparison with other experiments without spermine.

Application of 100 μM spermine did not lead to a significant change in anomalous rectification (Fig. 2.24B): $189 \pm 8 \text{ M}\Omega/\text{nA}$ without spermine ($n = 57(16)$) versus $160 \pm 7 \text{ M}\Omega/\text{nA}$ ($p > 0.05$, $n = 8(2)$, unpaired t-test) with spermine; also, additional extracellular application of 50 μM BaCl_2 reduced c_{AR} completely down to $-5 \pm 16 \text{ M}\Omega/\text{nA}$ ($p < 0.001$, $n = 5(2)$). Different from control experiments, though, application of BaCl_2 did not lead to a significant increase in R_{in} , whereas in all other experiments where BaCl_2 was applied an increase was observed (Fig. 2.24A).

2.3 Discussion

In this study we measured the biophysical properties of L2/3 pyramidal neurons during the first 6 weeks of postnatal development. The most important finding was a non-linear V-I relationship at all ages, which is well described by a second-order polynomial fit. Both coefficients of this fit, i.e. the linear input resistance R_{in} and the non-linear anomalous rectification (AR) coefficient c_{AR} , decrease with age. In pharmacological experiments we could show that AR is mainly attributable to inward-rectifier K^+ channels (KIR), while the contribution of the hyperpolarization-activated current I_h is small at best.

In the following paragraphs we will (1) discuss these experimental findings in the light of previous studies on the development of cortical neurons; (2) briefly review the ion channels that most likely contribute to the observed effects; and (3) present a re-interpretation of AR, which is based on the Hodgkin-Huxley formalism for describing ion channel kinetics.

2.3.1 Biophysical properties and development of L2/3 pyramidal neurons

The majority of previous studies on L2/3 pyramidal neurons have investigated cells from adult animals of more than 4 weeks of age. Thus, we will first compare our data from adult animals (steady-state) to these studies and then discuss the changes in biophysical properties that occurred during postnatal development.

Sub-threshold properties of adult L2/3 pyramidal cells

The input resistance R_{in} of L2/3 pyramidal neurons was found to be $47 \pm 16 \text{ M}\Omega$, which is consistent with the range for R_{in} (25 to 45 $\text{M}\Omega$) found in previous studies (Hwa & Avoli, 1991; Schroder & Luhmann, 1997; Traub et al., 2003; Waters et al., 2003; Larkum et al., 2007). Similarly, the resting membrane potential of $V_{rest} = 80 \pm 1$ is in the agreement with these previous studies (-72 to -81 mV), although it lies at the more hyperpolarized end of the range. Onset time constant is difficult to compare, because we found it to be voltage-dependent, while in other studies it is always presented with respect to current injections. Waters & Helmchen (2006) found 9 ms and Larkum et al. (2007) found 8 ms in rats of age around p28, which corresponds to our value for the voltage bin from 0 to -10 mV, while our value in the bin from -10 to -20 mV (which rather corresponds to the hyperpolarizations used for analyzing τ_{on} in the aforementioned studies) was 7

ms. This shift towards slightly faster time constants might have been introduced by the accounting for access resistance R_{acc} in our analysis.

The effect of AR in identified L2/3 pyramidal neurons was to our knowledge first described by Hwa & Avoli (1991). Unfortunately, the authors did not quantify, nor did they determine which specific channel types were responsible for this effect. Alonso & Klink investigated this effect in L2 cells of the rat entorhinal cortex and attributed it to TTX-sensitive persistent sodium currents (Alonso & Klink, 1993; Klink & Alonso, 1993). Recently, Waters & Helmchen (2006) provided a more quantitative analysis of AR in L2/3 pyramidal neurons *in vivo* using a second-order polynomial fit to steady-state V-I curves (equation 2.5). Their value as obtained under *in vivo* conditions ($c_{AR} = 18.7 \pm 3.7$ M Ω /nA) is pronouncedly lower than the value found in this study ($c_{AR} = 39 \pm 4$ M Ω /nA). In another recent *in vitro* study, Larkum et al. (2007) found a value of 37 ± 1 M Ω /nA, which is in good agreement with our value. As in the *in vivo* study of Waters & Helmchen R_{in} was also lower than in our study (29 M Ω versus 47 M Ω), we assume that additional modulatory effects might influence the biophysical properties of L2/3 pyramidal neurons *in vivo* even during DOWN-states. In none of the aforementioned studies the mechanism mediating AR was elucidated. Both Hwa & Avoli (1991) and Waters & Helmchen (2006) applied intracellularly the drug QX 314 to block Na⁺ channels (Connors & Prince, 1982). However, this drug is also known to affect other channels, in particular K⁺ channels (e.g. Nathan et al., 1990). Therefore, any conclusion derived from those experiments has to be taken with caution. It was noted, though, that Ih most likely is not responsible for AR, because of its near absence in L2/3 pyramidal neurons (Hwa & Avoli, 1991; Schroder & Luhmann, 1997; in this study, see lack of sag in Fig. 2.13). One likely consequence of AR might be that during summation of synaptic inputs, a loss of membrane resistivity due to increase in synaptic conductance is compensated for. Thus, PSPs which arrive during a train of EPSPs experience the same weighting at the soma. This aspect will be explored further in chapter 3.2.4.

Supra-threshold properties of adult L2/3 pyramidal cells

Action potential waveform and firing properties in L2/3 cells were very consistent with previous studies. As was noted before (Schroder & Luhmann, 1997), L2/3 pyramidal neurons were of the regular spiking (RS) type, showing almost no firing frequency adaptation during long constant current injections except during the first three APs. However, rhythmic bursting in these cells as reported by

Traub et al. (2003) was not observed in our experiments. Reasons for this discrepancy might be severalfold, including the use of preparatory depolarizing current injection in their study, differences in brain area and anesthesia, as well as their using sharp electrodes (additional leak in comparison to patch pipettes). AP halfwidth and amplitude V_{amp} were calculated to be around the same value as was found by Larkum et al. (2007).

Comparison with L5 pyramidal neurons

Some of the differences to the more thoroughly examined L5 pyramidal neurons are as follows: (1) L2/3 pyramids are much smaller with respect to dendritic extension. Following Zador et al. (1995), this makes L2/3 pyramids considerably more compact electrically. In particular the apical tuft, which in L5 pyramidal cells is electrically fairly uncoupled from the soma and the basal dendrites, might be much closer electrotonically in L2/3 pyramids, allowing single distal EPSPs to have a greater impact on somatic integration. (2) Ih is much more prominent in L5 pyramidal neurons, leading to sag values of 20-30% upon hyperpolarization in comparison to a maximum of 10% in L2/3 pyramids. We cannot exclude, however, that dendritic Ih density increases with distance from soma, as was shown for L5 pyramidal cells (Kole et al., 2006), which would have strong implications for dendritic integration (see below). (3) Prominent AR has not been reported in L5 pyramidal cells in rats. The somatic V-I relationships of L5 pyramidal neurons is nearly linear at all ages (Zhu, 2000), likely due to the balancing effect of Ih and KIR as reported by Day et al. (2006). However, presence of persistent Na⁺-channels in L5 pyramidal cells has been reported to mediate AR in cat sensori-motor cortex (Stafstrom et al., 1982; Stafstrom et al., 1985), implying that the behavior of these cells might differ from one species to another. (4) All cells encountered in L2/3 were of the regular spiking (RS) type, while in L5 a sub-population exhibits intrinsic bursting (IB) properties (Connors et al., 1982; McCormick et al., 1985; Changac-Amitai et al., 1990). In addition, even with strong depolarizing current injections, it was nearly impossible to elicit three APs with a mean frequency of more than 80 Hz. This suggests that under *in vivo* conditions, even during UP-states, L2/3 pyramidal neurons rarely fire more than 2 APs at high frequency, resulting in sparse firing in these layers (Brecht et al., 2003; Kerr et al., 2005; Waters & Helmchen, 2006; de Kock et al., 2007). This is inconsistent with the finding that regenerative events in the apical dendrite can be evoked at critical frequencies above 100 Hz (Larkum et al., 2007). Furthermore, Waters et al. (2003) reported strong Ca²⁺-influx upon trains of 2 to 5 APs at 150 Hz *in vivo*, while this influx was greatly reduced at 50 Hz with the

same number of APs. Indeed, 2 APs at 150 Hz elicited the same Ca^{2+} -influx as 4-5 APs at 50 Hz. We conclude that these supralinear summation effects and Ca^{2+} -influx might occur only very rarely and only upon extremely strong synaptic inputs.

In this study, we examined the postnatal development of the morphological and biophysical properties of L2/3 pyramidal cells between p8 and p45. All changes found indicate that these neurons become less receptive electrophysiologically to single PSPs as they mature. This will be discussed in detail in the following paragraphs.

Morphological development

Most changes in morphology take place within the first two postnatal weeks (Figs. 2.5-2.8). Primarily, dendritic branches grow out, shifting distributions of nodes and endings towards longer distances. However, on average no new dendritic compartments are added during development. Rather, between p8 and p14, elimination of small apical branches seems to take place. As was pointed out, though, various error sources might bias the number of dendritic branches towards higher values. Also, in a study on the development of L5 pyramidal cells (Zhang, 2004), no decrease in complexity was obvious, although morphological parameters were not quantified. Schroder & Luhmann (1997) pointed out in their study of adult cells, that the complexity of the basal tree is higher than that of the apical tree. We could not confirm this notion, as at all ages number of nodes and endings did not differ significantly between these two sub-trees.

Most surprisingly, no clear difference between L2 and L3 pyramidal cells was found based on morphological analysis. This is in contradiction to the empirical observation (also in this study), that L2 pyramidal cells extend more laterally with their apical tuft than L3 pyramidal cells (Fig. 2.4) and to findings that L2 and L3 pyramidal cells in somato-sensory areas receive different inputs from deeper brain areas (Shepherd & Svoboda, 2005; Bureau et al., 2006). However, for a detailed analysis, not enough morphologies were retrieved, and we most probably did not cover the whole spectrum of L2/3, with most cells being positioned around the middle of these two layers.

Development of L2/3 pyramidal neuron electrophysiology

Changes in R_{in} and V_{rest} show a similar time course as the changes found in other types of cortical neurons: R_{in} strongly decreases and V_{thresh} is shifted to

2 Experiments

more hyperpolarized potentials. Both changes implicate that the density of K^+ leak channels increases during development, increasing membrane conductance and shifting V_{rest} towards the K^+ reversal potential (eq. 1.7). These modifications have also been observed in L5 pyramidal neurons of several cortical regions (McCormick & Prince, 1987; Zhu, 2000; Zhang, 2004) and in Cajal-Retzius cells in L1 (Zhou & Hablitz, 1996). One possible explanation is that cortical neurons at early developmental states try to use all incoming synaptic activity for building and consolidating synaptic contacts to other cells in an activity-dependent way with maximized gain (here to be understood as number of EPSPs necessary to elicit an AP) with high input impedance and a short way to go from V_{rest} to V_{thresh} . In contrary, at later developmental stages, when the cortical network reaches a steady-state of synaptic contacts, single PSPs become less important and homeostatic effects take over, reducing the gain to a level where cortical computation can take place at minimized metabolic costs and without the system to explode in terms of activity.

Interestingly, the ability of L2/3 pyramidal neurons to elicit APs did not change during the ages, implying that all ionic conductances necessary are already inserted at a young age. This can be demonstrated in the following way: In order to exclude R_{in} and c_{AR} as sources of variability, AP frequencies were evaluated versus an extrapolated steady state voltage, $\Delta V_{extrapolated}$, using equation 2.5 with R_{in} and c_{AR} of the respective cell. This is illustrated in Fig. 2.25. Once the combined effect of different R_{in} and c_{AR} is excluded, the steady state AP frequency shows a similar behavior at all ages. We conclude that the ion channels responsible for eliciting APs are built into the membrane at an early age already, and are adjusted during development only to sharpen AP waveform.

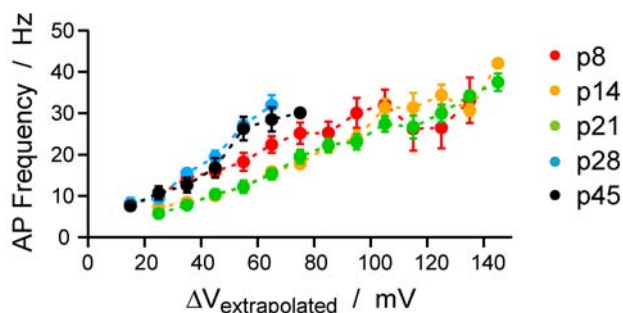


Fig. 2.25 AP frequencies versus extrapolated voltage. Voltages are binned in 10 mV wide intervals. Ages are color coded.

Nevertheless, conductance densities presumably do change during postnatal development, as AP waveform changes towards larger V_{amp} and smaller halfwidth. In addition, it was observed that young cells exhaust soon during longer lasting AP trains, resulting in sub-threshold voltage oscillations as not enough fast Na^+ channels can be recruited for additional APs.

2.3.2 KIR mediates anomalous rectification

The pharmacological experiments in this study demonstrated that the inwardly rectifying K^+ (KIR) channel is responsible for anomalous rectification in L2/3 pyramidal cells. Nevertheless, we cannot exclude a small contribution from other channels, mainly hyperpolarization-activated Ih channels, since after blocking KIR by low concentrations (50 μM) of Ba^{2+} the transient onset of voltage deflections was not reduced to a simple exponential curve (Fig. 2.22). Rather, an exponential transient seemed to be superimposed by the typical sag of Ih activation. These results will be discussed in the following sections.

KIR channels in L2/3 pyramidal neurons

In mammals, 15 gene products related to the KIR family have been classified into seven families named KIR1 to KIR7. Structural analysis of the crystal structure of a bacterial homolog shows two trans-membrane regions flanking an extracellular pore region (Kuo et al., 2003). The KIR channels mediating the strongest inward rectification comprise the KIR2 family (KIR2.1-KIR2.4). Recent studies (Pruess et al., 2005; Day et al., 2005) employing immuno-histological methods demonstrated that all channel types of the KIR2 family are present in neocortex, with KIR2.3 showing the highest expression in L2/3 and L5 pyramidal cell somata and neuropil. To complicate matters, KIR channels build hetero-tetramers (Yang et al., 1995), which virtually renders impossible the exact characterization of the KIR channel responsible for AR.

It is assumed that the inward rectifying properties of KIR channels are voltage-dependent and blocked by intracellular Mg^{2+} (Vandenberg, 1987; Matsuda et al., 1987) and polyamines (Lopatin et al., 1994; Ficker et al., 1994). Indeed, the amount of rectification mediated by these channels is defined by their characteristic interaction with these intracellular blockers. In our experiments, we were concerned about washout of these substances through the patch pipette, but addition of 100 μM spermine, a polyamine which was shown to effect KIR

channels (Ficker et al., 1994), did not alter AR (Fig. 2.24), showing the validity of our approach.

Contribution of Ih to anomalous rectification in L2/3 pyramidal neurons

As sag is present in L2/3 pyramids (if only to a small amount), we cannot completely neglect the effect of Ih-activation on sub-threshold behavior. In addition, it was shown in cortical L5 pyramidal neurons that Ih conductance density in the apical dendrite exponentially increases with distance from soma (Kole et al., 2006), a distribution which might also be present in L2/3 pyramidal neurons. Thus, while almost not present at the soma and in proximal regions, this channel might still shape synaptic integration in more distal regions of the dendritic tree.

Functional implications of anomalous rectification

The effect of KIR on the sub-threshold response of L2/3 pyramidal neurons is two-fold: (1) R_{in} and (2) τ_{on} both increase upon depolarization. The effects on dendritic integration of synaptic input might be as follows:

Activation of synapses is coupled to a loss of electric membrane resistance, thereby making polarization by activation of further synapses more difficult. This is a problem of all passive neurons, and is true in particular during episodes of high synaptic activity, be it spontaneous or stimulus-evoked. The increase of R_{in} upon depolarization by KIR channels might be a mechanism to overcome this problem. EPSPs arriving during UP-states will be rescaled by the increased input resistance, leading to a higher depolarization than in a passive neuron and thereby raising the cell's membrane potential across V_{thresh} more easily. Indeed, as was shown by Waters & Helmchen (2006), R_{in} is higher during UP-states (and not only unchanged), which implies that EPSPs arriving during these episodes are even bigger than those arriving during DOWN-states. Thus, the cell still remains receptive to incoming synaptic activity even during UP-states. Furthermore, as activation of synapses is costly with respect to the cell's metabolism, AR might also represent an "energy save" function.

The time constant $\tau_{on} = R \cdot C$ increases as R increases (and C stays constant). We observed an increase of τ_{on} upon depolarization of the cell's membrane, as it occurs during UP-states in vivo. This might lead to a state-dependent temporal filtering of synaptic input by L2/3 pyramidal neurons: During DOWN-states, when τ_{on} is small, the cell allows all EPSPs to contribute to the

cell's depolarization. During UP-states, however, fast EPSP-components are filtered out. Thereby the impact of proximal EPSPs on the cell response is reduced, while distal EPSPs (e.g. from the apical tuft), which already have been low-pass filtered by their longer traveling through dendritic cable, will stay constant. This also implies differential scaling by R_{in} -increase of EPSPs during UP-states.

Finally, KIR channels were shown to counterbalance the depolarizing effects of Ih on membrane potential, thereby stabilizing V_{rest} (Day et al., 2006). Clearly, since Ih is almost absent in L2/3 pyramidal neurons, this effect does not play a major role in these cells.

2.3.3 Hodgkin-Huxley-fit to I-V curves

From the pharmacology experiments we conclude, that anomalous rectification in L2/3 pyramidal neurons is mainly mediated by inwardly rectifying K-channels (KIR). This allows a reinterpretation of the observed steady-state V-I curves. Instead of fitting V-I relationships phenomenologically with a simple, second-order Taylor expansion, the inverse function (the I-V curve) can be fitted using a conductance-based Hodgkin-Huxley (HH) style model. The cells are treated here as being point-neurons. This gross simplification is justified since we do not consider transient responses but steady-states. The results of this approach lead to an estimate of the total conductance of the respective channel type for the electrically visible part of the cell, but provide no information on actual conductance densities which are essential for compartmental models of L2/3 pyramidal cells.

Fitting I-V curves by steady-state channel open probabilities

Since the contribution of Ih to c_{AR} is not very large, it was omitted and the I-V curve was fitted by a combination of nonspecific, non-voltage-dependent leak conductance G_{leak} , and KIR conductance G_{KIR} :

$$I(V) = G_{leak} (V - E_{leak}) + \frac{G_{KIR}}{1 + e^{\frac{V - V_{1/2}}{V_{slope}}}} (V - E_K) \quad (2.7)$$

Here, the voltage-dependence of the KIR conductance follows a sigmoidal relationship with half-activation at $V_{1/2} = -90$ mV and slope at half-activation of

2 Experiments

12.1 mV as shown in Day et al. (2005). According to equation 2.7, the fit uses four free parameters, the maximal leak and KIR conductances G_{leak} and G_{KIR} and the respective reversal potentials E_{leak} and E_K . The potassium reversal potential was restrained to be more negative than E_{leak} in all fits. Fig. 2.26 shows an example of the procedure: On the left panel (A), one can see that the fit by a polynomial (eq. 2.5) is not satisfactory. Inverting the data and fitting the data points by eq. 2.7 leads to a much better approximation of the data (red curve).

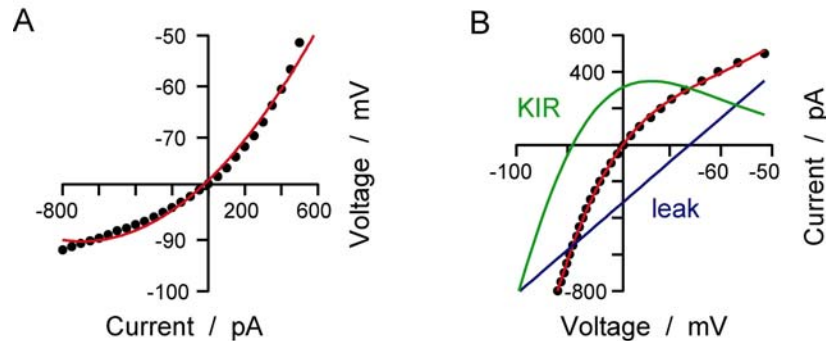


Fig. 2.26 Fitting data with Hodgkin-Huxley (HH) steady state kinetics. **A**, V-I curve fitted by a second order polynomial (eq. 2.5). **B**, I-V curve fitted with two-conductance HH-model (eq. 2.7). Contributions of leak (blue) and KIR (green) currents are displayed separately.

Note that at resting potential, the two currents taken into account (leak, blue, and KIR, green) exactly balance each other.

Leak and KIR conductances increase as L2/3 pyramidal neurons mature

Surprisingly, both leak and KIR conductances derived from such fits in animals of different age increased as the cells mature (Fig. 2.27A). G_{leak} increased from 5 μ S at p8 to 15 ± 4 μ S at p45 and G_{KIR} from 3 μ S to 51 ± 12 μ S. At the same time, the leak reversal potential shifted to slightly more negative values, while there were no significant changes in potassium reversal potential (Fig. 2.27B). This finding is surprising because C_{AR} as a measure for anomalous rectification decreases during development while the total conductance of the channel responsible for this effect increases. This problem does not occur with input resistance, since a higher leak conductance should lead to a lower linear (ohmic)

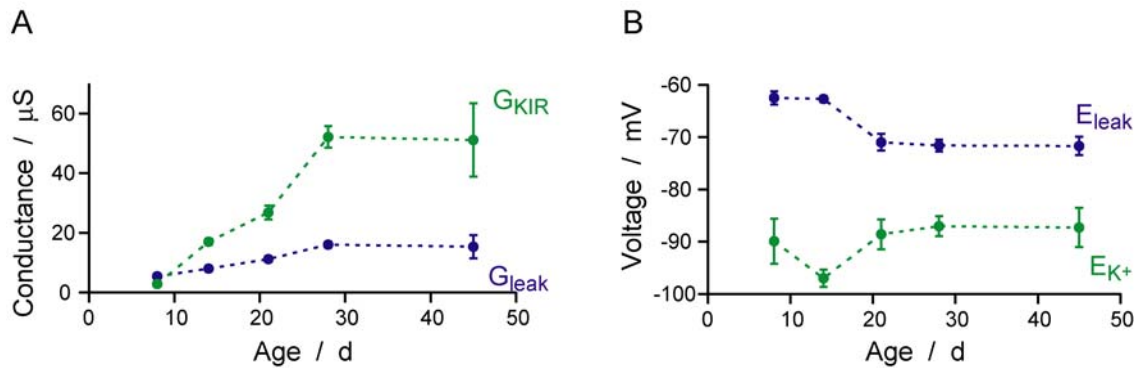


Fig. 2.27 Results of fitting HH steady-state kinetics to I-V curves. **A**, total conductances in dependence on age. **B**, age-dependence of respective reversal potentials.

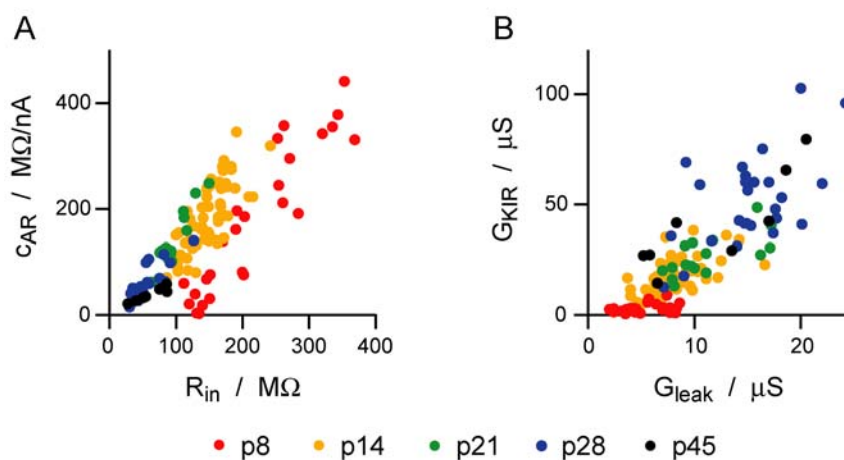


Fig. 2.28 Dependencies of passive parameters. **A**, c_{AR} versus R_{in} . **B**, KIR versus leak conductance. In both cases, ages are color-coded (bottom of graph).

input resistance. Another puzzling observation is that c_{AR} seems to be linearly dependent on input resistance at all ages (Fig. 2.28A). At the same time, G_{KIR} is linearly dependent on G_{leak} at all ages except p8 (Fig. 2.28B), which can be explained by changes in surface area given a purely age-dependent specific conductance density for both channels. One would expect, though, that a higher KIR conductance leads to a higher anomalous rectification. The contrary seems to be true, since in Fig. 2.28B the x-axis is practically the inverse of the x-axis in Fig. 2.28A.

In order to understand this contradiction we tried to predict R_{in} and c_{AR} as a function of G_{leak} and G_{KIR} . For this purpose we inverted equation 2.7 numerically using Mathematica (WolframResearch, IL, USA). The result was then expanded into a Taylor series. The first and second coefficients should be input resistance and anomalous rectification, respectively.

2 Experiments

The functions $R_{in}(G_{leak}, G_{KIR})$ and $c_{AR}(G_{leak}, G_{KIR})$ (pink surfaces) are shown in Fig. 2.29. One can see that the measured data follow the derived functional surfaces well, although measured c_{AR} seems to be systematically above the surface. This effect might be attributable to a small contribution of Ih or of other voltage-dependent channels.

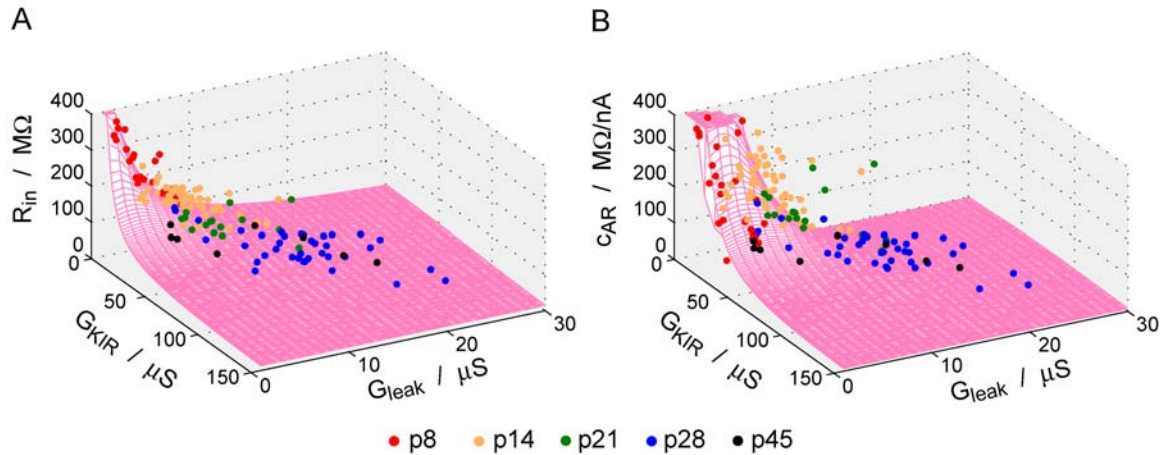


Fig. 2.29 Predicted and experimental dependencies of R_{in} and c_{AR} on G_{leak} and G_{KIR} . **A**, R_{in} as a function of G_{leak} and G_{KIR} . Pink surface, prediction; dots denote measurements. **B**, c_{AR} as a function of G_{leak} and G_{KIR} . Pink surface, prediction; dots denote measurements. Ages are color-coded (see bottom of graph).

BaCl₂ shows clear effect on KIR conductance

In contrast to younger animals, application of 50 μM BaCl₂ did not lead to a significant reduction of c_{AR} in p28 cells (Fig. 2.23 B), although G_{KIR} was found to increase with age. This is probably due to the strong reduction in R_{in} during maturation. In order to examine whether there really is no clear effect on the channel responsible for non-linearization of V-I curves in p28 cells, we analyzed the pharmacological experiments utilizing equation 2.7.

The results are shown in Fig. 2.30. G_{KIR} was reduced from 14 ± 1 μS to 1 ± 0 μS in p14 cells ($p < 0.01$, $n = 16(5)$) and from 63 ± 7 μS to 1 ± 0 μS in p28 cells ($p < 0.01$, $n = 10(3)$). At the same time, G_{leak} was reduced from 8 ± 1 μS to 5 ± 0 μS in p14 cells ($p < 0.05$, $n = 16(5)$) and from 16 ± 1 μS to 10 ± 1 μS in p28 cells, explaining the increase in R_{in} by application of BaCl₂.

From the pharmacological experiments and the additional analysis using the HH-style description of conductances we conclude, that AR is predominantly mediated by KIR channels which are blocked by low concentrations of BaCl₂.

Additional contribution to AR might originate from the hyperpolarization activated current, I_h , but experiments with a specific blocker were ambiguous. Persistent Na^+ -channels do not seem to contribute to AR. These findings are consistent for the two ages examined.

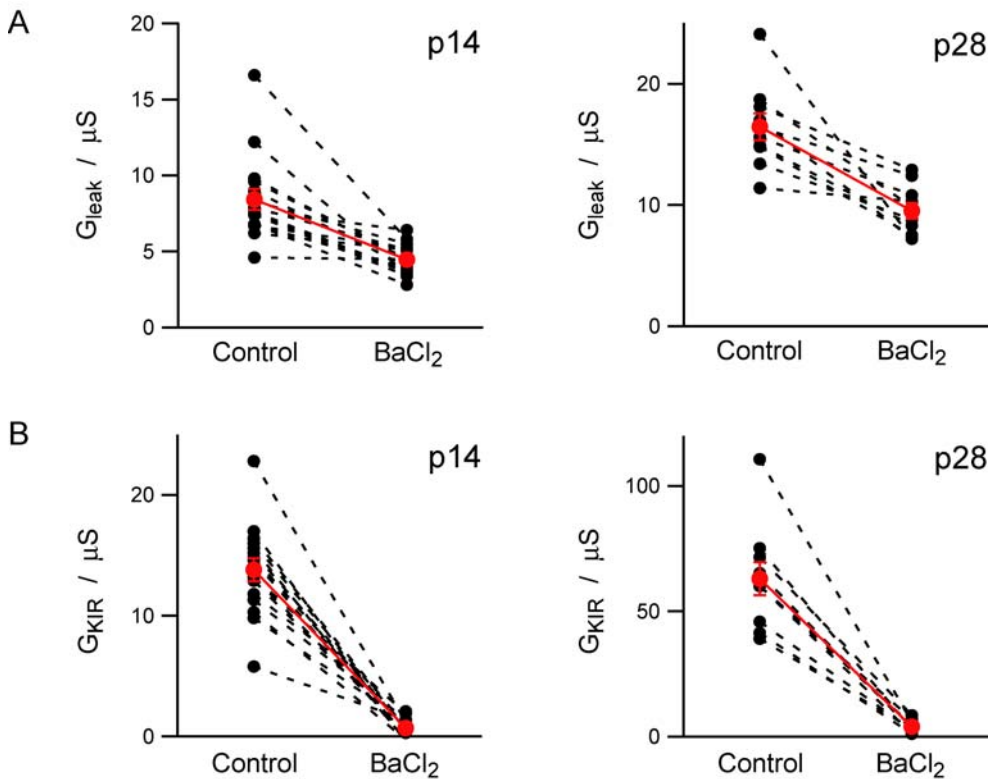


Fig. 1 Effect of $50 \mu\text{M}$ BaCl_2 on G_{leak} (A) and G_{KIR} (B). Averages are shown in red.

In order to further analyze the data, in particular the transient onset of the voltage traces, in a second step we turned to compartmental modeling. This gave us the means to finally assess the contribution of I_h as well as to build an age-dependent model of L2/3 pyramidal neurons which can be easily included in simulations of developing cortical networks.

3 Modeling

In the experimental part of this thesis we examined the basic biophysical properties of L2/3 pyramidal cells, their development during the first six postnatal weeks, and the mechanisms underlying the sub-threshold rectification. In order to further explore the role that these mechanisms may play in synaptic integration, we employed numerical simulations of reduced as well as full-morphology models. In this chapter the methods and results of numerical simulations are presented and their implications for L2/3 pyramidal neurons are discussed.

3.1 Modeling Methods

We first describe the modeling methods and theoretical formulations used in this study in detail. In particular, we introduce the search algorithm that was used for finding optimal parameter sets for a valid compartmental model of L2/3 pyramidal neurons in order to reproduce the experimental data from chapter 2.2.

3.1.1 Voltage-dependent ion channels

Although Hodgkin and Huxley already hypothesized that the steady-state behavior of gating particles, $x_{\infty}(V)$, can be described by a Boltzmann distribution, they used various arbitrary functions to fit the data (Hodgkin & Huxley, 1952d; see chapter 1.3.2). This led to an uncontrollable number of variables per gating particle. For gating particles that depend only on voltage this dependence can be described in a biophysically more meaningful way by considering parameters of a single-barrier kinetic model for each particle (Borg-Graham, 1999). This formulation reduces the number of kinetic parameters to five per gating particle. Additionally, the parameters are more directly linked to the kinetic behavior of the channel. In the following we describe this formula in more detail.

The following considerations transform the open and close rates $\alpha(V)$ and $\beta(V)$ of the original Hodgkin & Huxley (HH) formalism (equation 1.9) to new rates $\alpha'(V)$ and $\beta'(V)$: for a given particle x , z (dimensionless) is the effective valence of this particle's voltage sensor. Here, a negative value means that the particle tends to open with depolarization, i.e. it is an activation particle, whereas a positive value of z denotes an inactivation particle that closes with depolarization. Through partial electric shielding by charges of the opposite sign, z does not have to be an integer. γ (dimensionless, $0 \leq \gamma \leq 1$) is the asymmetry of the gating

particle's voltage sensor position within the membrane. A (in units of ms^{-1}) is the leading coefficient of both $\alpha'(V)$ and $\beta'(V)$, which can be described by Eyring rate theory, an explicit version of which might include an additional temperature dependence (Johnston & Wu, 1997). For all channels presented, A is taken to be constant. $V_{1/2}$ is the voltage for which $\alpha'(V)$ and $\beta'(V)$ are equal. With these definitions the new rates $\alpha'(V)$ and $\beta'(V)$ are given by:

$$\begin{aligned}\alpha'(V) &= A e^{\frac{-z\gamma F(V-V_{1/2})}{RT}} \\ \beta'(V) &= A e^{\frac{z(1-\gamma)F(V-V_{1/2})}{RT}}\end{aligned}\quad (3.1)$$

In accordance to equation 1.9, the steady-state activation $x_\infty(V)$ can be written as

$$x_\infty(V) = \frac{\alpha'(V)}{\alpha'(V) + \beta'(V)} \quad (3.2)$$

An additional parameter, τ_0 , is crucial for fitting the expression to the original HH mechanism. τ_0 can be interpreted as a rate limiting step in the conformational change following a voltage step. Intuitively, τ_0 is incorporated into equation 3.1:

$$\tau_x = \frac{1}{\alpha'(V) + \beta'(V)} + \tau_0 \quad (3.3)$$

Alternatively, one can write down the rate constants from equation 1.9 as functions of $\alpha'(V)$ and $\beta'(V)$ and τ_0 :

$$\begin{aligned}\alpha(V) &= \frac{\alpha'(V)}{\tau_0(\alpha'(V) + \beta'(V)) + 1} \\ \beta(V) &= \frac{\beta'(V)}{\tau_0(\alpha'(V) + \beta'(V)) + 1}\end{aligned}\quad (3.4)$$

The effects of A , z , γ , $V_{1/2}$ and τ_0 on $x_\infty(V)$ and $\tau_x(V)$ are illustrated in Fig. 3.1: $V_{1/2}$ sets the voltage of the midpoint and z the steepness of the $x_\infty(V)$ sigmoid. The symmetry parameter γ sets the skew of $\tau_x(V)$: $\gamma = 0.5$ means a voltage sensor exactly in the middle of the lipid bilayer and thus a perfectly symmetric bell-shaped curve for $\tau_x(V)$, which otherwise is bent to one or the other side as γ approaches 0 or 1, respectively. Finally, A sets the maximum of $\tau_x(V)$ and τ_0 its offset.

Note that, while z and $V_{1/2}$ do have effects on $\tau_x(V)$ by setting width and the maximum's position, respectively, the other parameters, A , γ and τ_0 , do not

3 Modeling

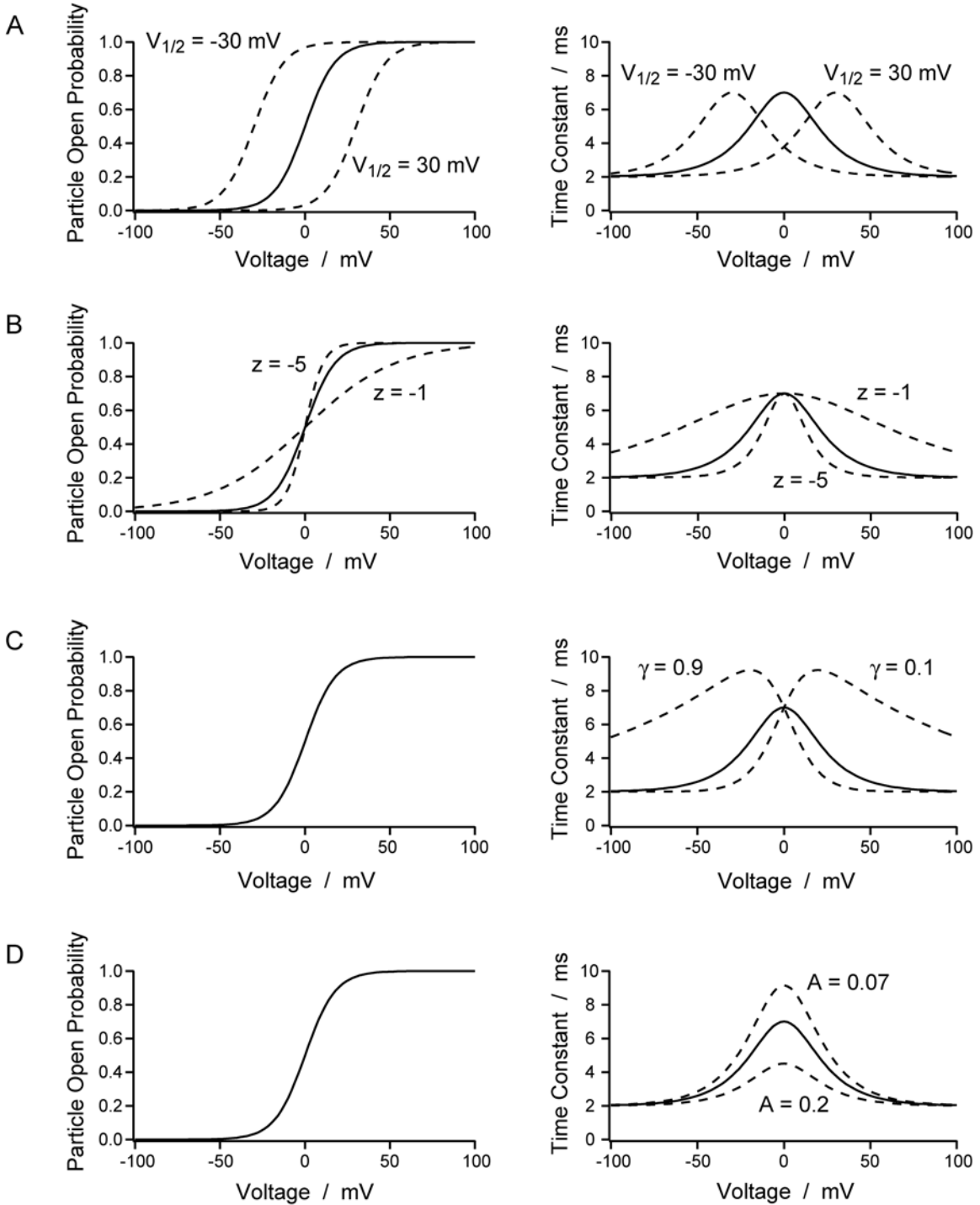


Fig. 3.1 Effect of kinetic parameters on steady-state open probability x_∞ (left) and time constant τ_x (right) of a voltage-sensitive ion channel. Solid lines in all graphs were generated using following parameters: $V_{1/2} = 0$ mV, $z = -3$, $\gamma = 0.5$, $A = 0.1$ ms⁻¹ and $\tau_0 = 2$ ms. **A**, changing $V_{1/2}$ shifts x_∞ and τ_x but leaves their shapes unchanged. **B**, decreasing z “flattens” out the curves while increasing z steepens the curves. **C**, changing γ skews τ_x but leaves x_∞ unaltered. Note that also the maximum time constant increases as γ is changed. **D**, changing A increases or decreases the maximum τ_x but leaves x_∞ unchanged.

have an effect on $x_\infty(V)$. This allows, within certain limits, independent tuning of $x_\infty(V)$ and $\tau_x(V)$.

3.1.2 Compartmental modeling

This study is part of an effort to build a realistic model of L2/3 pyramidal neurons. To this end we use numerical simulations in detailed reconstructed morphologies, in which a compartmental model is used to represent the complex dendritic tree.

Discretization of the cable equation

Analytical solutions of the cable equation become rather complicated if the diameter of the cable changes with distance or if there are branch points connecting multiple cables. In the presence of voltage-dependent ion channels, however, solving equation 1.1 analytically becomes practically impossible. In these cases it is convenient to solve it numerically. By spatial discretization of the cable equation one obtains a family of ordinary differential equations of the form

$$c_j \frac{\partial V_j}{\partial t} + I_{ion,j} = \sum_k \frac{V_k - V_j}{r_{jk}} \quad (3.5)$$

These equations simply represent Kirchhoff's law of current conservation: The membrane currents for compartment j must balance all currents from axially adjacent (connected) compartments k . Compartmental models of neurons were first used by Rall (1964).

The NEURON Environment

NEURON is a free software package written by Michael Hines (Hines & Carnevale, 1997) that has become a standard tool for simulating compartmental models of neurons. The program uses an efficient numbering scheme for the n compartments of the neuron's branched cable structures such as dendritic and axonal trees which allows for inverting the connectivity matrix in $O(n)$ steps (Hines, 1984). Thus, implicit methods for solving the discretized cable equation can be applied in an efficient manner. The default method is the backward Euler method, which is stable for large steps and robust in practice. Additionally, the HOC (Higher Order Calculator) command set allows programming of routines

similar to the language C with numerous intrinsic commands e.g. for manipulation of matrices and vectors.

All mechanisms such as voltage-dependent ion channels and calcium diffusion were programmed in NMODL (Hines & Carnevale, 2000), an extension to NEURON. In addition to its use for implementation of a variety of ionic conductances, NMODL can also be used as a freeware C compiler.

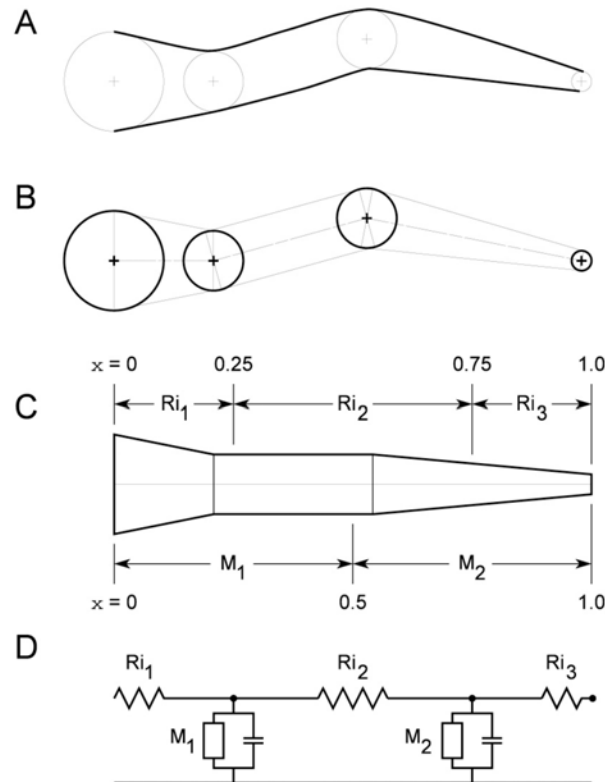


Fig. 3.2 Spatial discretization of the cable equation. **A**, schematic representation of an unbranched section of a dendrite. Morphological reconstruction (see experimental methods) provides lists of local coordinates (crosses) and diameters (circles). **B**, each pair of adjacent diameter measurements forms the parallel faces of a truncated cone. **C**, since bends are ignored when forming the one-dimensional cable equation, the reconstructed protrusion is straightened out. **D**, electrical equivalent circuit with two compartments. R_i refers to the axial resistance and M to the membrane areas of the compartments. x is a relative spatial coordinate with $0 \leq x \leq 1$. (Figure taken from Hines & Carnevale, 1997)

Besides solving the temporal evolution of the cable equation with constant timesteps NEURON also employs a multi-order variable timestep integration method called CVODE (Cohen & Hindmarsh, 1996; Hindmarsh et al., 2005) at hoc level, which was used for all parameter search experiments in this study.

3.1.3 Automated parameter search

In order to tune a neuronal model such that it reproduces experimental data one has to adjust a number of parameters characterizing ionic conductances and other biophysical properties such as capacitance and intracellular diffusion. In other words, a vector \mathbf{x} in an n -dimensional parameter space has to be found such that a scalar cost function $E(\mathbf{x})$ is minimized. For a valid model the global minimum is to be found.

Depending on the complexity of the neuronal model at hand, the number of parameters quickly skyrockets, as every voltage-dependent channel not only adds its conductance and reversal potential to the number of parameters, but also its kinetic parameters and spatial distribution. Considering this, it becomes clear that tuning the model by hand or simply sampling parameter space ("brute force approach"; for examples see Bhalla & Bower, 1993; Prinz et al., 2003) cannot be methods of choice (although it still is in most studies): If each one of n parameters is sampled k times, the total number of simulations N necessary for sampling the whole parameter space increases exponentially as $N = k^n$. This is known as "the curse of dimensionality" (Bellman, 1957).

Another problem arises from the fact that within the reachable parameter space "islands" exist with relatively low errors separated by regimes of high error values (e.g. Achard & De Schutter, 2006). This excludes gradient based search routines like the downward simplex method (see e. g. Press et al., 1992) because these will find the nearest or steepest local minimum and converge there without exploring parameter space any further.

In a recent study, Vanier and Bower (1999) examined the behaviour of different search algorithms when applied to a complex neuron model with several ionic conductances (leading to a total number of up to 23 parameters). When retrieving parameters in their tests two algorithms outperformed gradient based methods in respect to quality of the solution and computational time needed: a genetic algorithm and a simulated annealing algorithm (Kirkpatrick et al., 1983; Kirkpatrick, 1984). As the latter performed slightly better (and as it is inspired by physics), we chose to implement a simulated annealing-based search algorithm in the NEURON environment. In the following paragraphs the principle ideas underlying this search algorithm are described. The NEURON code for the simulated annealing algorithm as well as for the error functions used can be found in appendix 7.1 together with an example model file.

Simulated annealing – basic principles

The idea of the simulated annealing (SA) algorithm was first formulated by Nicholas Metropolis and colleagues at the Los Alamos laboratories and applied to the problem of condensing matter (Metropolis et al., 1953).

A point \mathbf{x} is moved in n -dimensional parameter space with an arbitrary random walk method. In contrast to gradient-based methods, where every move leading “downhill” and thus reducing the error function $E(\mathbf{x})$ is accepted, the SA algorithm will also accept movements "uphill" (i.e., $E(\mathbf{x})$ increases) with a certain probability. This probability p is given by a Boltzmann term

$$p \propto e^{-\frac{\Delta E}{kT}} \quad (3.6)$$

where $\Delta E = E_i - E_{i-1}$ is the difference in error function before and after movement of \mathbf{x} , and kT is the Boltzmann constant times temperature. Although the algorithm originally was inspired by thermodynamics and also applied in that field, the term kT has to be compared to the "energy" $E(\mathbf{x})$, which is given in units of error function (e. g. mV^2/ms^2). Note that, by convention, if $\Delta E \leq 0$, p is set to 1. Thus, movements downhill are always accepted.

At the start of the SA algorithm, T is chosen to be very high (see below), corresponding to the temperature of a hot fluid, as all movements are accepted even if the state \mathbf{x} moves into an energetically less favourable regime. As the temperature decreases according to a predefined annealing schedule (see below), the system moves to lower energy states, ideally settling in a global or at least near-optimal minimum as T approaches 0. In real physical systems this temperature corresponds to the point of crystallization. Vice versa, if only downhill movements are accepted or $T = 0$ from the very beginning, the material is quenched very rapidly and will develop into a glasslike structure representing a local minimum of $E(\mathbf{x})$.

A variant of the Metropolis algorithm was proposed by Glauber (1963), in which also downhill movements are also accepted with a probability $p \leq 1$:

$$p = \frac{e^{-\frac{\Delta E}{kT}}}{1 + e^{-\frac{\Delta E}{kT}}} \quad (3.7)$$

As the temperature approaches zero, the probability for accepting a downhill movement $p(\Delta E \leq 0)$ approaches 1 whereas $p(\Delta E \geq 0)$ approaches 0. For all parameter searches performed for this thesis the original Metropolis algorithm

was used as it performs better when moving close to thermal equilibrium (see below).

Movements in parameter space

One of the major problems in every SA algorithm is the movement of the test vector \mathbf{x} . Many algorithms have been proposed, the most attractive being that of Press and colleagues (first published by Press et al., 1991; Press et al., 1992). This algorithm combines the downward simplex algorithm (Nelder & Mead, 1965) with the Metropolis algorithm. Instead of moving a single point in parameter space a simplex, the simplest body consisting of $n+1$ linearly independent points in n -dimensional space is moved following certain rules as illustrated in Figure 3.3.

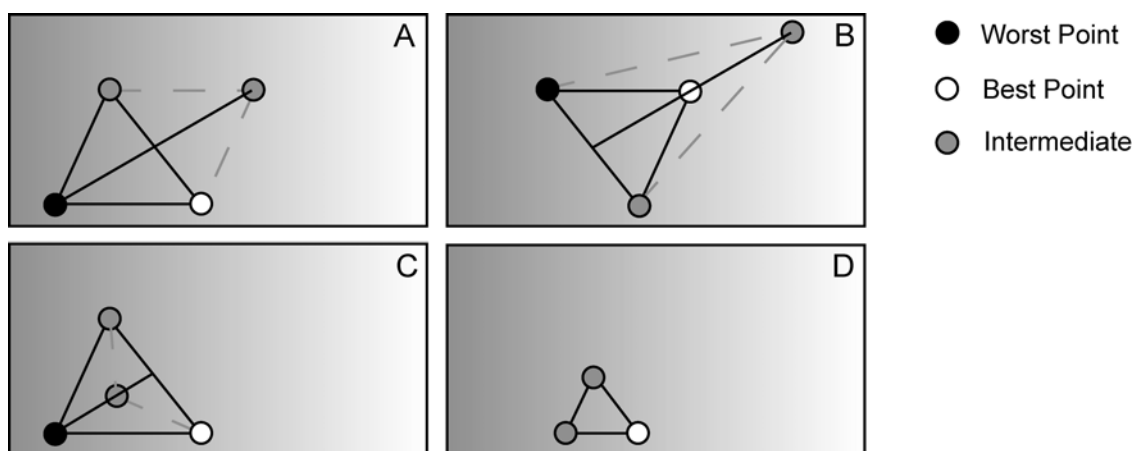


Fig. 3.3 Movement of the simplex in two-dimensional space. **A**, Basic movement. The worst vertex is mirrored through the centre of the hyperplane defined by the remaining vertices. **B**, Exploration. If the newly encountered point from **A** also is the new best, the simplex extends into the direction from **A** by a factor of two. **C**, One-directional contraction. If the newly encountered point from **A** is also the new worst, it is discarded. Instead, the old worst is moved along the direction from **A** by a factor of one-half. **D**, Complete Contraction. If the algorithm could not get rid of the worst point in **C**, it will contract completely around the best vertex.

In the algorithm used for this study, each of the $n+1$ vertices, \mathbf{x}_i , maps onto an error value $E_i(\mathbf{x}_i)$, which itself is one component of an $(n+1)$ -dimensional error vector \mathbf{E} . At the beginning of each movement cycle (see below), the decision is made which point will be moved by subtracting a temperature-dependent term from each E_i and comparing the new values E_i' :

$$E_i' = E_i - T \ln r \quad (3.8)$$

where T is the temperature and $0 \leq r \leq 1$ a random number. Note that this equation is equivalent to equation 3.6. Since the unit of T corresponds to the unit of the error function, k is omitted here. This procedure is the core of the function *amebsa()* (see appendix 7.1.1). After application of equation 3.8, three elements are identified: The best (lowest E_i'), the worst (highest E_i'), and the second worst. These are used for the whole movement cycle. Note that during the process E_i values are not changed.

Fig. 3.3 shows the possible movements of the simplex. Movements A, B and C are implemented in the function *amotsa()* and are described by

$$x_{try} = \bar{x}(1-a) - x_{old} \left(\frac{1-a}{n} - a \right) \quad (3.9)$$

with \bar{x} the centroid (as given by the average of all vertices) of the old simplex, n the dimension of parameter space and a the argument for *amotsa()*.

The first movement during a movement cycle is the mirroring of the worst point through the centre C_n of the hyperplane defined by the remaining n points (*amotsa(-1)*, Fig. 3.3A). If the newly encountered point is better than the previous best, the simplex will extend along that direction by a factor of 2 (*amotsa(2)*, Fig. 3.3B) and the movement cycle is terminated as successful. If the newly encountered point is better than the second worst, but worse than the best, then the point is accepted and the movement cycle is terminated as successful. In the third scenario, the new point is worse than the previously worst point. In this case, the new point is rejected (unsuccessful move), and *amotsa(0.5)* is called, moving the worst vertex towards the hyperplane (one-directional contraction; Fig. 3.3C). If the new point is better than the previously worst one, the movement cycle is terminated. Otherwise, complete multi-directional contraction around the best point takes place (Fig 3.3D), and the movement cycle is terminated.

Cooling schedule

As mentioned above, if a fluid is cooled down too quickly, it will end up as a glass and not a crystal. In analogy, fast reduction of the temperature T in the SA algorithm might lead to convergence around a local instead of the global minimum. On the other hand, if the algorithm converges too slowly much of the computational time is spent in regimes of the parameter space which are unlikely to contain the global minimum (or any minimum at all). Thus, it is crucial to find a

balance between cooling close to thermal equilibrium and total computational time spent on the given problem.

(Aarts and van Laarhoven, 1985) proposed a cooling schedule that uses the fluctuations of the error function encountered during one Metropolis cycle (in our program defined as $n \cdot (n+1)$ movement cycles). Here, the new temperature T_{j+1} is set according to

$$T_{j+1} = \frac{T_j}{1 + \frac{T_j \ln(1 + \delta)}{3\sigma}} \quad (3.10)$$

where T_j is the temperature during the last Metropolis cycle, σ the variance of all error function values encountered during that cycle and δ an adjustable parameter defining the closeness to equilibrium. As a rule of thumb, $\delta > 1$ leads to very fast cooling and convergence around a local minimum, while $0 < \delta < 1$ produces slow convergences with more extensive sampling of the reachable parameter space. In our experiments δ was set to 0.1, which is lower than values previously used ($\delta = 0.3$; Das et al., 1990).

For testing this method we employed a simple exponential cooling schedule (Kirkpatrick et al., 1983), whereby the temperature is decreased by a certain percentage (usually 3%) every given number of iterations.

Starting temperature

The starting temperature is an important parameter and has to be chosen according to the shape of the error landscape. It can be obtained by specifying the initial fraction of movements to be accepted. In our experience it is important, though, that the initial acceptance probability is close to one. To this end, T_{init} was chosen such that the acceptance probability

$$p = \frac{m_1 + m_2 e^{\frac{-\overline{\Delta E}}{T_{init}}}}{m_1 + m_2} \quad (3.11)$$

reached 95% (Das et al., 1990). Before starting the algorithm, one full Metropolis cycle was run with $m = m_1 + m_2$ error function evaluations. Here, m_1 represents the number of successful ($\Delta E < 0$), m_2 the number of unsuccessful moves ($\Delta E \geq 0$) and $\overline{\Delta E}$ the average increase in cost for the m_2 unsuccessful moves. The SA algorithm was run for one cycle at a temperature that was high enough for

acceptance of all simplex movements (for all practical reasons $T = 10^{12}$ was sufficiently high).

Termination criteria

Two criteria were used to determine convergence of the simplex: One criterion is inherent to the program as presented by Press et al. (1992) and describes the collapse of the centroid. Termination of parameter search occurred when the centroid collapsed below 10^{-3} .

The other criterion is based on an average gradient of the error function with respect to the number of function evaluations. In order to implement this while smoothing out fluctuations in the error function, groups of $5n$ (five times the number of parameters) values were averaged. The normalized gradient was computed from these averages:

$$\left\| \frac{1}{E_i^*} \frac{dE^*}{dN} \right\| = \left\| \frac{E_i^* - E_{i-1}^*}{E_i^*(N_i - N_{i-1})} \right\| < \varepsilon \quad (3.12)$$

with $0 < \varepsilon \ll 1$ (here usually chosen as 10^{-5}). E_i^* denotes the mean error values averaged over the respective N_i function evaluations during iteration i . Note that the N_i 's are not of constant size depending on the shape of the error function. It sometimes occurred, however, that the termination criterion equation 3.12 lead to premature exit of the algorithm. In these cases, equation 3.12 was not used and convergence was defined by the criterion originally proposed by Press et al. (1992).

Initialization of the simplex

The simplex was initiated by first defining a single vertex in parameter space. Then, the remaining n points were computed by moving a given maximal distance parallel to each coordinate axis in turn. Usually, the simplex was chosen such that it engulfed the "educated guess" regime in parameter space which was derived for example from previous models of other cells and measured channel kinetics.

Dealing with boundaries

In order to prevent the algorithm from getting lost in regimes of parameter space that are physiologically irrelevant or which result in unrealistic kinetics of a certain

channel, lower and upper boundaries were introduced. Every time a vertex crosses one (of a total of n) such boundary (boundaries), it is set randomly into a 1 % environment of the previously found best \mathbf{x}_{best} (Cardoso et al., 1996; Weaver & Wearne, 2006):

$$0.99x_{i,best} \leq x_{i,new} \leq 1.01x_{i,best} \quad (3.13)$$

This recentering procedure is repeated until a vertex is found that lies within the given boundaries. One has to note, though, that the simplex usually is heavily distorted by this procedure. In addition, in our experience, if recentering happens when \mathbf{x}_{best} itself is close to the border, convergence in a local minimum close to that border is likely

Error function

Crucial for successful tuning a neuron model is an error function that allows an objective distinction between "good" and "bad" parameter sets (and all intermediates). To this end, several approaches can be found in the literature, from simple ones like differences in inter-spike intervals (Vanier & Bower, 1999) to more complex ones such as differences in phase-plane trajectory densities (Le Masson & Maex, 2001; Achard & De Schutter, 2006) for fast spiking neurons.

In our study of sub-threshold behaviour of L2/3 pyramidal neurons a simple squared-error function was sufficient to describe the main features of sub-threshold voltage-traces. With this method the sequences of sub-threshold voltage traces evoked by current injection were fitted by minimizing the squared error between simulated (v_{sim}) and measured (v_{target}) trace:

$$E = \sum_{I_{inj}} (v_{sim} - v_{target})^2 \quad (3.14)$$

Here, the sum runs over all injected current values which elicit sub-threshold responses, whereby the entire series of current injections for determining V-I relationships were fitted simultaneously. Since the CVODE method (see chapter 3.1.2) leads to simulated voltage traces with time points that are not equidistant, for all error functions the simulated traces were re-sampled by linear interpolation to 10 kHz, the same frequency used for our experimental measurements. In order not to overrate certain aspects of the measured traces (like the temporal development following the onset of a current injection versus steady state) the time window over which the traces are compared has to be chosen carefully. Another option might be the introduction of an additional penalty function that

weighs the onset phase stronger than the steady state, e.g. multiplication by a decaying exponential function.

3.1.4 Simulating UP/DOWN-states

One important application of the subthreshold L2/3 pyramidal cell model is to reproduce spontaneous neuronal activity in the form of UP- and DOWN-states as typically seen in *in vivo* experiments, representing different levels of synaptic activity. In a recent publication, UP-states were reproduced for L2/3 pyramidal neurons in 4-weeks old rats using a simple phenomenological description of anomalous rectification (Waters & Helmchen, 2006; equation 2.5). Here, we aimed at a more realistic simulation of UP-states using a conductance-based model. The goal was to assess the impact of changes in KIR and leak conductances during postnatal development on these spontaneous depolarizations.

Double exponential synapses

A varying number of synapses were inserted in single- as well as in multi-compartment models of L2/3 pyramidal cells. Synapses were modelled as locally changing membrane conductance g_{syn} with a double exponential time course:

$$g_{syn}(t) = W k \left(e^{-\frac{t}{\tau_2}} - e^{-\frac{t}{\tau_1}} \right) \quad (3.15)$$

W is the synapse's weight factor; k is a factor normalizing the peak of the summed exponential functions to 1; τ_1 and τ_2 are the time constants for the rising and the decaying phase of the PSP, respectively, and were taken to be $\tau_1 = 0.2$ ms and $\tau_2 = 1.7$ ms for excitatory (Hausser & Roth, 1997) and $\tau_1 = 1$ and $\tau_2 = 10$ ms for inhibitory synapses (Ali et al., 2001). The postsynaptic current at each synapse is given by

$$I_{syn}(t) = g_{syn}(t) (V - E_{syn}) \quad (3.16)$$

where E_{syn} is the reversal potential of the synapse. E_{syn} was set to 0 mV for excitatory and -75 mV for inhibitory synapses. This synapse mechanism is implemented in NEURON by the `Syn2Exp()` command.

Synapses were connected using a `NetCon()` command to a single pre-synaptic compartment stimulated by `NetStim()` with fixed mean rate but

completely random timing ($Stim.noise = 1$). Number of synapses was fixed to 10000 excitatory and 2000 inhibitory synapses (DeFelipe & Farinas, 1992).

Protocols for UP/DOWN-states

UP-states were modelled as 500 ms long periods of enhanced synaptic input and were preceded by 50 ms equilibration time and followed by 300 ms baseline, each without synaptic input. During the UP-state and baseline, 100 ms-long hyperpolarizing current pulses with an amplitude of -300 pA were injected into the soma in order to measure R_{in} during UP- and DOWN-states, respectively, and compare these values to those previously found (Waters & Helmchen, 2006). UP-states were modeled for animals of all ages while the number and properties of synapses were kept constant and only the mean activation frequency was changed. Using this approach we wanted to determine how developmental changes in sub-threshold properties might influence neuronal responses to synaptic input.

3.2 Modeling Results

Over the last few years, immense computer power has become available for neuroscience. As a consequence, increasing effort is put into building numerical models for single cells and small networks in order to deepen our understanding of the mechanisms underlying experimental observations.

Crucial for building a valid model is the knowledge of the best parameter set that reproduces experimental results. Unfortunately, most models are tuned “by hand”, often lacking objective evaluation of quality in respect to experimental data. Moreover, tuning a model is a daunting task, thus scientists are bound to accept the first reasonable parameter set (reproducing some effects), which however most likely is far away from a global minimum that would best reproduce all effects observed.

Here, we employed and evaluated an automatic parameter search method called simulated annealing (SA) algorithm, which allows searching high-dimensional parameter spaces for a near-optimal solution of an objective error function (Kirkpatrick et al., 1983; Press et al., 1991; Vanier & Bower, 1999; Weaver & Wearne, 2006).

3.2.1 Testing the SA algorithm with artificial data

One of the major problems for any parameter estimation is the fact that experimental data are never noise-free. This might lead to a different global minimum of the error function as compared to that of an ideal, noise-free measurement. In the following, we tried to estimate the error in parameters made by applying the simulated annealing algorithm to artificially generated, noisy data.

Generation of artificial data for a retrieval test

Artificial data were generated in two steps. First, voltage traces were simulated using a single compartment model ($L=90 \mu\text{m}$, diameter = $100 \mu\text{m}$) with the following parameters: (1) passive properties: specific membrane resistance $R_m = 18 \text{ k}\Omega/\text{cm}^2$, specific membrane capacitance $C_m = 1.2 \mu\text{F}/\text{cm}^2$, passive reversal potential $E_{pas} = -57 \text{ mV}$; (2) Ih: specific conductance $g_{Ih} = 1\text{e-}5 \text{ S}/\text{cm}^2$, reversal potential $E_{Ih} = -20 \text{ mV}$, fixed kinetic parameters (equation 3.1) $A = 0.01 \text{ ms}^{-1}$, $\gamma =$

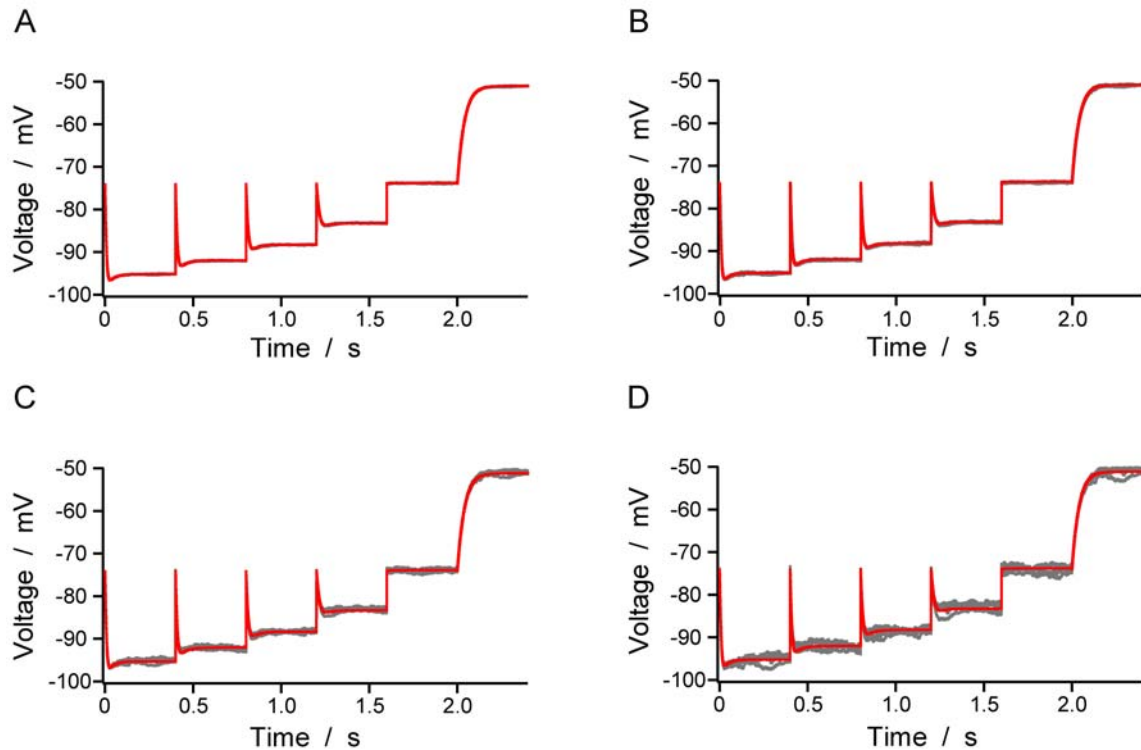


Fig. 3.4 Artificial data with different levels of noise for testing the SA algorithm. A, initial noise amplitude 0.1 mV; B, 0.2 mV; C, 0.5 mV; D, 1 mV. Red traces depict original simulated data without noise. X-axis is totally simulated time.

0.6, $q = 4.2$ elementary charges e , $V_{1/2} = -90$ mV; (3) instantaneous KIR: specific conductance $g_{KIR} = 2.3e-4$ S/cm², potassium reversal potential $E_K = -94$ mV, kinetic parameters (kept fixed) $V_h = -90$ mV, $V_c = 12.1$ mV (Day et al., 2006).

The resulting traces were smooth curves which were directly taken for “no noise” retrieval test. Curves were generated using the CVODE method and sampled with 10 kHz. Noise in electrophysiological experiments was assumed to be of $1/f$ character (Dutta & Horn, 1981; Benndorf, 1995). Thus, a series of sinusoidal functions was added to the simulated data in Igor Pro 4.0 (Wavemetrics, OR, USA). Frequency, f , of functions ran from 1 Hz to 5 kHz in 1 Hz steps; amplitudes scaled with $1/f$; phase shift within an interval $[-\pi, +\pi]$ was random for each function separately. In order to prevent that noisy data with different maximal noise amplitudes are merely scaled versions of one another, five different curves were generated with different seeds for the random number generator at each initial amplitude. Four different initial amplitudes at $f = 1$ Hz were used: 0.1 mV, 0.2 mV, 0.5 mV and 1 mV. Additionally, Gaussian offset noise with fixed standard deviation of 0.002 mV was added. Fig. 3.4 shows all artificial data used for testing.

Testing the SA algorithm on artificial subthreshold data

To test the SA algorithm, several starting temperatures and annealing schedules were examined. First, the SA algorithm was used as a downward simplex algorithm, i.e. starting temperature was set to zero. In a second run a starting temperature of 1000 (which was approximately 10% of the maximal differences in the vertices' starting errors) and an exponential decay as annealing schedule were used. Finally, the complete set of mechanics was used including automated choice of starting temperature (equation 3.11), cooling dependent on variance in encountered errors (equation 3.10) and termination criteria based on the size of the simplex in error landscape and averaged development of error values encountered (equation 3.12). The latter mode is referred to as fully automated (f. a.) mode. Example runs are shown in Fig. 3.5, applied to artificial data without noise. Note the different timescales (“simulation run”) on which the algorithms converged. It can clearly be seen that a higher temperature leads to a more erratic movement of the simplex, mirrored in the fluctuations of the example parameter. In addition, the higher the temperature, the more different “currently best”-values are encountered, as can be seen from the fluctuations in the red dots in Fig. 3.5C, right panel.

Fig. 3.6 shows the complete results of the initial test of the SA algorithm. As expected, the downward simplex algorithm ($T = 0$) took only few error function evaluations to converge, because only better error function values are accepted for movement (Fig. 3.6B). Somewhat surprising was that the final Ih parameter values were much closer to the target values with $T = 0$ than with $T = 1000$ or the f.a. algorithm, although the latter showed the least deviation from the other target parameters (Fig. 3.6A). Evaluating the lowest encountered error values E_{best} showed that for all algorithms tested often a solution was found that was better

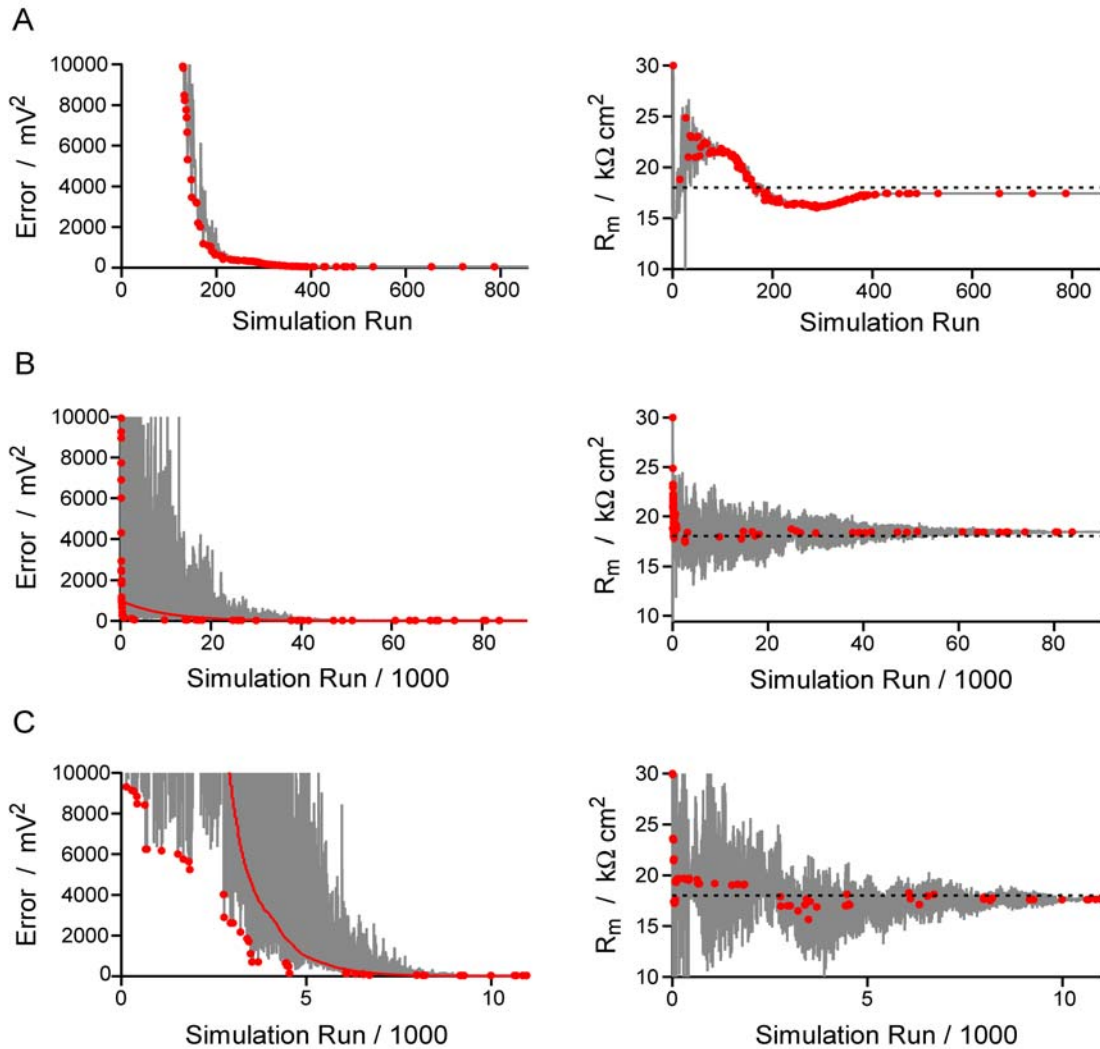


Fig. 3.5 Examples for test runs with different annealing schedules. Left panels depict errors (grey), temperature (red solid line) and encountered new best (red dots). Right panels show specific membrane resistance values (grey) as an example parameter (out of seven) with the respective current best (red dots); broken black line is the target value. A, $T = 0$. B, $T = 1000$, exponential decay. C, fully automated.

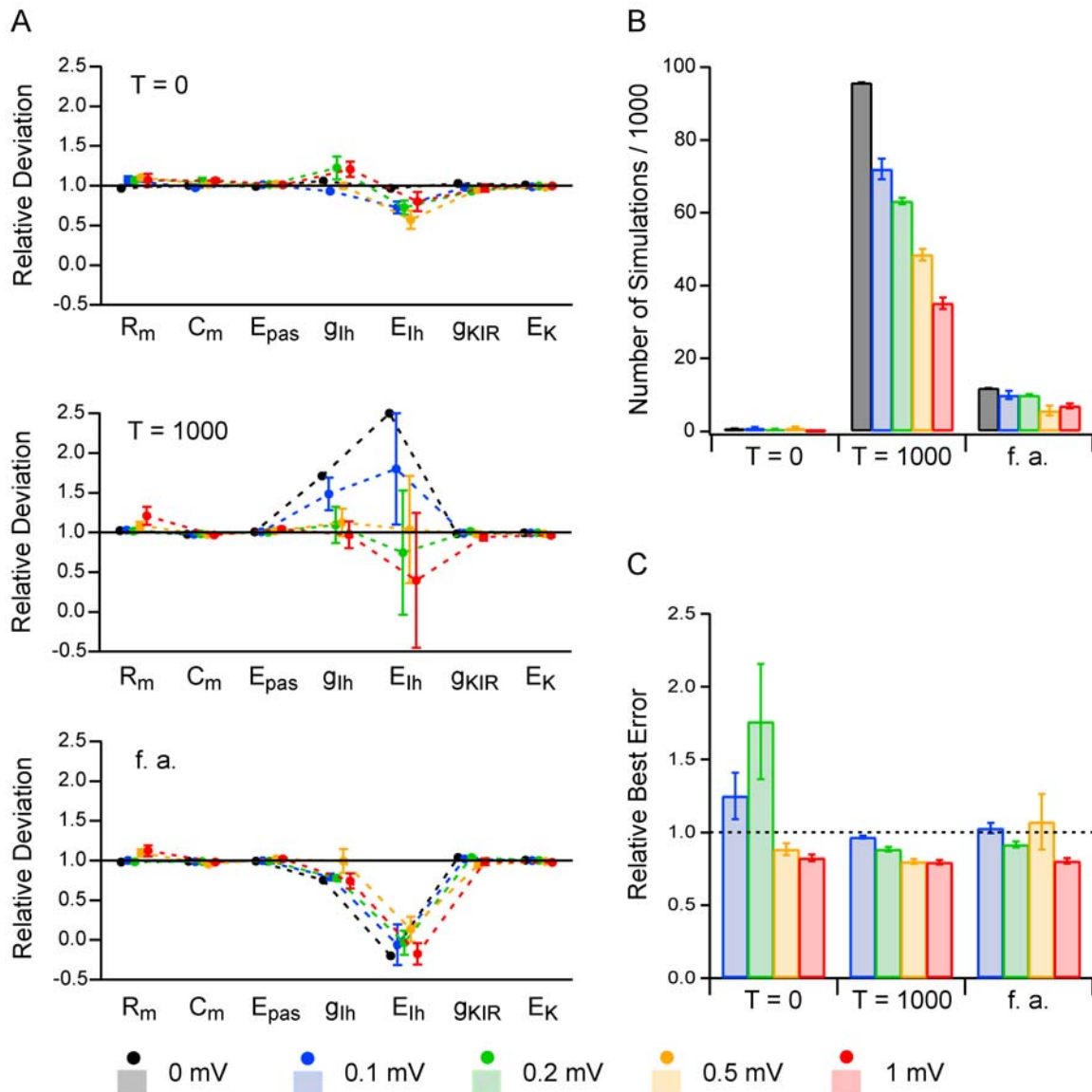


Fig. 3.6 Results of SA algorithm test under three different conditions: downward simplex ($T = 0$), exponential decay ($T = 1000$) and fully automated (f. a.). **A**, deviations in single parameters for the three different conditions after the algorithm terminated. **B**, number of error function evaluations before convergence occurred. **C**, error after convergence, divided by the theoretical best error if the correct set of parameters had been retrieved. Colors indicate the amount of noise added (see bottom).

than the target parameter set. To show this, E_{best} was divided by the absolute point-wise difference between original data and noisy data (Fig 3.6C). Most likely the algorithm also optimized the parameter set with respect to the low-frequency components of the added noise. This might also be reflected in the huge

variance in I_h conductance and reversal potential, which are the parameters least constrained due to the initially low value of g_{Ih} .

In order to test the fully automated SA algorithm for later applications with a larger set of free kinetic parameters, optimization of parameters was tested in a 14-dimensional parameter space (Fig. 3.7). While g_{Ih} was systematically over- and g_{KIR} underestimated, kinetic parameters were retrieved well with little variance. Additionally, the number of error function evaluations needed for convergence was only around 1.5 times higher than with the 7-dimensional parameter space.

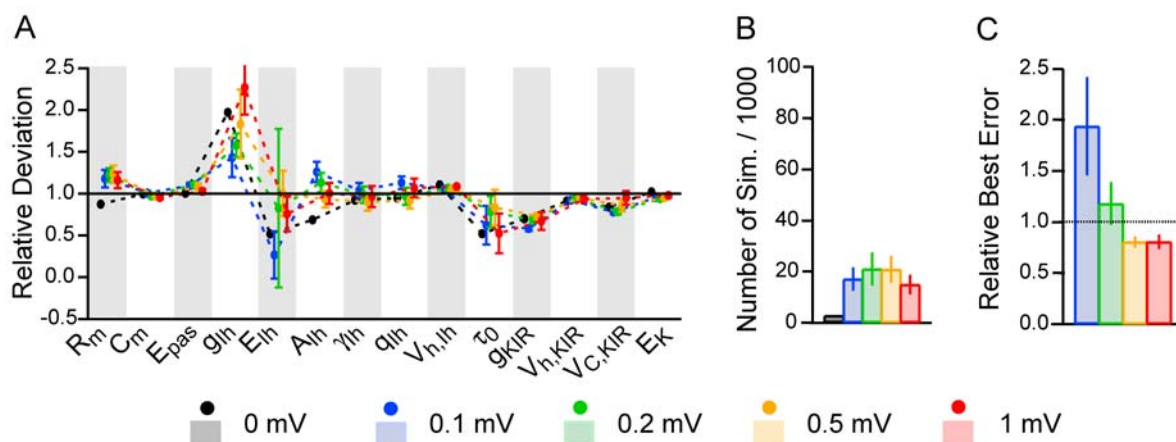


Fig. 3.7 Results of testing the fully automated SA algorithm on a 14-dimensional parameter space, now including kinetic parameters (eq. 3.1). **A**, deviations in single parameters (grey bars for better separation of parameters). **B**, number of error function evaluations before convergence occurred. **C**, error after convergence, divided by the theoretical best error. Colors indicate the amount of noise added (see bottom).

In conclusion, we decided to use the fully automated (f. a.) SA-algorithm because it performed best compared to the alternative modes with respect to minimal error and computational time needed to find a near-optimal parameter set.

3.2.2 Simulation of experimental data

Single compartment model reveals a low density of I_h in L2/3 pyramidal neurons

In order to estimate the age-dependency of total I_h -conductance G_{Ih} in comparison to total KIR conductance G_{KIR} , a single isopotential compartment (arbitrary length of 50 μm and diameter 50 μm) was equipped with passive

properties, as well as the ion channels KIR and I_h , leading to a total of 14 free parameters (see above). It was necessary to declare kinetic parameters as free parameters because the time course of sag was in most cases not reproducible with the kinetics taken from the literature (Magee, 1998; Traub et al., 2003; Day et al., 2006). Instead of fitting 400 ms per current level as in the tests, only the initial 200 ms of the voltage response were fitted for each current level. This ensured a larger relative weight of the transient behavior for the error function values. In total, 13 cells at p8, 17 cells at p14, 11 cells at p21, 10 cells at p28 and 6 cells at p45 were tested. Conductances and currents are given per area. Nevertheless, since membrane area is the same arbitrary value for all cells simulated, the development of conductances is directly comparable to that given in chapter 2.3.3 (Fig. 2.27).

Fig. 3.8 shows the results of the age-dependent single compartment model. As expected, the estimated I_h conductance was lower than the KIR conductance: at p8, both conductances were of the same order of magnitude (I_h : $6 \pm 2 \mu\text{S}/\text{cm}^2$; KIR: $24 \pm 6 \mu\text{S}/\text{cm}^2$, $p < 0.01$) whereas at p45, where steady state was reached, there was a large difference between the two conductances (I_h : $29 \pm 7 \mu\text{S}/\text{cm}^2$; KIR: $768 \pm 315 \mu\text{S}/\text{cm}^2$, $p < 0.05$). Leak conductance increased from $67 \pm 7 \mu\text{S}/\text{cm}^2$ at p8 to $180 \pm 40 \mu\text{S}/\text{cm}^2$ at p45 ($p < 0.001$). Reversal potentials remained fairly constant (Fig. 3.8B), showing only a slight decrease in leak ($p < 0.05$) and K^+ reversal potentials ($p > 0.05$). Furthermore, the reversal potentials for leak and K^+ were similar ($p > 0.05$), suggesting a major contribution of K^+ channels to leak conductance.

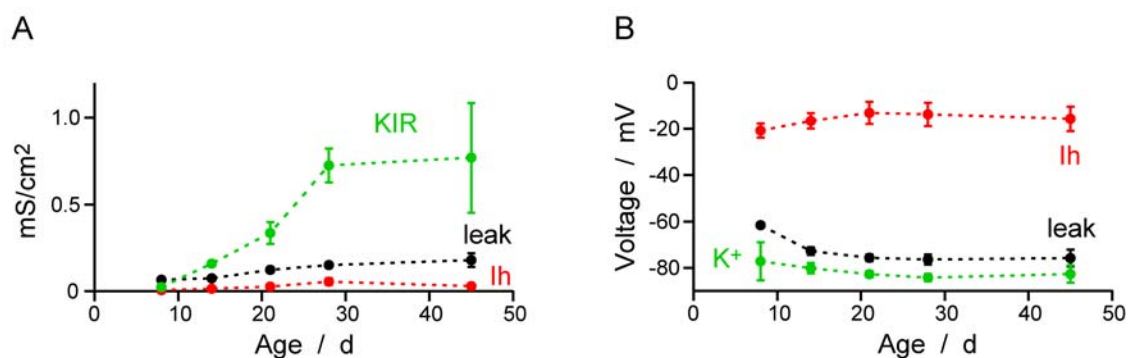


Fig. 3.8 Conductance densities and reversal potentials from single compartment fit. **A**, conductance densities versus age of simulated cells. **B**, corresponding reversal potentials versus age. Channel and ion types, respectively, are color-coded.

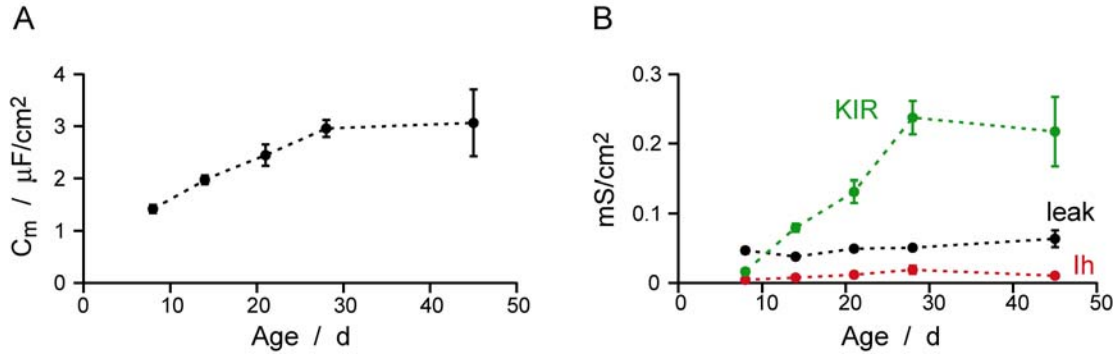


Fig. 3.9 Changes in membrane capacitance and effect on conductances. **A**, age-dependence of specific membrane capacitance C_m . **B**, conductance values normalized to $C_m = 1 \mu\text{F}/\text{cm}^2$. Channel types are color-coded.

In order to test the extent to which the observed changes in conductances are due to developmental changes in morphology, all conductances were normalized to a specific membrane capacitance of $1 \mu\text{F}/\text{cm}^2$. Thereby, effects of an increase in electrically “visible” membrane area are cancelled. Specific membrane capacitance C_m roughly doubled from $1.4 \pm 0.1 \mu\text{F}/\text{cm}^2$ at p8 to $3.1 \pm 0.6 \mu\text{F}/\text{cm}^2$ at p45 ($p < 0.001$; Fig. 3.9A), indicating an increase in efficient membrane surface during development. After normalization to C_m (Fig. 3.9B) the pronounced increase in specific KIR conductance still prevails, but the increase in leak conductance is much less pronounced from $47 \pm 4 \mu\text{S}/\text{cm}^2$ at p8 to $64 \pm 12 \mu\text{S}/\text{cm}^2$ at p45 ($p = 0.1$; Fig. 3.9B, black trace), suggesting that the mature density of leak channels is established already at an early stage of development and that any increase in absolute leak conductance is due to an increase in cell surface area.

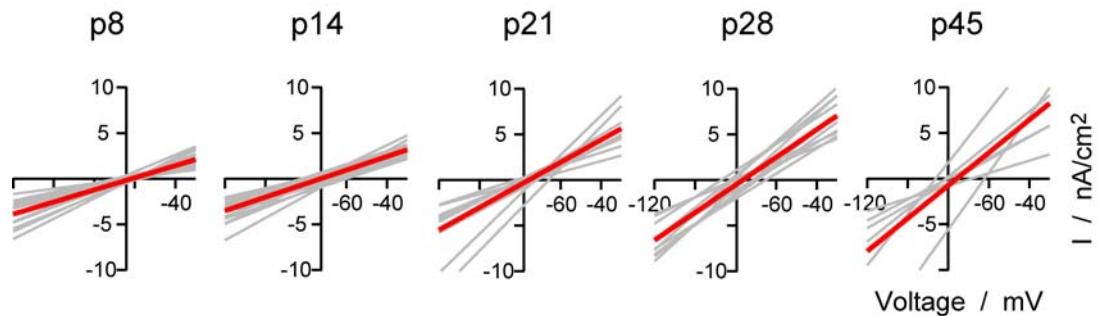


Fig. 3.10 Simulated leak currents from different ages. Individual experiments in light grey, curves from mean values in red; y-axis intercepts at experimentally determined V_{rest} .

Because not only conductances but also kinetic parameters and reversal potentials were free parameters in these simulations it is particularly interesting to see how the I-V relationships evolve as the cells mature. In Fig. 3.10, the fitted leak currents are shown. The slope of the mean I-V curve (red) increases with age, leading to the experimentally observed decrease in R_{in} . Note that also the mean leak reversal potential is at all ages close to the experimentally determined mean resting potential (intercept of x- and y-axis). Due to its small conductance in L2/3 pyramidal neurons the I_h current does not play a significant role in steady-state behavior but gives rise to the small sag observed in these cells. Fig. 3.11 depicts the development of I_h current in these cells during maturation. Around resting potential (intercept of x- and y-axis) there is practically no I_h current present due to a rather steep activation curve centered around more hyperpolarized half-activation $V_{1/2}$. Little change in mean steady state activation

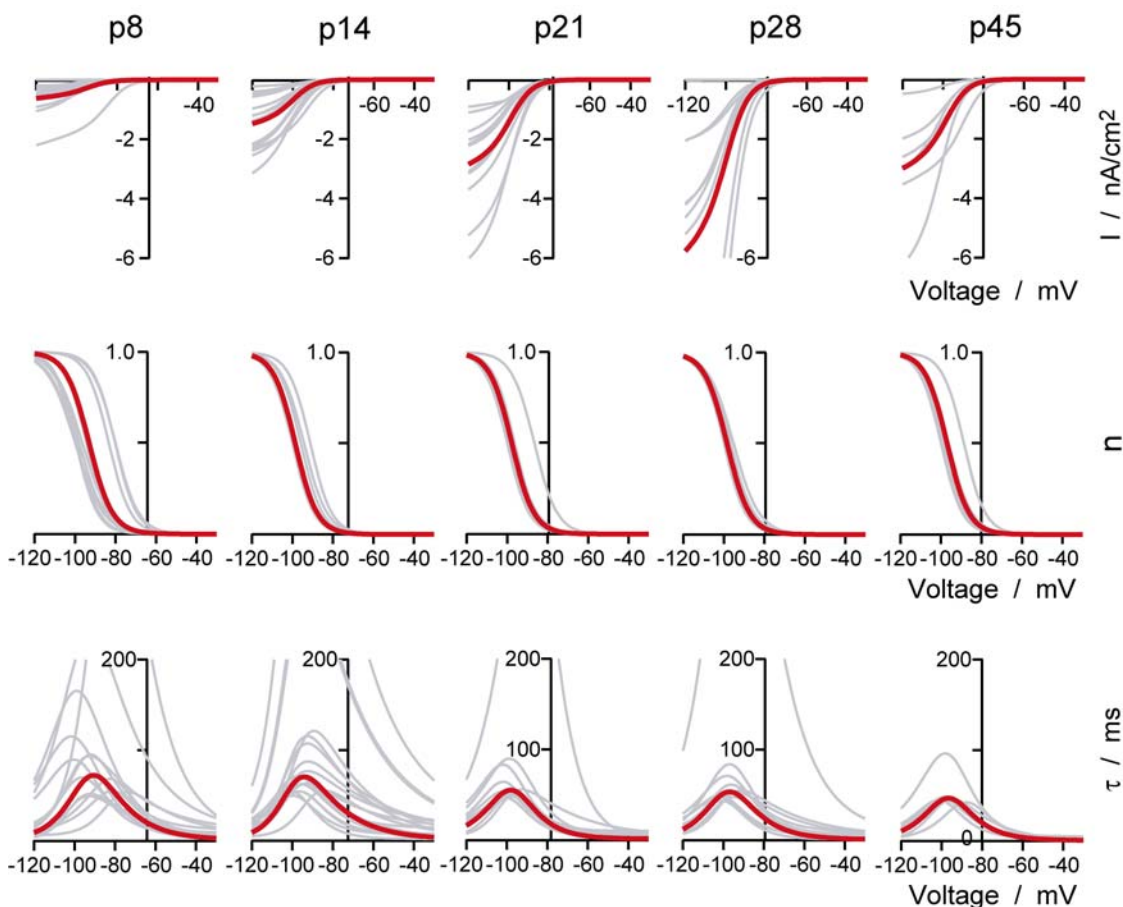


Fig. 3.11 I_h currents and kinetics at different ages. Upper row, current contribution from I_h . Middle row, steady state activation curve. Lower row, activation time constants. Individual experiments in light grey, curves from mean values in red; y-axis intercepts at experimentally determined V_{rest} .

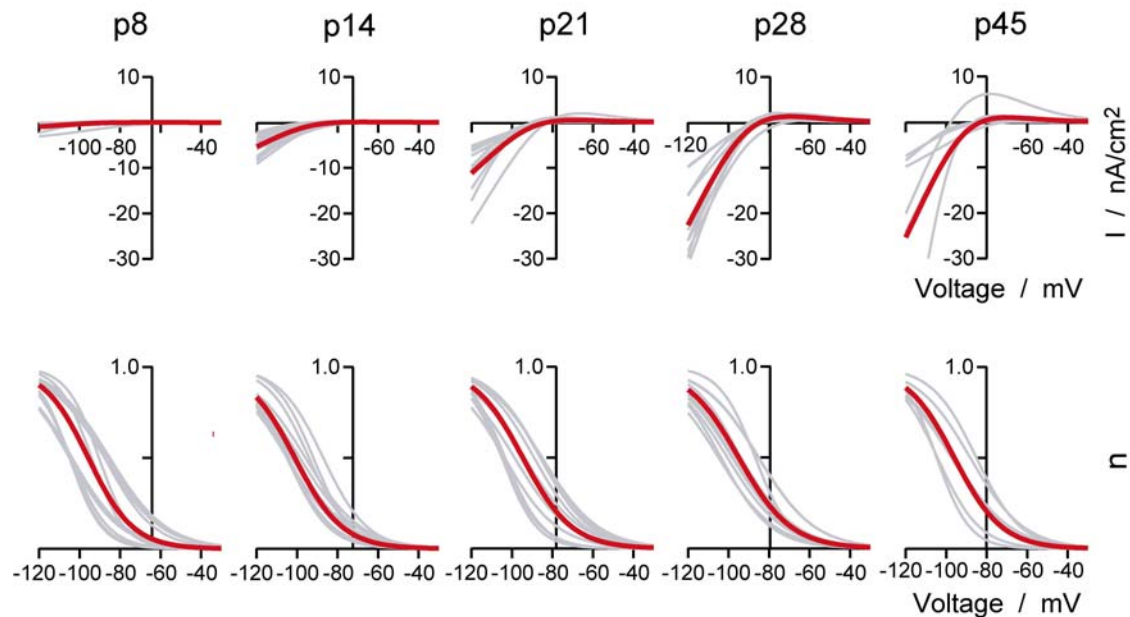


Fig. 3.12 KIR currents and kinetics at different ages. Upper row, current contribution from KIR. Lower row, steady-state activation. Individual experiments in light grey, curves from mean values in red; y-axis intercepts at experimentally determined V_{rest} .

	p8	p14	p21	p28	p45
$g_{leak} / \mu\text{S}/\text{cm}^2$	67 ± 7	74 ± 4	123 ± 16	151 ± 12	180 ± 40
E_{leak} / mV	-62 ± 1	-73 ± 2	-76 ± 1	-76 ± 2	-76 ± 4
$C_m / \mu\text{F}/\text{cm}^2$	1.4 ± 0.1	2.0 ± 0.1	2.4 ± 0.2	3.0 ± 0.2	3.1 ± 0.6
$g_{lh} / \mu\text{S}/\text{cm}^2$	6 ± 1	15 ± 2	27 ± 4	56 ± 19	29 ± 7
E_{lh} / mV	-21 ± 3	-17 ± 3	-13 ± 5	-14 ± 5	-16 ± 5
$A_{lh} / 1/\mu\text{s}$	7 ± 1	8 ± 1	9 ± 1	10 ± 1	11 ± 1
γ_{lh}	0.65 ± 0.04	0.7 ± 0.03	0.48 ± 0.04	0.57 ± 0.05	0.51 ± 0.04
q_{lh} / e	4.6 ± 0.1	4.9	4.9 ± 0.1	4.8 ± 0.1	4.9 ± 0.1
$V_{1/2,lh} / \text{mV}$	-93 ± 2	-99 ± 1	-98 ± 1	-99 ± 1	-97 ± 2
$\tau_{0,lh} / \text{ms}$	1.1 ± 0.2	1.2 ± 0.1	1.5 ± 0.3	0.8 ± 0.3	0.6 ± 0.2
$g_{KIR} / \mu\text{S}/\text{cm}^2$	24 ± 6	160 ± 15	337 ± 63	724 ± 98	769 ± 315
E_K / mV	-77 ± 8	-80 ± 2	-83 ± 1	-84 ± 2	-83 ± 4
$V_{h,KIR} / \text{mV}$	-96 ± 3	-101 ± 1	-95 ± 3	-95 ± 2	-96 ± 3
$V_{c,KIR} / \text{mV}$	11.0 ± 0.7	11.8 ± 0.4	12.1 ± 0.6	13.0 ± 0.5	11.8 ± 1

Table 2 Parameters from multi-parameter fitting in a single compartment model.

was observed over the different ages. Also, the time constant τ was stable, although a systematic shift towards an on average faster activation was observed. All kinetic parameters are given in table 3.1. In comparison to Ih, the currents mediated by KIR channels are significantly larger (Fig. 3.12). In addition, due to a shallower steady-state activation curve more KIR channels are active around resting membrane potential of the cell (experimentally determined mean value as intercept of x- and y-axis). Since the potassium reversal potential lies below the leak reversal potential, also the KIR current reverses below resting potential. Over the ages, this current increases significantly, as was already obvious from the conductances alone, thus becoming more important with age for contributing to the steady state currents.

The age-dependent single-compartment model

Using the mean parameters given in Table 3.1, an age-dependent single compartment model was built. This model reproduces the sub-threshold voltage response of L2/3 pyramidal cells of different ages (Fig. 3.13; compare Fig. 2.9). Diameter and length were set to 50 μm (the same value as during actual parameter search; see above) to allow usage of the conductance densities found during multi-parameter fitting. Injected currents ranged from -500 pA to +500 pA (raising some of the cells well above AP threshold) in steps of 50 pA.

While in younger cells relatively low current injections (between 150 pA and 200 pA at p8) are sufficient to reach AP threshold, in the majority of matured cells even a current injection of 500 pA does not depolarize the cells sufficiently

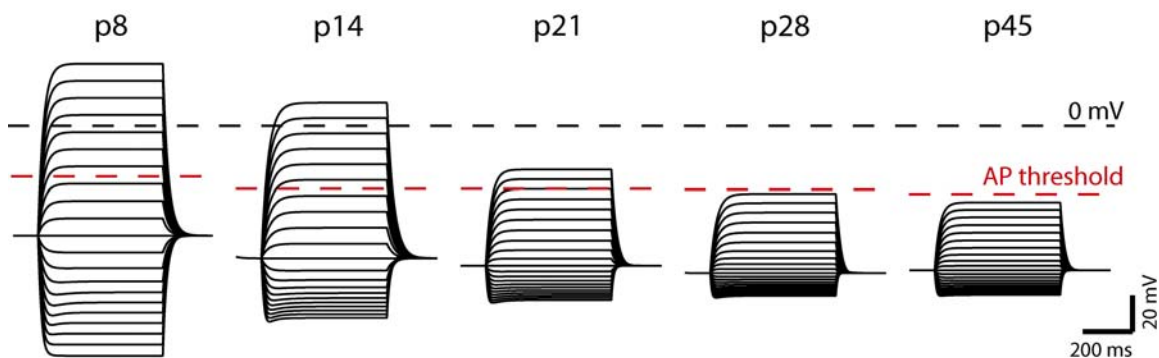


Fig. 3.13 Resulting V-I curves from averaged single compartment models. Current injections ranged from -500 pA to +500 pA in steps of 50 pA. Black dashed line represents 0 mV, red dashed lines the measured AP threshold for the respective age.

to reach AP threshold. Of course, this result is based on the assumption that leak, I_h and KIR are the only ionic conductances present in these cells.

Simulated pharmacology

In order to test whether the simulated channels do have the effect on anomalous rectification as observed in our experiments, additional simulations with complete blocking of I_h and KIR, respectively, were performed. The respective conductance densities were set to 0 S/cm^2 .

Fig. 3.14 shows the results of these simulated pharmacological experiments for two ages, p14 and p28. At p14, application of $50 \mu\text{M BaCl}_2$ almost linearized the voltage response, while blocking of I_h showed little effect (compare Figs. 2.19 and 2.22). In p28 cells, though, $50 \mu\text{M BaCl}_2$ failed to

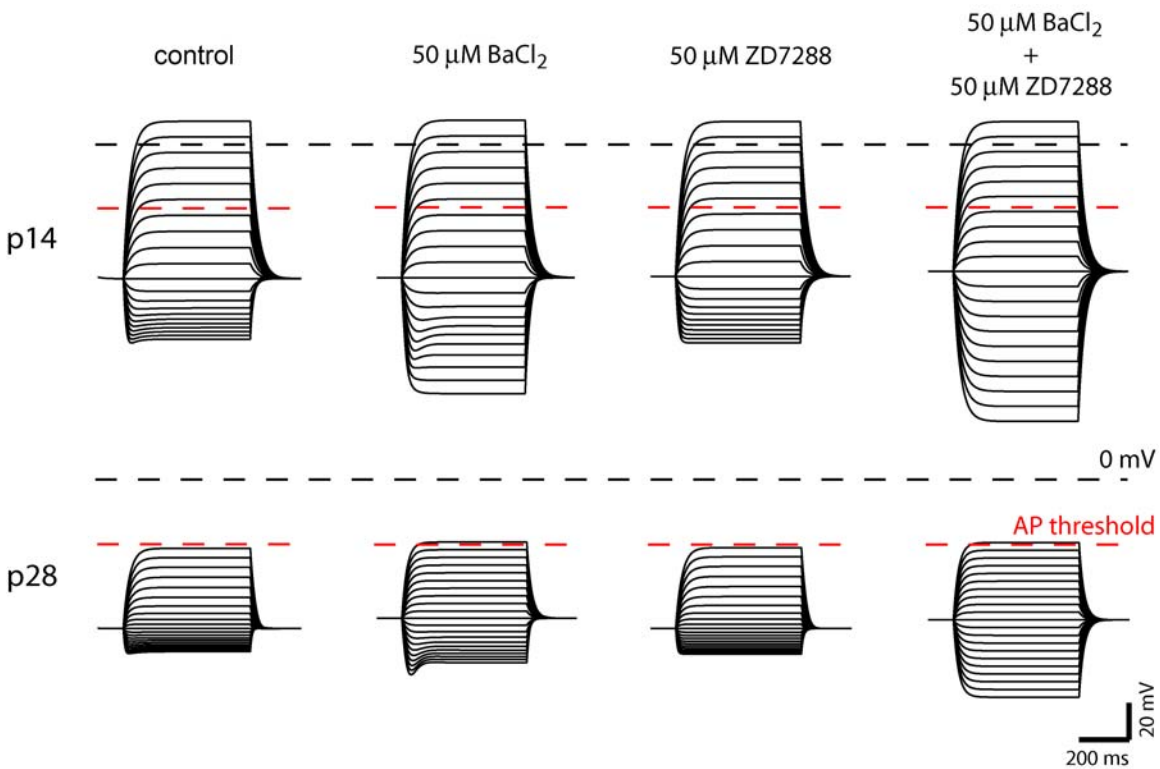


Fig. 3.14 Simulated pharmacological block of KIR and I_h for two ages, p14 (upper row) and p28 (lower row). Current injection ranged from -500 pA to $+500 \text{ pA}$ in steps of 50 pA . Control traces are the same as in Fig. 3.13. For $50 \mu\text{M BaCl}_2$, g_{KIR} was set to zero, for $50 \mu\text{M ZD7288}$, g_{Ih} was set to zero. The last column represents the purely passive model with no active conductances ($g_{KIR}, g_{Ih} = 0$). Black broken lines are 0 mV , red broken lines show experimentally determined AP threshold.

completely remove AR due to stronger presence of Ih, which elicits a more prominent sag when KIR is blocked due to stronger activation during hyperpolarization. However, blocking of Ih alone shows little effect on AR, suggesting that the overall effect of Ih is small.

3.2.3 Full-morphology models

In order to get a more realistic estimate of channel densities in L2/3 pyramidal neurons, the SA algorithm was employed to find parameter sets for reconstructed morphologies.

Full-morphology models with constant conductance densities

In a first set of simulations we tried to estimate more realistic values for membrane properties based on our experiments. Since we did not measure several locations in the dendrite tree at the same time during our experiments, we lack the knowledge of how channel densities might change with distance from soma. Thus, we decided to reproduce our experimental findings in a first approximation with homogenous channel distributions in reconstructed morphologies, with the hope that more distal parts are electrically uncoupled from the proximal parts and do not substantially influence the response obtained at the soma. For all simulations presented in this paragraph, axial resistance R_{ax} was set to 120 Ω -cm to prevent over-fitting. Channel kinetics were variable with the same free parameters and within the same boundaries as for the single compartment model (see above).

Results are presented in Table 3.2. The same trends as in the single compartment models are obvious for the passive parameters: g_{leak} increases, while E_{leak} shifts to more hyperpolarized values. C_m again increases with age, an effect that might have several reasons: (1) we did not correct morphologies for shrinkage, which might lead to under-estimation of dendritic diameters; (2) spines, which add to the membrane surface while leaving the diameter unaltered, were not included in the morphology; (3) R_{ax} was chosen too high, thereby electrically “hiding” distal parts of the dendritic tree and requiring higher values in order to reproduce the transients observed. Ih conductance densities are in good agreement with those obtained in the single compartment models. Except

3 Modeling

	p8	p14	p21	p28	p45
$g_{leak} / \mu\text{S}/\text{cm}^2$	94 ± 12 (67 ± 7)	60 ± 4 (74 ± 4)*	116 ± 11 (123 ± 16)	144 ± 17 (151 ± 12)	141 ± 20 (180 ± 40)
E_{leak} / mV	-57 ± 1 (-62 ± 1)*	-73 ± 2 (-73 ± 2)	-73 ± 1 (-76 ± 1)*	-64 ± 2 (-76 ± 2)**	-73 ± 3 (-76 ± 4)
$C_m / \mu\text{F}/\text{cm}^2$	2.9 ± 0.4 (1.4 ± 0.1)**	1.9 ± 0.1 (2.0 ± 0.1)	2.7 ± 0.2 (2.4 ± 0.2)	2.4 ± 0.3 (3.0 ± 0.2)	3.6 ± 0.7 (3.1 ± 0.6)
$g_{Ih} / \mu\text{S}/\text{cm}^2$	15 ± 5 (6 ± 1)**	11 ± 2 (15 ± 2)	23 ± 3 (27 ± 4)	16 ± 8 (56 ± 19)	134 ± 62 (29 ± 7)
E_{Ih} / mV	-36 ± 0 (-21 ± 3)*	-28 ± 5 (-17 ± 3)	-27 ± 7 (-13 ± 5)	-41 ± 9 (-14 ± 5)*	-37 ± 11 (-16 ± 5)
$A_{Ih} / \mu\text{s}^{-1}$	7 ± 1 (7 ± 1)	7 ± 1 (8 ± 1)	8 ± 1 (9 ± 1)	7 ± 2 (10 ± 1)	10 ± 1 (11 ± 1)
Y_{Ih}	0.55 ± 0.12 (0.65 ± 0.04)	0.61 ± 0.04 (0.7 ± 0.03)	0.61 ± 0.04 (0.48 ± 0.04)*	0.54 ± 0.06 (0.57 ± 0.05)	0.61 ± 0.05 (0.51 ± 0.04)
q_{Ih} / e	4.6 ± 0.2 (4.6 ± 0.1)	4.7 ± 0.1 (4.9)	4.4 ± 0.1 (4.9 ± 0.1)**	4.4 ± 0.2 (4.8 ± 0.1)	4.7 ± 0.1 (4.9 ± 0.1)
$V_{1/2,Ih} / \text{mV}$	-91 ± 5 (-93 ± 2)	-98 ± 2 (-99 ± 1)	-90 ± 2 (-98 ± 1)**	-99 ± 3 (-99 ± 1)	-97 ± 4 (-97 ± 2)
$\tau_{0,Ih} / \text{ms}$	1.2 ± 0.1 (1.1 ± 0.2)	1.3 ± 0.2 (1.2 ± 0.1)	2.0 ± 0.7 (1.5 ± 0.3)	0.7 ± 0.2 (0.8 ± 0.3)	0.9 ± 0.2 (0.6 ± 0.2)
$g_{KIR} / \mu\text{S}/\text{cm}^2$	114 ± 40 (24 ± 6)**	184 ± 15 (160 ± 15)	545 ± 94 (337 ± 63)	997 ± 215 (724 ± 98)	1686 ± 545 (769 ± 315)
E_K / mV	-95 ± 3 (-77 ± 8)	-92 ± 1 (-80 ± 2)**	-90 ± 1 (-83 ± 1)**	-91 ± 3 (-84 ± 2)	-87 ± 1 (-83 ± 4)
$V_{h,KIR} / \text{mV}$	-99 ± 3 (-96 ± 3)	-101 ± 2 (-101 ± 1)	-95 ± 2 (-95 ± 3)	-94 ± 4 (-95 ± 2)	-97 ± 3 (-96 ± 3)
$V_{C,KIR} / \text{mV}$	13.0 ± 0.6 (11.0 ± 0.7)	11.3 ± 0.6 (11.8 ± 0.4)	9.9 ± 0.5 (12.1 ± 0.6)	11.4 ± 0.8 (13.0 ± 0.5)	11.0 ± 0.8 (11.8 ± 1)

Table 3.2 Parameters from multi-parameter fitting in full morphologies. Values in brackets are from single-compartment fits (Table 3.1); * = significant ($p < 0.05$), ** = highly significant ($p < 0.01$).

at p8, where conductances are very small, none of these deviations is significant. Also the kinetic properties are overall unchanged, although a systematic, though not significant shift of $E_{rev,Ih}$ towards more hyperpolarized values was observed. KIR conductance densities and kinetic parameters were found to resemble those found in single compartment models. Although a systematic trend towards higher conductance densities was found, these differences were not significant.

As was stated above, a model that does not take into account the voltage responses in the dendrites is of limited value. Thus, in a second model, data from dual recordings were combined with detailed morphological reconstruction to build a detailed full-morphology model with heterogeneous ion channel distributions, using the same parameter search approach.

Refining full-morphology models with dendritic voltage measurements

In cells with extensive dendritic branching, voltage control of more distal regimes of the dendritic tree is difficult (e.g. Schaefer et al., 2003). Thus, for building a more realistic model with conductance distributions that depend on distance from the soma, the voltage response to somatic current injection is to be measured at dendritic sites. Data of dual recordings from L2/3 pyramidal neurons have kindly been provided by Matthew E. Larkum, along with the corresponding reconstructed morphologies. Unfortunately, only one cell turned out to be usable due to large voltage shifts in the dendritic recording electrode visible in the recordings.

Four additional parameters were introduced compared to the single-compartment model and the full-morphology model with constant conductance densities: (1) axial resistance R_{ax} , which governs the spread of voltage signal along the dendritic cable; (2) exponential distribution of Ih channels (analogous to observations in L5 pyramidal cells, with larger Ih conductance in the distal parts of the apical tree (Kole et al., 2006)) required a positive length constant λ_{Ih} , describing the local conductance density relative to Ih conductance at soma; (3) spatial distribution of KIR and leak channels was described by exponential functions, leading to two additional length constants λ_{KIR} and λ_{leak} as free parameters. Length constants were allowed to assume positive as well as negative values, leading to an increase or decrease, respectively, in channel density along the dendrite away from the soma. The error function was changed by adding up the errors in the somatic and dendritic voltage traces:

$$E = \sum_{I_{inj}} \left((v_{soma,sim} - v_{soma,target})^2 + (v_{dend,sim} - v_{dend,target})^2 \right) \quad (3.17)$$

Fig. 3.15 shows the reconstructed cell (age p28), positions of the two recording micropipettes, and the original data measured at the two sites (dendritic electrode 184 μm away from soma). Since the dendritic recording is noisier than the somatic one, fitted conductance of I_h at the dendritic site is less reliable than at the soma. At both sites, anomalous rectification is present in the voltage response upon somatic current injection.

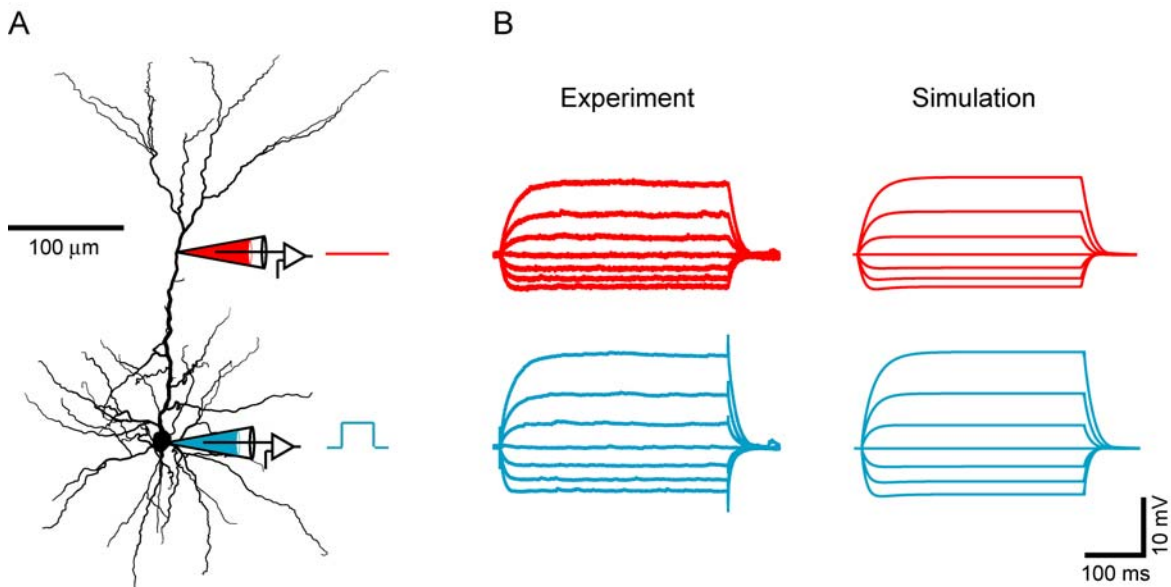


Fig. 3.15 Morphology and electrophysiological data used for constraining full-morphology L2/3 pyramidal cell model with non-constant channel distributions. A, reconstructed morphology from in vitro experiment. The two recording sites are indicated, voltage traces in B in respective colors. B, respective voltage response upon somatic current injection. Left, experimental traces; right, simulated traces after convergence of SA algorithm. Current injections through the somatic electrode ranged from -300 to +300 pA in steps of 100 pA. (Data kindly provided by Matthew E. Larkum.)

In the resulting best parameter set, kinetic parameters were very similar to those found in the single compartment model: $A_{Ih} = 10 \text{ us}^{-1}$, $\gamma_{Ih} = 0.6$, $q_{Ih} = 4.7 e$, $V_{1/2,Ih} = -98 \text{ mV}$, $\tau_{0,Ih} = 1.4 \text{ ms}$, $V_{h,KIR} = -87.7 \text{ mV}$, $V_{c,KIR} = 11.3 \text{ mV}$. Somatic leak conductance was $111 \text{ }\mu\text{S}/\text{cm}^2$ ($E_{leak} = -69.1 \text{ mV}$), with a very high length constant along the dendrite ($\lambda_{leak} = 138.5 \text{ mm}$) compared to the dimensions of the cell. This suggests that passive membrane properties are the same at every site in the dendritic tree. Specific membrane capacitance was $C_m = 1.8 \text{ }\mu\text{F}/\text{cm}^2$. Axial resistance was found to be $R_{ax} = 191 \text{ }\Omega\text{cm}$. KIR conductance was $578 \text{ }\mu\text{S}/\text{cm}^2$ at the soma and decreased with a length constant of $\lambda_{KIR} = 117 \text{ }\mu\text{m}$ along the

dendrites. At the same time, I_h conductance density increased from $10 \mu\text{S}/\text{cm}^2$ at the soma with a length constant of $\lambda_{I_h} = 207 \mu\text{m}$.

As a control simulation, we tried to reproduce experimental data from the same cell where current injection occurred through the dendritic micropipette and the response was simultaneously measured at the soma. The parameters were fixed to the values obtained from fitting the traces with somatic current injection. Experimental and simulated traces are in close agreement (Fig. 3.16). A slight difference was that $R_{in,dendrite}$ was larger in simulations than in experiments. Still, somatic voltage response upon dendritic current injection is reproduced correctly. This indicates that the set of parameters found is useful for simulation of more complex voltage patterns such as stochastic activation of synapses in the dendritic tree (see below).

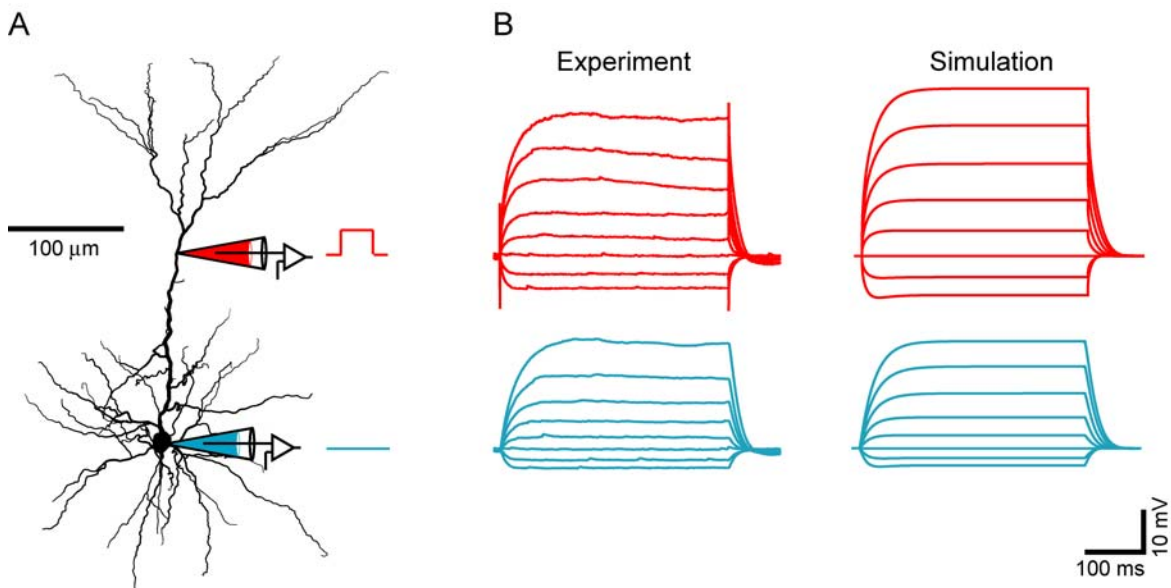


Fig. 3.16 Simulation with dendritic current injection. Same cell and parameters as in Fig. 3.15. A, reconstructed morphology. Current injections were applied to the dendrite $184 \mu\text{m}$ from soma. Voltage traces in B in respective colors. B, respective voltage response upon somatic current injection. Left, experimental traces; right, simulated traces after convergence of SA algorithm. Current injections through the dendritic electrode ranged from -200 to $+500 \text{ pA}$ in steps of 100 pA . (Data kindly provided by Matthew E. Larkum.)

3.2.4 Simulation of *in vivo* UP- and DOWN states

In the recent study of Waters & Helmchen (2006), compartmental models with a phenomenological mechanism for reproducing anomalous rectification were used for assessing the influence of non-linear V-I relationships on synaptic integration. Here, we wanted to test how our mechanistic conductance-based, age-dependent model behaves during episodes of stochastic synaptic input resembling spontaneous *in vivo* activity (UP-states).

Age-dependent single-compartment models

For determining the age-dependency of changes in number or activation frequency of synapses, the single-compartment model presented in chapter 3.2.2 was used. Properties of single synapses and simulation protocols are described in 3.1.4. Simulations were done with fixed timesteps every 25 μ s. In a first step, UP- and DOWN-states were reproduced for p45 animals according to measurements from adult rats. To this end, 10000 excitatory and 2050 inhibitory synapses (De Felipe & Farinas, 1992; Waters & Helmchen, 2006) converged onto a single compartment. Active properties were inserted following Table 3.1, last column (p45) in order to build an adult cell. Five runs with different seeds for the random number generator setting PSP events were done. Steady state voltage deflections from V_{rest} and UP-state were determined by averaging of the last 50 ms of the averaged voltage response upon current injection of -300 pA.

Fig. 3.17 shows single runs and the average trace. Mean activation rates of 0.18 Hz for excitatory and 0.03 Hz for inhibitory synapses were sufficient to elicit a depolarization of 14 mV (-78.1 mV at rest to -64.1 mV), while in accordance to experimental findings *in vivo*, R_{in} increased during UP-states. While current injection of -300 pA without synaptic input lead to a hyperpolarization of -9.5 mV ($R_{in} = 31.7$ M Ω), injecting the same current during the UP-state lead to a mean hyperpolarization of -14.9 mV ($R_{in} = 49.7$ M Ω).

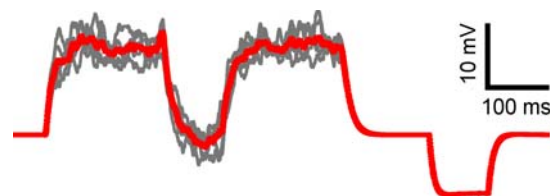


Fig. 3.17 Simulated UP/DOWN states in a L2/3 single compartment model for age p45. Two current injections of -300 pA for 100 ms occurred during and after the UP-state. Grey traces show single runs, red trace shows the average.

In a subsequent step, the numerical experiment was repeated with the averaged single compartment models of younger cells presented above. The same number of synapses and firing rates were used. It is important to note that these activation patterns are purely hypothetical as UP- and DOWN-states have not been examined systematically in younger rats. Also, a constant number of synapses with the same synaptic strength almost certainly do not represent the conditions during postnatal development. Nevertheless, it is instructive to see how immature cells would respond to such synaptic activation. Results are shown in Fig. 3.18. The voltage deflections and respective values for R_{in} are listed in Table 3.3:

Our age-dependent single-compartment model of L2/3 pyramidal cells shows, that the amplitude of UP-states elicited by the same number and mean activation frequency of synapses as in p45 animals decreases as L2/3 pyramidal

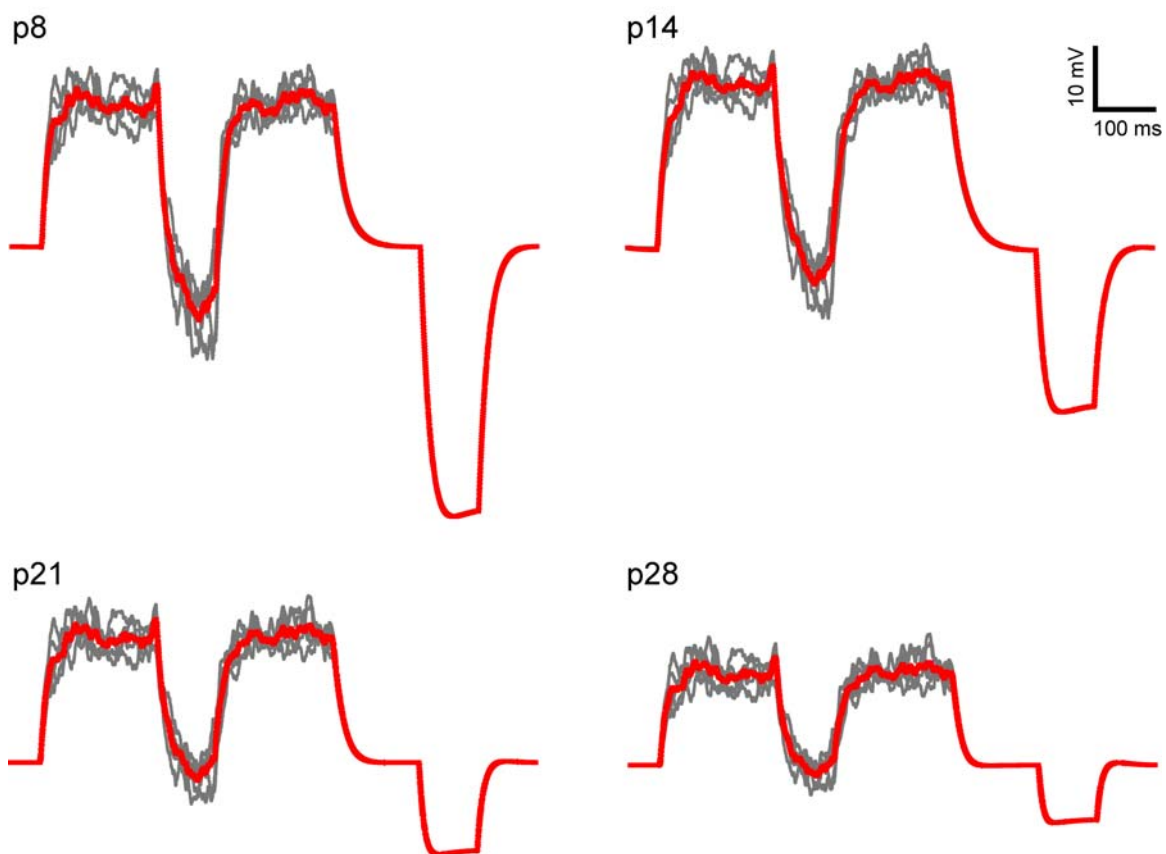


Fig. 3.18 Simulated UP/DOWN states in a L2/3 single compartment model for different ages. Traces are shifted to the same arbitrary V_{rest} to allow a better comparison between ages. Two current injections of -300 pA for 100 ms occurred during and after the UP-state. Grey traces show single runs, red trace shows the average.

3 Modeling

	p8	p14	p21	p28	p45
V_{rest} / mV	-62.2	-74	-78.3	-80.2	-78.1
V_{UP} / mV	-38.9	-47.1	-58.5	-65.5	-64.1
$\Delta V / \text{mV}$	23.3	26.9	19.8	14.7	14
$R_{in,rest} / \text{M}\Omega$	146	85.3	47	29.7	31.7
$R_{in,UP} / \text{M}\Omega$	109.7	101.3	70	51	49.7
$R_{in,UP}/R_{in,rest}$	0.75	1.19	1.49	1.72	1.57

Table 3.3 Results of simulations of UP/DOWN states in single compartment model cells at different ages.

cells mature. This is due to the decrease in input resistance. The only exception is in young cells at age p8, where the amplitude is smaller than at p14. This might be attributable to a decrease in R_{in} for EPSCs that arrive later during a train and thus lead to a smaller depolarization. This is also reflected in the fact, that $R_{in,UP}/R_{in,rest} < 1$ at p8. At this age, the KIR conductance density presumably is not sufficient to counteract the conductance increase during episodes of higher synaptic activity.

In order to estimate the level of synaptic activity necessary to induce UP-states during postnatal development, we adjusted the mean synaptic activation frequency to elicit UP-states of about 15 mV amplitude. One has to note, however, that knowledge of UP-state amplitude in young animals is

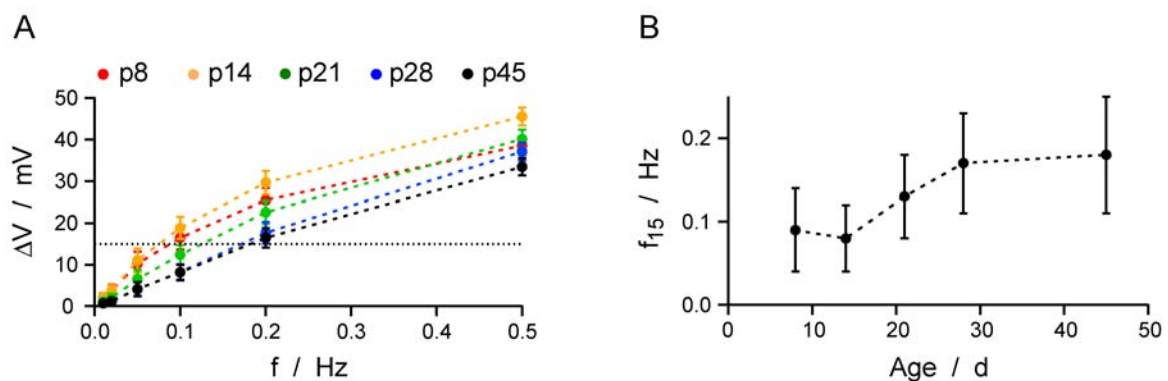


Fig. 3.19 Dependence of UP-state amplitude on mean synaptic activation frequency (data as mean \pm standard deviation). A, UP-state amplitude versus mean synaptic activation frequency. Ages are color-coded, dotted line denotes experimental value for p28. B, mean synaptic activation frequency necessary to elicit UP-states of 15 mV amplitude, versus age, assuming the same number of synapses for all ages.

	p8	p14	p21	p28	p45
$\Delta V_{0.5} / \text{mV}$	39 ± 2	46 ± 2	40 ± 2	37 ± 2	33 ± 2
f_{15} / Hz	0.09 ± 0.05	0.08 ± 0.04	0.13 ± 0.05	0.17 ± 0.06	0.18 ± 0.07

Table 3.4 Age-dependent UP-state properties: ΔV at tested maximal mean frequency $f = 0.5$ Hz and frequency needed to elicit UP-states of 15 mV amplitude. Data as mean \pm standard deviation.

scarce, and this scenario is therefore hypothetical. Also, it is unclear whether changes in UP-state amplitude are due to changes in number of synapses, synaptic strength, synaptic activation frequency, ratio between excitation and inhibition, or a combination thereof. Thus, the prediction of our model will need to be tested experimentally in the future.

Synaptic input onto refined full-morphology model

In order to test whether the number and mean activation frequency of synapses found in single compartments elicit comparable UP- and DOWN-states in model cells based on reconstructed morphologies, the refined full-morphology sub-threshold model as presented in the last chapter was used. For this simulation a homogeneous distribution of synapses was applied to the morphology. UP/DOWN-state protocol was the same as for the single-compartment cells.

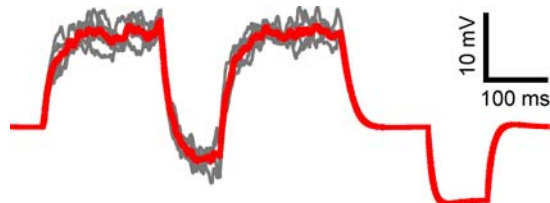


Fig. 3.20 Simulated UP/DOWN states in a fully reconstructed L2/3 neuron with heterogeneous ion channel distributions. Two current steps of -300 pA for 100 ms were injected during and after the UP-state. Grey traces show single runs, red trace shows the average.

Fig. 3.20 shows the result of five UP/DOWN-state simulations with a homogenous distribution of 9911 excitatory and 1982 inhibitory synapses on the dendritic tree. With the same mean synaptic frequencies as for the p45 single-compartment model, an UP-state of 14.4 mV was elicited ($V_{UP} = -67$ mV vs $V_{rest} = -81.4$ mV). R_{in} increased 1.64-fold (from 38.7 M Ω at rest to 63.3 M Ω during UP-

state), which is in good agreement with the value obtained in single-compartment cells.

3.3 Discussion

In the following paragraphs, we will compare our L2/3 pyramidal neuron model to previously built models, set our model parameters in relationship to our experimental data and interpret the predictions made by the age-dependent model in respect to UP- and DOWN-states.

3.3.1 Automated parameter search by simulated annealing

Performance of the simulated annealing algorithm

In this work, we programmed and tested a simulated annealing (SA) algorithm for parameter optimization for realistic neuronal models constrained by experimental data. To our knowledge, this is the first time such an algorithm has been used to build a neuronal model constrained by noisy experimental data. Previous attempts were limited to parameter retrieval from artificial data sets (Vanier & Bower, 1999; Weaver & Wearne, 2006).

To our initial surprise, during test runs the SA algorithm was able to find solutions in parameter space (lower error values upon convergence) than theoretically expected. We attribute this to the low frequency components of the added $1/f$ noise. These could be fitted by the I_h current, in particular when its kinetics was allowed to vary. Because I_h current is not very prominent in L2/3 pyramidal neurons, the conductance densities found for the age-dependent model therefore have to be considered with caution as they might be confounded by the low frequency noise in the model-constraining experimental data.

Among the variants tested, the fully automated SA algorithm performed best as judged from the quality of fit per computational effort. This was particularly prominent for higher noise levels. Of the alternative modes used for our SA algorithm, the variance-dependent annealing schedule (equation 3.10) was the most efficient. While the starting temperature (equation 3.11) was usually chosen very high, equation 3.10 quickly brought it to levels in the regime of the error values themselves (Fig. 3.5C). The main parameter governing the behavior is δ , which for the age-dependent model was set to a value of $\delta = 0.1$ during parameter search, leading to slower annealing close to “thermal”

equilibrium (Das et al., 1990). The expansion causing most problems was the (again) variance-dependent termination criterion, which caused the algorithm to exit prematurely without having found a satisfying solution. This behavior was due to the fact that in equation 3.12 the left side can accidentally become arbitrarily small, although the variance in encountered error values is still high. Therefore we set the governing parameter epsilon to a very small value, thereby disabling this SA algorithm mechanism.

Simulated annealing versus genetic algorithms

An alternative to SA for non-linear optimization in high-dimensional parameter spaces is the class of so-called genetic or evolutionary algorithms (Goldberg, 1989; Eichler-West & Wilcox, 1997; Baldi et al., 1998). These types of algorithm use a fixed-size “population” of parameter sets, of which each “individual” is associated with a certain “fitness” (error function). Each new “generation” is generated by “cross-breeding” (either exchange or averaging parameter sets of fittest individuals) and “mutation” (random changes in single parameter values). Worst individuals become “extinct”. Upon convergence, the differences between individuals become arbitrarily small and the whole population is optimally adapted to its “environment” (error landscape). This algorithm was analyzed by Vanier & Bower (1999) and was found to perform similarly to the SA algorithm. For neuronal models, it has been used in parameter retrieval (Keren et al., 2005) and analysis of parameter landscapes (Achard & De Schutter, 2006).

While in the comparative study by Vanier & Bower (1999), the SA algorithm performed slightly better in medium-sized parameter spaces (up to 20 dimensions), the advantage of genetic algorithms is their inherently parallel structure. Because each individual of a population will be changed once per generation, the fitness of the whole generation can be computed at the same time. In contrast, in the SA algorithm used here only one vertex can be treated at a time, making the algorithm inherently serial. However, new simulation algorithms can distribute the workload of the single simulation run itself onto several computer processors, thereby reducing total computational time considerably. Another strategy would be to divide the parameter space into sections, in each of which a separate SA algorithm is run (parallel search).

3.3.2 Age-dependent L2/3 pyramidal cell models

Comparison to experimental data

With our automated parameter search we aimed at reproducing age-dependent changes of L2/3 pyramidal cell properties as determined by electrophysiological experiments. We focused on the sub-threshold voltage regime determining the cell's basic integrative properties onto which further excitability builds. Furthermore, the number of free parameters is limited compared to the supra-threshold regime and because the simulation results are directly comparable to our experimental data and the conductance values derived thereof.

In our single-compartment models the conductance density g_{KIR} changed in parallel to the total KIR conductance G_{KIR} as derived from the Hodgkin-Huxley (HH) fit to experimental I-V curves (equation 2.7; Fig. 2.27). This result satisfyingly confirms our method proposed in chapter 2.3.3. In addition, we were able to assess the Ih conductance density g_{Ih} , which was not possible with the HH fit method. Consistent with our experimental data g_{Ih} was very small in our model for all ages and maybe even overestimated, as implied by our parameter retrieval test runs (Fig. 3.7A) and the simulated pharmacology (Fig. 3.14). However, Ih was poorly constrained by our experimental data. Here, additional data from voltage-clamp experiments in L2/3 pyramidal cells would be helpful. In addition, we estimated the influence of morphological changes on ion channel densities by normalizing all conductance densities to a membrane capacitance of $C_m = 1 \mu\text{F}/\text{cm}^2$. For g_{Ih} and g_{KIR} this yielded a similar developmental curve, but g_{leak} did not show any developmental changes anymore. Therefore, we conclude, that developmental changes in leak conductance density are completed before p8 and that all changes in R_{in} are attributable to changes in morphology, g_{KIR} and (to lesser degree) g_{Ih} .

The parameter search in models with fully reconstructed morphologies, however, yielded similar developmental changes in C_m compared to the HH-fit presented in chapter 2.3.3. This might have several reasons: (1) morphological reconstructions were biased towards underestimation of dendritic diameters in older cells which might be due to either problems with the optics of the NeuroLucida system itself or to tissue shrinkage of the slice tissue during fixation procedures (Jaeger, 2001); (2) severe increase in spine density might lead to increased surface area relative to dendrite diameter; (3) under-estimation of axial resistance R_{ax} (in these simulations set to $120 \Omega \cdot \text{cm}$) might lead to a decreased electrically effective surface area which had to be corrected for by an increase in C_m . The last point, however, does not seem very likely, as in the full morphology

model based on dual recordings R_{ax} was found to be even higher ($R_{ax} = 191 \Omega\cdot\text{cm}$). Concerning the second point, in other models (Traub et al., 2003; Traub et al., 2006) the spine correction factor was set to a value of around 2, which for mature cells (p45) is well below the value observed in our simulations ($3.6 \pm 0.7 \mu\text{F}/\text{cm}^2$, in this context C_m corresponds to the spine correction factor directly). This discrepancy could mean that the number of proximal spines has been underestimated until now for building neuronal models, and that this number increases during postnatal development.

Comparison with other models

To our knowledge the models presented here are the first age-dependent L2/3 pyramidal cell models. In addition, virtually all other models concentrate on the output with respect to firing pattern, and not on the dendritic integration of synaptic input. Therefore, L2/3 pyramidal cell models previously published are only presented in respect to their firing behavior (Traub et al., 2003; Traub et al., 2006; van Drongelen et al., 2006; van Drongelen et al., 2007), which complicates the comparison of integrative properties between models.

The most detailed L2/3 pyramidal cell model available to date is the model published by Traub et al. (2003). It includes 11 different conductances, most of them responsible for firing behavior and AP waveform. The ion channels governing sub-threshold behavior are the leak conductance, I_h (termed anomalous rectifier), a persistent Na^+ -channel (NaP), and the A-type K^+ -channel (K_A). Because in our analysis NaP did not appear to be present in L2/3 pyramidal cells and K_A was not considered in our model, we can only compare leak and I_h conductances. In the Traub model, g_{leak} was set to $20 \mu\text{S}/\text{cm}^2$ (compared to a g_{leak} of around $150 \mu\text{S}/\text{cm}^2$ in our model). This yielded an input resistance R_{in} of around $70 \text{ M}\Omega$, which expectedly was higher than the value we modeled ($45\text{-}50 \text{ M}\Omega$). I_h was set to a value much higher than in our adult model ($250 \mu\text{S}/\text{cm}^2$). I_h might contribute much more to anomalous rectification in the Traub model than in our model. Therefore, we assume that synaptic integration in that model, especially when included in a network model (Traub et al., 2006), behaves differently from what one would expect experimentally. Further models did not make much effort in modeling sub-threshold behavior (van Drongelen, 2006; van Drongelen, 2007; Rhodes, unpublished) or included very different ion channel sets, making a comparison difficult (e.g. NaP in Segev, unpublished). In summary, we are convinced that a solid understanding of the basic electrical properties of L2/3 neurons is absolutely required for building a realistic model

that is capable of reproducing cellular behavior under in vivo conditions. The models built so far have captured certain aspects but do clearly not provide a comprehensive description of L2/3 pyramidal neurons. In the future all aspects that pass experimental testing may be combined to yield a more complete model.

The ion channel kinetics we used for our model were mainly taken from Day et al. (2006). However, since channel kinetics were made free parameters during automated parameter search, it is interesting to see how the mean kinetics used in our model deviates from the original kinetics. The parameters are listed in Table 3.5. While the shape of the activation curves and the time constant are similar, all curves are shifted to more hyper-polarized values in our model. This might be a property of L2/3 pyramidal neurons compared to the L5/6 pyramidal cells in mouse prefrontal cortex investigated in Day et al. (2006).

	Day et al., 2006	Our model
$A_{lh} / \mu\text{s}^{-1}$	10	11 ± 1
γ_{lh}	0.6	0.51 ± 0.04
q_{lh} / e	4.2	4.9 ± 0.1
$V_{1/2,lh} / \text{mV}$	-90	-97 ± 2
$\tau_{0,lh} / \text{ms}$	1.2	0.6 ± 0.2
$V_{h,KIR} / \text{mV}$	-90	-96 ± 3
$V_{c,KIR} / \text{mV}$	12.1	11.8 ± 1

Table 3.5 Comparison between kinetics in our model and those presented in Day et al. (2006). Values for our model are from single compartment fits for p45. Values for lh from Day et al. were derived from best fit of equation 3.1 to their kinetic curves.

Variability and averaging

One of the advantages of our approach was that besides obtaining average values for an age-dependent L2/3 pyramidal cell model we could also assess the variability in all parameters. This is useful for several reasons: (1) comparison with other models is simplified, as we have an objective measure to decide whether two models incorporating the same ion channels still are similar, even if the exact conductance values differ; (2) when building a network model, cells can be inserted with a certain variability governed by the standard deviation of parameters; (3) variability of ion channel properties are a determining factor in

neuronal networks activity, although the mechanisms governing this variability still remain to be elucidated.

It was shown in several studies (Golowasch et al., 2002; Goldman et al., 2001) that averaging of parameters derived from single cell fits in order to build the “average neuron” often leads to qualitatively different behavior. This was shown in respect to supra-threshold behavior such as bursting, but we cannot exclude that this might also apply to sub-threshold behavior as investigated in this study. Therefore, the averaged age-dependent single-compartment and full-morphology models have to be considered with caution and can only be used with the respective standard errors of each parameter.

3.3.3 UP- and DOWN-states

In this study, we aimed to reproduce the results from Waters & Helmchen (2006) with a mechanistic conductance-based model of L2/3 pyramidal cells. Beyond that, qualitative changes in integrative properties during postnatal development could be elucidated and predictions about cellular behavior at younger ages could be made.

In our adult single compartment model, frequencies of 0.18 Hz for excitatory and 0.03 Hz for inhibitory synapses were sufficient to elicit UP-states of 15 mV amplitude (Table 3.4). These frequencies are only about half the values presented in Waters & Helmchen (2006). This might be due to the fact that their exact values for R_{in} and c_{AR} are only around 50% of the values found in this study, which might be caused by *in vivo* neuromodulation which was not accounted for in this study (e.g. Stanfield et al., 1985). Still, the mean firing rate required for 15 mV UP-states is almost double the rate that was estimated from *in vivo* experiments in neuronal populations of L2/3 (Kerr et al., 2005). This suggests that additional activity is required from other neuronal populations besides L2/3, which might stem from deeper cortical layers (Cowan & Wilson, 1994; Timofeev et al., 2001) or other brain areas (e.g. Battaglia et al., 2004). While R_{in} increased during UP-states in model neurons for p14 or older, in p8 neurons R_{in} decreased during UP-states, although these cells show the highest c_{AR} . The reason was, that part of the effect of AR was “overwritten” by the conductance change due to synaptic activity.

How will developmental changes in intrinsic biophysical properties of L2/3 pyramidal neurons shape activity patterns during UP/DOWN-states? Under the

assumption that synaptic strength and amplitude of UP-states do not change during development, the higher R_{in} of young neurons imply that less synaptic input is required than in matured networks in order to reach the UP-state. This could be due to a less dense (immature) connectivity or a generally reduced network activity. In adult cells, on the other hand, small synaptic inputs will not elevate the membrane potential substantially due to the small R_{in} , but strong synaptic input will be amplified by AR. This might serve as feature detection in respect to network activity. Our prediction thus would be that in young neocortical networks, activity UP-states is even sparser than in adult networks. Only very sparse experimental data is available on the postnatal development of UP/DOWN-states (Johnson & Buonomano, 2007), so that this will need to be elucidated in future *in vivo* experiments.

3.3.4 Expanding the model towards supra-threshold behavior

At the present stage, the model presented here reproduces the sub-threshold behavior of L2/3 pyramidal neurons. The next step necessary to complete the model will be to include mechanisms responsible for generation of regenerative events (APs, dendritic spikes). This will include fast Na^+ - and delayed rectifier K^+ -channels for AP generation itself as well as a variety of Ca^{2+} -, K^+ -, and Ca^{2+} -dependent ion channels for frequency attenuation and exact AP waveform. This will elevate the number of free parameters n well above 20 (Keren et al., 2005; Achard & De Schutter, 2006).

Fitting AP waveform requires an error function different from the squared-error function used in sub-threshold fitting, because one or two APs only make up a very small fraction of all data points due to the low firing frequency of L2/3 pyramidal neurons during a 500-ms trace. Simply using equation 3.12 favours traces without any AP since no AP will lead to a smaller error value than a trace with the right number of APs, but shifted in time. Le Masson & Maex (2001) proposed an error function based on analyzing the trajectory density on a phase plane. Plotting the first derivative of the voltage in time, dV/dt , versus voltage V , APs lead to very characteristic loops within this phase plane. Still, simply comparing curves over the whole stimulus period does not lead to a good description of AP waveform since most of the points describe what happens between APs (which is little indeed). Thus, for test runs with our SA algorithm, a small time window was centred around the first simulated AP and the distance of

the loop to a corresponding experimentally measured loop in phase plane was computed using the squared error:

$$E = \sum_i (V_{sim}^i - V_{target}^i)^2 + c \sum_i (\dot{V}_{sim}^i - \dot{V}_{target}^i)^2 \quad (3.17)$$

Here the dots denote the first derivative in time, dV/dt . The constant c was introduced in order to adjust units and was generally set to 1 ms. The reason for using the phase plane instead of simply the voltage values alone lies in the fact that fast transient behaviour (e. g. the very fast rising phase of the AP) is better characterized than by voltage alone.

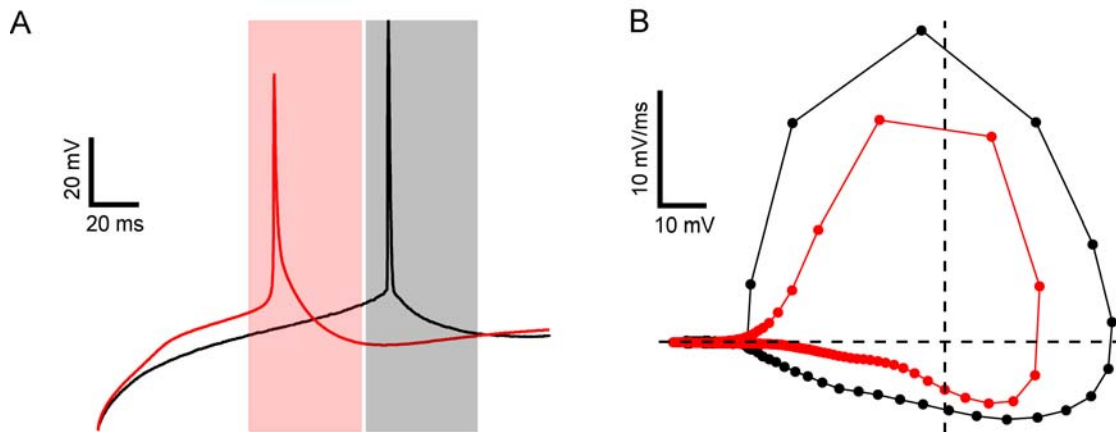


Fig. 3.4 Error function based on phase-plane analysis for reproducing AP firing. **A**, measured (black) versus simulated (red) AP and the respective time-windows over which the error is summed. **B**, phase-plane representation of the two APs shown in **A**. The error is computed using equation 3.13.

Penalty functions

In the case of fitting AP waveform additional penalty functions were introduced to the error function. Obviously, the first step was to penalize the complete absence of APs. Previously this was done by simply setting the error function to a very high value (usually 10^{12}) that represents a potential barrier that cannot be overcome by the simplex at any temperature. Problematic here are several issues, though: If there exist non-connected islands in parameter space where APs are fired, and the complete simplex sets off in one of them it will never reach any other of these islands; secondly, temperature reduction might be difficult to calculate (equation 3.10) since the variance in error function values is either big

(alternation between presence of AP and no AP) or very small (if for example no AP was fired over a complete Metropolis cycle the variance will become 0). Thus, instead of using a fixed value that cannot be overcome, equation 3.17 was replaced by equation 3.14, the squared voltage error was calculated over the complete stimulus period. A second step concerned the exact timing of elicited APs. Here, if an AP was elicited the error calculated in equation 3.17 was multiplied by $(1+|\Delta t_{rel}|)$, where Δt_{rel} denotes the relative error in timing of simulated versus measured AP.

Preliminary results and future challenges

In preliminary simulations for reproducing AP waveform and general firing behavior the following channels were used: a fast Na^+ -channel and a delayed rectifier K^+ -channel for basic AP generation; A-type K^+ -channel for the delay between stimulus onset and first AP; L- and T-type Ca^{2+} -channels; a voltage and Ca^{2+} -dependent K^+ -channel; simple Ca^{2+} -dynamics for exponential Ca^{2+} -extrusion. Different channel kinetics were tested and translated into the formulation used here (equation 3.1; channels taken from Mainen et al., 1995; Traub et al., 2003; Belluzzi & Sacchi, 1991; Rhodes, unpublished; Poirazi et al., 2003). Resulting kinetic parameters in equation 3.1 could vary strongly, depending on which channel was used. This led us to leaving free kinetic parameters mainly unconstrained.

Finding parameter sets with an error function following equation 3.17 which reproduced AP waveform was extremely difficult in single compartment models. In most cases, the SA algorithm was satisfied with the model generating a small “bump” where the actual AP should have happened. In cases where APs were generated, AP waveform was far from optimal in comparison to experimental data. The main problem seemed to be that free kinetic parameters led to too many degrees of freedom so that the algorithm cooled down before encountering a near-optimal solution. Therefore, we kept the kinetics fixed and varied only the conductance densities. This, too, did not result in satisfying AP waveforms. In addition, some of the kinetics (Traub et al, 2003) were to “nervous”, easily resulting in extremely high firing frequencies, while others were to slow (Mainen et al., 1995).

One of the main problems with AP waveform in L2/3 pyramidal cells is the relatively high threshold of around -35 mV. Since simple shifting of kinetics to more depolarized potentials did not result in the required behavior, we switched to using a full-morphology model with a generic axon (following Mainen &

Sejnowski, 1995), in which the AP was generated within the first node of Ranvier and the kinetics of the fast Na⁺-channel and the delayed rectifier K⁺-channel were shifted to more depolarized potentials. These measures had little effect on the AP threshold, however.

The challenges for future simulations of L2/3 pyramidal cells which also display the experimentally observed supra-threshold behavior are the following: (1) definition of an error function that captures AP waveform as well as general firing behavior; combination of an inter-spike interval (ISI) based function with the phase-plane base function presented above appear promising; (2) step-wise expanding of the set of channels included in the model, as not all channels determine e.g. AP waveform; (3) developing of methods for thoroughly testing which kinetic parameters of which channels the supra-threshold behavior is sensitive to, i.e. a better definition of error landscape (Achard & De Schutter., 2006)

4 Conclusion and Outlook

Anomalous rectification

The main finding in this study is that the anomalous rectification (AR) observed in pyramidal neurons of cortical L2/3 is caused by an inward-rectifier potassium (KIR) current, the expression of which increases during the first six weeks of postnatal development. Based on numerical simulations we conclude that AR counterbalances the progressive reduction in input resistance R_{in} in these cells during the postnatal development. Indeed, AR seems to be an abundant theme in the mammalian CNS and has been reported for motoneurons of the brainstem and the spinal chord (Nelson & Frank, 1967; Chandler et al., 1994; Bayliss et al., 1994; Heckman, 2003), cerebellar Purkinje cells (Crepel & Penit-Soria, 1986; Li et al., 1993), hippocampal pyramidal neurons (Seeger & Alzheimer, 2001), cortical interneurons (Gorelova et al., 2002) and pyramidal cells different from those in L2/3 (Stafstrom et al., 1982; Stafstrom et al., 1985). The reason for this abundance could be that AR provides a mechanism to counterbalance the conductance increase that is caused by strong synaptic activation and that renders each additional synaptic input less effective. The precise consequences of this mechanism for synaptic integration under *in vivo* conditions in the neocortex remain to be elucidated in further experiments. In addition, it is unclear which role modulatory effects on AR, e.g. via cholinergic or dopaminergic ascending systems, might play in shaping the response of L2/3 pyramidal cells to synaptic activity *in vivo*.

Developmental changes

During postnatal development, L2/3 pyramidal neurons were found to change their electrophysiological properties until 4-5 weeks after birth, while morphological development was complete already 2 weeks after birth. The most rapid changes in electrophysiological properties took place within the second week after birth, while later changes might rather represent fine tuning of the cell's responsiveness. This period around p14 has previously been found to be a critical period in L2/3 of somato-sensory cortex of rats (Lendvai et al., 2000; Stern et al., 2001; Maravall et al., 2004a). Therefore, in future *in vivo* experiments on the interplay of the effects of single-cell properties and network activity at different developmental stages, special attention has to be turned on this period. One would expect the most pronounced changes in network responses to stimuli as well as spontaneous activity in these cortical networks during this period

since the receptive field as well as the responsiveness to synaptic input change most then. With respect to morphologies, it would also be interesting to assess how the volume covered by axons of L2/3 pyramidal neurons changes, as this will constrain possible network architectures that can be tested for in simulation. Also, estimating the change in numbers of pre- and post-synaptic terminals will be interesting as this (together with the network activity) will further constrain the spatio-temporal pattern of synaptic input.

Modeling

The simulated annealing (SA) algorithm to our knowledge was here for the first time applied to noisy data in order to build a valid model. In our opinion, this approach was successful, as parameter sets displayed a certain stability from cell to cell, and all values are within reasonable physiological ranges. However, a major problem of this algorithm is its intrinsic serial computing, which prevents efficient application on multi-processor computers. Two strategies to overcome this limitation seem reasonable: (1) intelligent dividing of parameter space into sub-spaces, in each of which an independent SA algorithm is run; or (2) parallelizing the numerical simulation itself. As several parallel simulation programs will become available in the near future, the second strategy seems promising. Also, in our experience the SA algorithm itself was never the “bottleneck” for computational time needed for convergence. As we showed in this work, automated parameter search can be quite rewarding when single-cell, single-experiment data are available. Basically, the parameter sets obtained could be directly implemented into a model network such as a single column.

Outlook

The main question that arises from the experiments presented here is how developmental changes in biophysical properties of single L2/3 pyramidal neurons influence or are accompanied by changes in network properties of the intact cortical L2/3. In particular, how spontaneous and stimulus-evoked activity does developmentally evolve in these networks has not been understood nor even systematically investigated *in vivo* yet. In order to approach this problem, again a dual experimental and modeling approach will be needed.

New experimental techniques allow to image populations of neurons with single-cell and single-AP resolution in the intact brain by combining bulk-loading of cortical tissue with fluorescent Ca^{2+} -sensitive dyes and subsequent imaging

with two-photon excitation (Stosiek et al., 2003; Nimmerjahn et al., 2004; Kerr et al., 2005; Gobel et al., 2007). These techniques will enable us to measure the spread of neural activity during spontaneous UP-states and during stimulus-evoked network responses for animals of different developmental stages. However, experimental procedures have to be developed for young animals, as several problems will arise here with anesthesia and stability during recordings. Optical imaging will be accompanied by simultaneous electrophysiological experiments on the single-cell level (whole-cell patch-clamp) and the network level (electro-corticogram, ECoG). Reconstruction of single-cell dendritic and axonal trees will allow estimation of the network's connectivity and topology at different ages.

Thus in the future, new experimental data will be used to constrain network simulations of L2/3 in order to elucidate the basic principles of organization and function of this layer and its interaction with other layers. To this end, age-dependent single cell properties have to be transferred to simpler models, e.g. spike-response models (SRM; see e.g. Gerstner & Kistler, 2002), which reproduce the features of L2/3 pyramidal cells without the same need for computation power as complicated conductance-based models such as those presented in this study (Kistler et al., 1997). These simplified models then can be used to build age-dependent network models, elucidating interactions between developmental changes in synaptic inputs, connectivity, network topology and biophysical properties of single cells.

5 References

- Aarts, EHL, van Laarhoven, PJM (1985). Statistical cooling: a general approach to combinatorial optimization problems. *Philips J Res* 40, 193-226
- Achard, P, De Schutter, E (2006). Complex parameter landscape for a complex neuron model. *PLoS Comp Biol* 2(7), 794-804
- Adam, G, Lauger, P, Stark, G (1995). *Physikalische Chemie und Biophysik* (3rd ed.), Springer, Berlin
- Ahissar, E, Kleinfeld, D (2003). Closed-loop neuronal computations: focus on vibrissa somatosensation in rat. *Cereb Cortex* 13(1), 53-62
- Ali, AB, Rossier, J, Staiger, JF, Audinat, E (2001). Kainate receptors regulate unitary IPSCs elicited in pyramidal cells by fast-spiking interneurons in the neocortex. *J Neurosci* 21, 2992-2999
- Alonso, A, Klink, R (1993). Differential electroresponsiveness of stellate and pyramidal-like cells of medial entorhinal cortex layer II. *J Neurophysiol* 70(1), 128-143
- Ashe, J, Ugurbil, K (1994). Functional imaging of the motor system. *Curr Opin Neurobiol* 4(6), 832-839
- Bajic, D, Koike, M, Albsoul-Younes, AM, Nakajima, S, Nakajima, Y (2002). Two different inward rectifier K⁺ channels are effectors for transmitter-induced slow excitation in brain neurons. *Proc Natl Acad Sci USA* 99(22), 14494-14499
- Baldi, PF, Vanier, MC, Bower, JM (1998). On the use of Bayesian methods for evaluating compartmental neural models. *J Comp Neurosci* 5, 285-314
- Barrett, JN (1975). Motoneuron dendrites: role in synaptic integration. *Fed Proc* 34, 1398-1407
- Battaglia, FP, Sutherland, GR, McNaughton, BL (2004). Hippocampal sharp wave bursts coincide with neocortical "up-state" transitions. *Learn Mem* 11(6), 697-704
- Bayliss, DA, Viana, F, Bellingham, MC, Berger, AJ (1994). Characteristics and postnatal development of a hyperpolarization-activated inward current in rat hypoglossal motoneurons *in vitro*. *J Neurophysiol* 71(1), 119-128

5 References

- Beaulieu, C (1993). Numerical data on neocortical neurons in adult rat, with special reference to the GABA population. *Brain Research* 609, 284-292
- Bellman, RE (1957). Dynamic programming. Princeton University Press, Princeton, NJ
- Belluzzi, O, Sacchi, O (1991). A five-conductance model of the action potential in the rat sympathetic neurone. *Prog Biophys molec Biol* 55, 1-30
- Benndorf, K (1995). Low-noise recording. In: Sakmann, B, Neher, E (ed.): Single-channel recording (2nd ed.), Plenum Press, New York
- Berger, T, Larkum, ME, Lüscher, HR (2001). High I(h) channel density in the distal apical dendrite of layer V pyramidal cells increases bidirectional attenuation of EPSPs. *J Neurophysiol* 85(2), 855-868
- Berger, T, Senn, W, Lüscher, HR (2003). Hyperpolarization-activated current I_h disconnects somatic and dendritic spike initiation zones in layer V pyramidal neurons. *J Neurophysiol* 90, 2428-2437
- Bernander, Ö, Douglas, R, Martin, KAC, Koch, C (1991). Synaptic background activity influences spatiotemporal integration in single pyramidal cells. *Proc Natl Acad Sci USA* 88, 11569-11573
- Bhalla, US, Bower, JM (1993). Exploring parameter space in detailed single neuron models: simulations of the mitral and granule cells of the olfactory bulb. *J Neurophysiol* 69(6), 1948-1965
- Bi, GQ, Poo, MM (1998). Synaptic modifications in cultured hippocampal neurons: dependence on spike timing, synaptic strength, and postsynaptic cell type. *J Neurosci* 18(24), 10464-10472
- Bichet, D, Hass, FA, Jan, LY (2003). Merging functional studies with structures of inward-rectifier K⁺ channels. *Nature Reviews* 4, 957-967
- Blanton, MG, Lo Turco, JJ, Kriegstein, AR (1989). Whole cell recording from neurons in slices of reptilian and mammalian cerebral cortex. *J Neurosci Methods* 30, 203-210
- Blatz, AL, Magleby, KL (1987). Calcium-activated potassium channels. *Trends Neurosci* 10, 463-467
- Borg-Graham, L (1999). Interpretations of data and mechanisms for hippocampal pyramidal cell models. In: Jones, E, Ulinski, P, Peters, A (ed.): *Cerebral Cortex*. Plenum Publishing Corporation, New York

- BoSmith, RE, Briggs, I, Sturgess, NC (1993). Inhibitory actions of ZENECA ZD7288 on whole cell hyperpolarization activated inward current (I_h) in guinea-pig dissociated sinoatrial node cells. *Br J Pharmacol* 110(1), 343-349
- Brecht, M, Roth, A, Sakmann, B (2003). Dynamic receptive fields of reconstructed pyramidal cells in layers 3 and 2 of rat somatosensory barrel cortex. *J Physiol* 553(1), 243-265
- Brodmann, K (1909). Vergleichende Lokalisationslehre der Grosshirnrinde. Barth, Leipzig
- Brown, D (1988). M-current: an update. *Trends Neurosci* 11, 294-299
- Bruzzone, R, Dermietzel, R (2006). Structure and function of gap junctions in the developing brain. *Cell Tissue Res* 326, 239-248
- Bureau, I, von Saint Paul, F, Svoboda, K (2006). Interdigitated paralemniscal and lemniscal pathways in the mouse barrel cortex. *PLoS Biol* 4(12), e382
- Buzsaki, G, Geisler, C, Henze, DA, Wang, XJ (2003). Interneuron diversity series: circuit complexity and axon wiring economy of cortical interneurons. *Trends Neurosci* 27(4), 186-193
- Cardoso, MF, Salcedo, RL, de Azevedo, SF (1996). The simplex-simulated annealing approach to continuous non-linear optimization. *Comp Chem Eng* 20(9), 1065-1080
- Catterall, WA (1990). Cellular and molecular biology of voltage-gated sodium channels. *Physiol Rev* 72, S15-S48
- Chagnac-Amitai, Y, Luhmann, HJ, Prince, DA (1990). Burst generating and regular spiking layer 5 pyramidal neurons of rat neocortex have different morphological features. *J Comp Neurol* 296, 598-613
- Chandler, WK, Meves, H (1970). Rate constants associated with changes in sodium conductance in axons perfused with sodium fluoride. *J Physiol (Lond)* 211, 679-705
- Chandler, SH, Hsiao, CF, Inoue, T, Goldberg, LJ (1994). Electrophysiological properties of guinea pig trigeminal motoneurons recorded *in vitro*. *J Neurophysiol* 71(1), 129-145
- Cherubini, E, Gaiarsa, JL, Ben-Ari, Y (1991). GABA: an excitatory transmitter in early postnatal life. *Trends Neurosci* 14(12), 515-519

5 References

- Coetzee, WA, Amarillo, Y, Chiu, J, Chow, A, Lau, D, McCormack, T, Moreno, H, Nadal, MS, Ozaita, A, Pountney, D, Saganich, M, Vega-Saenz de Miera, E, Rudy, B (1999). Molecular diversity of K⁺ channels. *Ann NY Acad Sci* 868, 233-285
- Cohen, SD, Hindmarsh, AC (1996). CVODE, a stiff/nonstiff ODE solver in C. *Comp Phys* 10(2), 138-143
- Cohen-Tannoudji, M, Babinet, C, Wassef, M (1994). Early determination of a mouse somatosensory cortex marker. *Nature* 368, 460-463
- Connor, JA, Stevens, JF (1971). Voltage clamp studies of a transient outward membrane current in gastropod neural somata. *J Physiol (Lond)* 213, 21-30
- Connors, BW, Gutnick, MJ, Prince, DA (1982). Electrophysiological properties of neocortical neurons *in vitro*. *J Neurophysiol* 48(6), 1302-1320
- Connors, BW, Prince, DA (1982). Effects of local anesthetic QX-314 on the membrane properties of hippocampal pyramidal neurons. *J Pharmacol Exp Ther* 220, 476-481
- Connors, BW, Benardo, LS, Prince, DA (1983). Coupling between neurons of the developing rat neocortex. *J Neurosci* 3, 773-782
- Cowan, RL, Wilson, CJ (1994). Spontaneous firing patterns and axonal projections of single corticostriatal neurons in the rat medial agranular cortex. *J Neurophysiol* 71(1), 17-32
- Crepel, F, Penit-Soria, J (1986). Inward rectification and low threshold calcium conductance in rat cerebellar Purkinje cells. An *in vitro* study. *J Physiol* 372, 1-23
- Das, H, Cummings, PT, Le Van, MD (1990). Scheduling of serial multiproduct batch processes via simulated annealing. *Comp Chem Eng* 14(12), 1351-1362
- Day, M, Carr, DB, Ulrich, S, Ilijic, E, Tkatch, T, Surmeier, DJ (2005). Dendritic excitability of mouse frontal cortex pyramidal neurons is shaped by the interaction among HCN, Kir2, and K_{leak} channels. *J Neurosci* 25(38), 8776-8787
- Debanne, D, Gähwiler, BH, Thompson, SM (1998). Long-term synaptic plasticity between pairs of individual CA3 pyramidal cells in rat hippocampal slice cultures. *J Physiol (Lond)* 507, 237-247

- DeFelipe, J, Farinas, I (1992). The pyramidal neuron of the cerebral cortex: morphological and chemical characteristics of the synaptic input. *Prog Neurobiol* 39, 563-607
- De Kock, CPJ, Bruno, RM, Sakmann, B (2007). Layer and cell type specific suprathreshold stimulus representation in primary somatosensory cortex. *J Physiol* 581(1), 139-145
- Destexhe, A, Rudolph, M, Fellous, JM, Sejnowski, TJ (2001). Fluctuating synaptic conductances recreate in vivo-like activity in neocortical neurons. *Neurosci* 107(1), 13-24
- Destexhe, A, Rudolph, M, Pare, D (2003). The high conductance state of neocortical neurons in vivo. *Nat Rev Neurosci* 4(9), 739-751
- DiFrancesco, D (1981). A study of the ionic nature of the pace-maker current in calf Purkinje fibres. *J Physiol (Lond)* 314, 377-393
- Dutta, P, Horn, PM (1981). Low frequency fluctuations in solids: 1/f noise. *Rev Mod Phys* 53, 497-516
- Edmondson, JC, Hatten, ME (1987). Glial-guided granule neuron migration *in vitro*: a high-resolution time-lapse video microscopic study. *J Neurosci* 7, 1928-1934
- Edwards, FA, Konnerth, A, Sakmann, B, Takahashi, T (1989). A thin slice preparation for patch clamp recordings from neurons of the mammalian central nervous system. *Pflugers Arch* 414, 600-612
- Eichler-West, R, Wilcox, G (1997). Robust parameter selection for compartmental models of neurons using evolutionary algorithms. In: Bower, JM (ed): *Computational neuroscience: trends in research 1997*. Plenum Publishing, New York
- Erzurumlu, RS, Jhaveri, S (1990). Thalamic axons confer a blueprint of the sensory periphery onto developing rat somatosensory cortex. *Dev Brain Res* 56, 229-234
- Feldmeyer, D, Lubke, J, Silver, RA, Sakmann, B (2002). Synaptic connections between layer 4 spiny neurone-layer 2/3 pyramidal cell pairs in juvenile rat barrel cortex: physiology and anatomy of interlaminar signaling within a cortical column. *J Physiol* 538(3), 803-822
- Feldmeyer, D, Lubke, J, Sakmann, B (2006). Efficacy and connectivity of intracolumnar pairs of layer 2/3 pyramidal cells in the barrel cortex of juvenile rats. *J Physiol* 575(2), 583-602

5 References

- Fozzard, HA, Hanck, DA (1996). Structure and function of voltage-dependent sodium channels: comparison of brain II and cardiac isoforms. *Physiol Rev* 76(3), 887-926
- Fukuda, A, Prince, DA (1992). Postnatal development of electrogenic sodium pump activity in rat hippocampal pyramidal neurons. *Brain Res Dev Brain Res* 65(1), 101-114
- Garcia, ML, Hanner, M, Knaus, HG, Koch, R, Schmalhofer, W, Slaughter, RS, Kaczorowski, GJ (1997). Pharmacology of potassium channels. *Adv Pharmacol* 39, 425-471
- Gerstner, W, Kistler, W (2002). Spiking Neuron Models. Cambridge University Press, Cambridge, UK
- Glauber, RJ (1963). Time-dependent statistics of the Ising model. *J Math Phys* 4, 294
- Gobel, W, Kampa, BM, Helmchen, F (2007). Imaging cellular network dynamics in three dimensions using fast 3D laser scanning. *Nat Methods* 4(1), 73-79
- Goldberg, DE (1989). Genetic algorithms in search, optimization, and machine learning. Addison-Wesley, Reading, MA
- Goldin, AL (2001). Resurgence of sodium channel research. *Annu Rev Physiol* 63, 871-894
- Gorelova, N, Seamans, JK, Yang, CR (2002). Mechanisms of dopamine activation of fast-spiking interneurons that exert inhibition in rat prefrontal cortex. *J Neurophysiol* 88(6), 3150-3166
- Hagiwara, S, Kusano, K, Saito, N (1961). Membrane changes of *Onchidium* nerve cell in potassium-rich media. *J Physiol (Lond)* 155, 470-489
- Hamill, OP, Marty, A, Neher, E, Sakmann, B, Sigworth, FJ (1981). Improved patch-clamp techniques for high-resolution current recording from cells and cell-free membrane patches. *Pflugers Arch* 391, 85-100
- Häusser, M, Stuart, GJ, Racca, C, Sakmann, B (1995). Axonal initiation and active dendritic propagation of action potentials in *substantia nigra* neurons. *Neuron* 15(3), 637-647
- Häusser, M, Roth, A (1997). Estimating the time course of the excitatory synaptic conductance in neocortical pyramidal cells using a novel voltage jump method. *J Neurosci* 17, 7606-7625

- Heckman, CJ (2003). Active conductances in motoneuron dendrites enhance movement capabilities. *Exerc Sport Sci Rev* 31(2), 96-101
- Hille, B (2001). Ion channels of excitable membranes (3rd ed.). Sinauer Associates, Inc., Sunderland, Massachusetts
- Hindmarsh, AD, Brown, PN, Grant, KE, Lee, SL, Serban, R, Shumaker, DE, Woodward, CS (2005). SUNDIALS: Suite of nonlinear and differential/algebraic equation solvers. *ACM Transactions on Mathematical Software* 31(3), 363-396
- Hines, ML (1984). Efficient computation of branched nerve equations. *Int J Bio-Med Comp* 15, 69-76
- Hines, ML, Carnevale, NT (1997). The NEURON simulation environment. *Neural Comp* 9, 1179-1209
- Hines, ML, Carnevale, NT (2000). Expanding NEURONS's repertoire of mechanisms with NMODL. *Neural Comp* 12, 839-851
- Hirrlinger, J, Hülsmann S, Kirchhoff, F (2004). Astroglial processes show spontaneous motility at active synaptic terminals *in situ*. *Eur J Neurosci* 20(8), 2235-2239
- Hodgkin, AL, Huxley, AF (1952a). Currents carried by sodium and potassium ions through the membrane of the giant axon of *Loligo*. *J Physiol* 116, 449-472
- Hodgkin, AL, Huxley, AF (1952b). The components of membrane conductance in the giant axon of *Loligo*. *J Physiol* 116, 473-496
- Hodgkin, AL, Huxley, AF (1952c). The dual effect of membrane potential on sodium conductance in the giant axon of *Loligo*. *J Physiol* 116, 497-506
- Hodgkin, AL, Huxley, AF (1952d). A quantitative description of membrane current and its application to conduction and excitation in nerve. *J Physiol* 117, 500-544
- Hubel, DH, Wiesel, TN (1962). Receptive fields, binocular interaction and functional architecture in the cat's visual cortex. *J Physiol* 148, 106-154
- Hubel, DH, Wiesel, TN (1970). The period of susceptibility to the physiological effects of unilateral eye closure. *J Physiol* 206, 419-436
- Hwa, GGC, Avoli, M (1991). Hyperpolarizing inward rectification in rat neocortical neurons located in the superficial layers. *Neuroscience Letters* 124, 65-68

5 References

- Jaeger, D (2001). Accurate reconstruction of neuronal morphology. In: De Schutter, E (ed.). Computational neuroscience: realistic modeling for experimentalists. CRC Press, Boca Raton
- Jentsch, TJ (2000). Neuronal KCNQ potassium channels: physiology and role in diseases. *Nat Rev Neurosci* 1, 21-30
- Johnson, HA, Buonomano, DV (2007). Development and plasticity of spontaneous activity and up states in cortical organotypic slices. *J Neurosci* 27(22), 5915-5925
- Johnston, D, Wu, SM (1997). Foundations of cellular neurophysiology. MIT Press, Cambridge, Massachusetts
- Kaplan, MR, Cho, MH, Ullian, EM, Isom, LL, Levinson, SR, Barres, BA (2001). Differential control of clustering of the sodium channels Na(v)1.2 and Na(v)1.6 at developing CNS nodes of Ranvier. *Neuron* 30(1), 105-119
- Karten, HJ, Shimazu, T (1989). The origins of neocortex: connections and lamination as distinct events in evolution. *J Cogn Neurosci* 1, 291-301
- Katz, B (1949). Les constantes electriques de la membrane du muscle. *Arch Sci Physiol* 3, 285-299
- Katz, LC, Crowley, JC (2002). Development of cortical circuits: lessons from ocular dominance columns. *Nat Rev Neurosci* 3(1), 34-42
- Kerr, JN, Greenberg, D, Helmchen, F (2005). Imaging input and output of neocortical networks *in vivo*. *Proc Natl Acad Sci USA* 102(39), 14063-14068
- Kirkpatrick, S, Gelatt, CK, Vecchi, MP (1983). Optimization by simulated annealing. *Science* 220(4598), 671-680
- Kirkpatrick, S (1984). Optimization by simulated annealing: quantitative studies. *J Stat Phys* 34(5/6), 975-986
- Kistler, WM, Gerstner, W, van Hemmen, JL (1997). Reduction of Hodgkin-Huxley equations to a single-variable threshold model. *Neural Comp* 9, 1015-1045
- Kitano, K, Fukai, T (2007). Variability versus synchronicity of neuronal activity in local cortical network models with different wiring topologies. *J Comput Neurosci* (Epub ahead of print)
- Klink, R, Alonso, A (1993). Ionic mechanisms for the subthreshold oscillations and differential electroresponsiveness of medial entorhinal cortex layer II. *J Neurophysiol* 70(1), 144-157

- Koch, C (1999). Biophysics of computation. Information processing in single neurons. Oxford University Press, Oxford
- Koch, C, Douglas, R, Wehrmeier, U (1990). Visibility of synaptically induced conductance changes: Theory and simulations of anatomically characterized cortical pyramidal cells. *J Neurosci* 10, 1728-1744
- Koch, C, Poggio, T, Torre, V (1982). Retinal ganglion cells: A functional interpretation of dendritic morphology. *Phil Trans Roy Soc B* 298, 227-264
- Kole, MH, Hallermann, S, Stuart, GJ (2006). Single Ih channels in pyramidal neuron dendrites: properties, distribution, and impact on action potential output. *J Neurosci* 26(6), 1677-1687
- Kuo, A, Gulbis, JM, Antcliff, JF, Rahman, T, Lowe, ED, Zimmer, J, Cuthbertson, J, Ashcroft, FM, Ezaki, T, Doyle, DA (2003). Crystal structure of the potassium channel KirBac1.1 in the closed state. *Science* 300, 1922-1926
- Lampl, I, Schwindt, P, Crill, W (1998). Reduction of cortical pyramidal neuron excitability by the action of phenytoin on persistent Na⁺ current. *J Pharmacol Exp Ther* 284(1), 228-237
- Lampl, I, Reichova, I, Ferster, D (1999). Synchronous membrane potential fluctuations in neurons of the cat visual cortex. *Neuron* 22, 361-374
- Larkman, AU, Mason, A (1990). Correlations between morphology and electrophysiology of pyramidal neurons in slices of rat visual cortex. I. Establishment of cell classes. *J Neurosci* 10(5), 1407-1414
- Larkman, AU (1991a). Dendritic morphology of pyramidal neurones of the visual cortex of the rat: I. branching pattern. *J Comp Neurol* 306, 307-319
- Larkman, AU (1991b). Dendritic morphology of pyramidal neurones of the visual cortex of the rat: II. parameter correlations. *J Comp Neurol* 306, 320-331
- Larkman, AU (1991c) Dendritic morphology of pyramidal neurones of the visual cortex of the rat: III. spine distributions. *J Comp Neurol* 306, 332-343
- Larkum, ME, Zhu, JJ, Sakmann, B (1999). A new cellular mechanism for coupling inputs arriving at different cortical layers. *Nature* 398, 338-341
- Larkum, ME, Zhu, JJ, Sakmann, B (2001). Dendritic mechanisms underlying the coupling of the dendritic with the axonal action potential initiation zone of adult rat layer 5 pyramidal neurons. *J Physiol* 533(2), 447-466

5 References

- Larkum, ME, Watanabe, S, Nakamura, T, Lasser-Ross, N, Ross, WN (2003). Synaptically activated Ca²⁺ waves in layer 2/3 and layer 5 rat neocortical pyramidal neurons. *J Physiol* 549(2), 471-488
- Larkum, ME, Waters, J, Sakmann, B, Helmchen, F (2007). Dendritic spikes in apical dendrites of neocortical layer 2/3 pyramidal neurons. Submitted
- Lee, AK, Manns, ID, Sakmann, B, Brecht, M (2006). Whole-cell recordings in freely moving rats. *Neuron* 51(4), 399-407
- Le Masson, G, Maex, R (2001). Introduction to equation solving and parameter fitting. In: De Schutter, E (ed.). *Computational neuroscience: realistic modeling for experimentalists*. CRC Press, Boca Raton
- Lendvai, B, Stern, EA, Chen, B, Svoboda, K (2000). Experience-dependent plasticity of dendritic spines in the developing rat barrel cortex *in vivo*. *Nature* 404(6780), 876-881
- Li, SJ, Wang, Y, Strahlendorf, HK, Strahlendorf, JC (1993). Serotonin alters an inwardly rectifying current (I_h) in rat cerebellar Purkinje cells under voltage clamp. *Brain Res* 617(1), 87-95
- Llinas, RR (1988). The intrinsic electrophysiological properties of mammalian neurons: insights into central nervous system function. *Science* 242, 1654-1664
- Lopatin, AN, Makhina, EN, Nichols, CG (1994). Potassium channel block by cytoplasmic polyamines as the mechanism of intrinsic rectification. *Nature* 372, 366-369
- Lubke, J, Roth, A, Feldmeyer, D, Sakmann, B (2003). Morphometric analysis of the columnar innervation domain of neurons connecting layer 4 and layer 2/3 of juvenile rat barrel cortex. *Cerebral Cortex* 13(10), 1051-1063
- Lüthi, A, Bal, T, McCormick, DA (1998a). Periodicity of thalamic spindle waves is abolished by ZD7288, a blocker of I_h. *J Neurophysiol* 79(6), 3284-3289
- Lüthi, A, McCormick, DA (1998b). H-current: properties of a neuronal and network pace-maker. *Neuron* 21, 9-12
- Maccaferri, G, Mangoni, M, Lazzari, A, DiFrancesco, D (1993). Properties of the hyperpolarization-activated current in rat hippocampal CA1 neurons. *J Neurophysiol* 69, 2129-2136

- Magee, JC (1998). Dendritic hyperpolarization-activated currents modify the integrative properties of hippocampal CA1 pyramidal neurons. *J Neurosci* 18(19), 7613-7624
- Magee, JC (1999). Dendritic Ih normalizes temporal summation in hippocampal CA1 neurons. *Nat Neurosci* 2, 508-514
- Mainen, ZF, Joerges, J, Huguenard, JR, Sejnowski, TJ (1995). A model of spike initiation in neocortical pyramidal neurons. *Neuron* 15, 1427-1439
- Maravall, M, Koh, IY, Lindquist, WB, Svoboda, K (2004a). Experience-dependent changes in basal dendritic branching of layer 2/3 pyramidal neurons during a critical period for developmental plasticity in rat barrel cortex. *Cereb Cortex* 14(6), 655-664
- Maravall, M, Stern, EA, Svoboda, K (2004b). Development of intrinsic properties and excitability of layer 2/3 pyramidal neurons during a critical period for sensory maps in rat barrel cortex. *J Neurophysiol* 92(1), 144-156
- Marban, E, Yamagashi, T, Tomaselli, GF (1998). Structure and function of voltage-gated sodium channels. *J Physiol* 508(3), 647-657
- Mariani, J (1983). Elimination of synapses during the development of the central nervous system. *Prog Brain Res* 58, 383-392
- Marquardt, DW (1963). An algorithm for least-squares estimation of nonlinear parameters. *J Soc Ind Appl Math* 11, 431-441
- Matsuda, H, Saigusa, A, Irisawa, H (1987). Ohmic conductance through the inwardly rectifying K⁺ channel and blocking by internal Mg²⁺. *Nature* 325, 156-159
- McCormick, DA, Connors, BW, Lighthall, JW, Prince, DA (1985). Comparative electrophysiology of pyramidal and sparsely spiny stellate neurons of the neocortex. *J Neurophysiol* 54, 782-806
- McCormick, DA, Prince, DA (1987). Post-natal development of electrophysiological properties of rat cerebral cortical pyramidal neurones. *J Physiol* 393, 743-762
- McCormick, DA, Pape, HC (1990). Properties of a hyperpolarization-activated cation current and its role in rhythmic oscillation in thalamic relay neurones. *J Physiol (Lond)* 431, 291-318
- Meech, RW (1974). The sensitivity of *Helix aspersa* neurones to injected calcium ions. *J Physiol (Lond)* 237, 259-277

5 References

- Metropolis, N, Rosenbluth, AW, Rosenbluth, MN, Teller, AH (1953). Equation of state calculations by fast computing machines. *J Chem Phys* 21(6), 1087-1092
- Mountcastle, VB (1957). Modality and topographic properties of single neurons of cat's somatosensory cortex. *J Neurophysiol* 20, 403-434
- Nathan, T, Jensen, MS, Lambert, JDC (1990). The slow inhibitory postsynaptic potential in rat hippocampal CA1 neurones is blocked by intracellular injection of QX-314. *Neurosci Lett* 110, 309-314
- Neher, E, Sakmann, B (1976). Single-channel currents recorded from membrane of denervated frog muscle fibres. *Nature* 260, 799-802
- Nelder, JA, Mead, R (1965). A simplex method for function minimization. *Comput J* 7, 308-313
- Nelson, PG, Frank, K (1967). Anomalous rectification in cat spinal motoneurons and effect of polarizing currents on excitatory postsynaptic potential. *J Neurophysiol* 30(5), 1097-1113
- Nilius, B, Hess, P, Lansman, JB, Tsien, RW (1985). A novel type of cardiac calcium channel in ventricular cells. *Nature (Lond)* 316, 443-446
- Nimmerjahn, A, Kirchhoff, F, Kerr, JND, Helmchen, F (2004). Sulforhodamine 101 as a specific marker of astroglia in the neocortex *in vivo*. *Nat Methods* 1, 31-37
- Nimmerjahn, A, Kirchhoff, F, Helmchen, F (2005). Resting microglial cells are highly dynamic surveillants of brain parenchyma *in vivo*. *Science* 308(5726), 1314-1318
- O'Leary, DDM (1992). Development of connectional diversity and specificity in the mammalian brain by the pruning of collateral projections. *Curr Opin Neurobiol* 2, 70-77
- Pare, D, Shink, E, Gaudreau, H, Destexhe, A, Lang, EJ (1998). Impact of spontaneous synaptic activity on the resting properties of cat neocortical neurons *in vivo*. *Exp Brain Res* 69, 489-496
- Penfield, W, Rasmussen, T (1950). The cerebral cortex of man. A clinical study of localization of function. The Macmillan Comp., New York
- Peters, A (1987). Number of neurons and synapses in primary visual cortex. In: Peters, A, Jones, EG (eds.). *Cerebral Cortex Vol. 3: Visual cortex*. Plenum Press, New York

- Petersen, CCH, Grinvald, A, Sakmann, B (2003a). Spatiotemporal dynamics of sensory responses in layer 2/3 of rat barrel cortex measured *in vivo* by voltage-sensitive dye imaging combined with whole-cell voltage recordings and neuron reconstructions. *J Neurosci* 23(3), 1298-1309
- Petersen, CCH, Hahn, TTG, Mehta, M, Grinvald, A, Sakmann, B (2003b). Interaction of sensory responses with spontaneous depolarization in layer 2/3 barrel cortex. *Proc Natl Acad Sci USA* 100, 13638-13643
- Poirazi, P, Brannon, T, Mel, BW (2003). Arithmetic of subthreshold synaptic summation in a model CA1 pyramidal cell. *Neuron* 37, 977-987
- Press, WH, Teukolsky, SA (1991). Simulated annealing optimization over continuous spaces. *Comput Phys* 5(4), 426-429
- Press, WH, Teukolsky, SA, Vetterling, WT, Flannery, BP (1992). Numerical recipes in C (2nd ed.). Cambridge University Press, New York
- Prinz, AA, Billimoria, CP, Marder, E (2003). Alternative to hand-tuning conductance-based models: construction and analysis of databases of model neurons. *J Neurophysiol* 90, 3998-4015
- Pruess, H, Derst, C, Lommel, R, Veh, RW (2005). Differential distribution of individual subunits of strongly inwardly rectifying potassium channels (Kir2 family) in rat brain. *Mol Brain Res* 139, 63-79
- Rakic, P (1971). Neuron-glia relationship during granule cell migration in developing cerebellar cortex. A Golgi and electronmicroscopic study in *macacus rhesus*. *J Comp Neurol* 141(3), 283-312
- Rakic, P (1972). Mode of cell migration to the superficial layers of fetal monkey cortex. *J Comp Neurol* 145, 61-84
- Rall, W (1962). Theory of physiological properties of dendrites. *Ann N Y Acad Sci* 96, 1071-1092
- Rall, W (1964). Theoretical significance of dendritic tree for input-output relation. In: Reiss, RF (ed.), *Neural theory and modeling*. Stanford University Press, Stanford, California
- Ramon y Cajal, S (1995). *Histology of the nervous system* (English translation, reprint). Oxford University Press, Oxford
- Represa, A, Ben-Ari, Y (2005). Trophic actions of GABA on neuronal development. *Trends Neurosci* 28(6), 278-283

- Rorig, B, Klaus, G, Sutor, B (1995). Dye coupling between pyramidal neurons in developing rat prefrontal and frontal cortex is reduced by protein kinase A activation and dopamine. *J Neurosci* 15(11), 7386-7400
- Rudolph, M, Destexhe, A (2003). A fast-conducting, stochastic integrative mode for neocortical neurons *in vivo*. *J Neurosci* 23, 2466-2476
- Sah, P (1996). Ca²⁺-activated K⁺ currents in neurones: types, physiological roles and modulation. *Trends Neurosci* 19, 150-154
- Sakmann, B, Neher, E (1984). Patch clamp technique for studying ionic channels in excitable membranes. *Annu Rev Physiol* 46, 455-472
- Schaefer, AT, Helmstaedter, M, Sakmann, B, Korngreen, A (2003). Correction of conductance measurements in non-space-clamped structures: 1. Voltage-gated K⁺ channels. *Biophys J* 84(6), 3508-3528
- Schiller, J, Schiller, Y, Stuart, GJ, Sakmann, B (1997). Calcium action potentials restricted to distal apical dendrites of rat neocortical pyramidal neurons. *J Physiol* 505(3), 605-616
- Schiller, J, Schiller, Y (2001). NMDA receptor-mediated dendritic spikes and coincidence signal amplification. *Curr Opin Neurobiol* 11(3), 343-348
- Shepherd, GMG, Svoboda, K (2005). Laminar and columnar organization of ascending excitatory projections to layer 2/3 pyramidal neurons in rat barrel cortex. *J Neurosci* 25(24), 5670-5679
- Shibasaki, H (1993). Recent advances in non-invasive studies of higher brain functions. *Brain Dev* 15(6), 423-427
- Sholl, DA (1953). Dendritic organization in the neurons of the visual and motor cortices of the cat. *J Anat* 87(4), 387-406
- Sidman, RL, Rakic, P (1973). Neuronal migration, with special reference to developing human brain: a review. *Brain Res* 62(1), 1-35
- Somogyi, P, Klausberger, T (2004). Defined types of cortical interneurone structure space and spike timing in the hippocampus. *J Physiol* 562(1), 9-26
- Squire, LR, Bloom, FE, McConnell, SK, Roberts, JL, Spitzer, NC, Zigmond, MJ (eds.)(2003). *Fundamental Neuroscience* (2nd ed.). Academic Press, London, UK
- Stafstrom, CE, Schwindt, PC, Crill, WE (1982). Negative slope conductance due to a persistent subthreshold sodium current in cat neocortical neurons *in vitro*. *Brain Res* 236(1), 221-226

- Stafstrom, CE, Schwindt, PC, Chubb, MC, Crill, WE (1985). Properties of persistent sodium conductance and calcium conductance of layer V neurons from cat sensorimotor cortex *in vitro*. *J Neurophysiol* 53(1), 153-170
- Stanfield, PR, Nakajima, Y, Yamaguchi, K (1985). Substance P raises neuronal membrane excitability by reducing inward rectification. *Nature* 315(6019), 498-501
- Steriade, M (2001). Impact of network activities on neuronal properties in corticothalamic systems. *J Neurophysiol* 86, 1-39
- Stern, EA, Kincaid, EA, Wilson, CJ (1997). Spontaneous subthreshold membrane potential fluctuations and action potential variability of rat cortico-striatal and striatal neurons *in vivo*. *J Neurophysiol* 77, 1697-1715
- Stosiek, C, Garaschuk, O, Holthoff, K, Konnerth, A (2003). In vivo two-photon calcium imaging of neuronal networks. *PNAS* 100, 7319-7324
- Stuart, GJ, Dodt, HU, Sakmann, B (1993). Patch-clamp recordings from the soma and dendrites of neurons in brain slices using infrared video microscopy. *Pflugers Arch* 423, 511-518
- Stuart, GJ, Sakmann, B (1994). Active propagation of somatic action potentials into neocortical pyramidal cell dendrites. *Nature* 367(6458), 69-72
- Stuart, GJ, Spruston, N, Sakmann, B, Häusser, M (1997). Action potential initiation and backpropagation in neurons of the mammalian CNS. *Trends Neurosci* 20(3), 125-131
- Stuart, GJ, Spruston, N (1998). Determinants of voltage attenuation in neocortical pyramidal neuron dendrites. *J Neurosci* 18(10), 3501-3510
- Sutor, B, Zieglgänsberger, W (1987). A low-voltage activated, transient calcium current is responsible for the time-dependent depolarizing inward rectification of rat neocortical neurons *in vitro*. *Pflugers Arch* 410(1-2), 102-111
- Tan, SS; Gunnensen, J, Job, C (2002). Global gene expression analysis of developing neocortex using SAGE. *Int J Dev Biol* 46, 653-660
- Taylor, CP (1993). Na⁺ channels that fail to inactivate. *Trends Neurosci* 16, 455-460
- Teramae, JN, Fukai, T (2007). Local cortical circuit model inferred from power-law distributed neuronal avalanches. *J Comput Neurosci* 22(3), 301-312

5 References

- Toldi, J, Feher, O, Wolff, JR (1996). Neuronal plasticity induced by neonatal monocular (and binocular) enucleation. *Prog Neurobiol* 48(3), 191-218
- Ungerleider, LG (1995). Functional brain imaging studies of cortical mechanisms for memory. *Science* 270(5237), 769-775
- Vandenberg, CA (1987). Inward rectification of a potassium channel in cardiac ventricular cells depends on internal magnesium ions. *Proc Natl Acad Sci USA* 84, 2560-2564
- Van Drongelen, W, Koch, H, Elsen, FP, Lee, HC, Mrejeru, A, Doren, E, Marcuccilli, CJ, Hereld, M, Stevens, RL, Ramirez, JM (2006). Role of persistent sodium current in bursting activity of mouse neocortical networks *in vitro*. *J Neurophysiol* 96(5), 2564-2577
- Van Drongelen, W, Lee, HC, Stevens, RL, Hereld, M (2007). Propagation of seizure-like activity in a model of neocortex. *J Clin Neurophysiol* 24(2), 182-188
- Vanier, MC, Bower, JM (1999). A comparative survey of automated parameter-search methods for compartmental neural models. *J Comp Neurosci* 7, 149-171
- Wang, HS, Pan, Z, Shi, W, Brown, BS, Wymore, RS, Cohen, IS, Dixon, JE, McKinnon, D (1998). KCNQ2 and KCNQ3 potassium channel subunits: molecular correlates of the M-channel. *Science* 282, 1890-1893
- Waters, J, Larkum, ME, Sakmann, B, Helmchen, F (2003). Supralinear Ca^{2+} influx into dendritic tufts of layer 2/3 neocortical pyramidal neurons *in vitro* and *in vivo*. *J Neurosci* 23(24), 8558-8567
- Waters, J, Helmchen, F (2004). Boosting of action potential backpropagation by neocortical network activity *in vivo*. *J Neurosci* 24(49), 11127-11136
- Waters, J, Helmchen, F (2006). Background synaptic activity is sparse in neocortex. *J Neurosci* 26(32), 8267-8277
- Weaver, CM, Wearne, SL (2006). The role of action potential shape and parameter constraints in optimization of compartment models. *Neurocomp* 69, 1053-1057
- Wiesel, TN, Hubel, DH (1963). Single cell responses in striate cortex of kittens deprived of vision in one eye. *J Neurophysiol* 26, 1003-1017
- Wiesel, TN (1982). Postnatal development of the visual cortex and the influence of environment. *Nature* 299, 583-591

- Woodbury, DM (1980). Phenytoin: introduction and history. In: Glaser, GH, Penry, JK, Woodbury DM. Antiepileptic drugs: mechanisms of action. Raven Press, New York
- Woolsey, TA, Van der Loos, H (1970). The description of a cortical field composed of discrete cytoarchitectonic units. *Brain Res* 17, 205-242
- Yanagihara, K, Irisawa, H (1980). Inward current activated during hyperpolarization in the rabbit sinoatrial node cell. *Pflügers Archiv* 385, 11-19
- Yang, J, Jan, YN, Jan, LY (1995). Determination of the subunit stoichiometry of an inwardly rectifying potassium channel. *Neuron* 15, 1441-1447
- Yuste, R, Nelson, DA, Rubin, WW, Katz, LC (1995). Neuronal domains in developing neocortex: mechanisms of coactivation. *Neuron* 14, 7-17
- Yuste, R (2005). Origin and classification of neocortical interneurons. *Neuron* 48(4), 524-527
- Zhang, ZW (2004). Maturation of layer V pyramidal neurons in the rat prefrontal cortex: intrinsic properties and synaptic function. *J Neurophysiol* 91, 1171-1182
- Zhou, FM, Hablitz, JJ (1996). Postnatal development of membrane properties of layer I neurons in rat neocortex. *J Neurosci* 16(3), 1131-1139
- Zhu, JJ (2000). Maturation of layer 5 neocortical pyramidal neurons: amplifying salient layer 1 and layer 4 inputs by Ca²⁺ action potentials in adult rat tuft dendrites. *J Physiol* 526(3), 571-587

6 Acknowledgments

Prof. Dr. B. Sakmann, whose persistent support made this work possible and who always stunned me with his sudden eruptions of humor and his comments on the “politische Großwetterlage”

Prof. Dr. F Helmchen for being a continuous source of ideas and his great patience in leading me along this project

Prof. Dr. K.-H. Meier for giving this work a more physical twist

Dr. A. Frick for spending a lot of time reading and commenting on this manuscript

Dr. M. E. Larkum for providing the experimental data for the refined full-morphology model

Dr. Arnd Roth for helping me out with NEURON innumerable times

M. Kaiser for brilliant technical assistance to the verge of actually doing my experiments

R. Granadillo and S. Terbeck for their patience with many paper requests

G. Matthies and G. Dücker for their immense help in my struggles with administrative problems

K. Bauer and W. Kaiser for expert help with all questions concerning computers

Dr. J. Waters, Dr. P. Krieger, M. Wiechert and M. Oberlaender for commenting on the manuscript

Dr. P. Broser, Dr. R. Bruno, Dr. H. Spohrs, Dr. D. Feldmeyer, Dr. A. Nimmerjahn, Dr. V. Wimmer, Dr. J. Kerr, Dr. T. Celikel, A. Groh, T. Hahn, H. S. Meyer, D. Greenberg, E. Resnik, A. Dondzillo, B. Grewe and M. Frey for a lot of fruitful discussions

Dr. B. Kampa, Dr. N. Benhassine, W Goebel, C. Engelbrecht, D. Langer and H. Johannssen for a very productive time in Zürich

my family and Katja for continuous support during all this time

7 List of abbreviations

AHP	after-hyperpolarization
AP	action potential
AR	anomalous rectification
BaCl ₂	barium chloride
Ca ²⁺	calcium ions
C_{AR}	coefficient describing anomalous rectification
Cl ⁻	chloride ions
C_m	specific membrane capacitance
CNS	central nervous system
EPSP	excitatory post-synaptic potential
$E_{rev,X}$	reversal potential of ion species X
F	Faraday's constant
GHK	the Goldman-Hodgkin-Katz equation
HH	Hodgkin-Huxley description of ion channel kinetics
g_x	specific conductance density of channel x
G_x	total conductance of channel x
I _h	hyperpolarization-activated current
IPSP	inhibitory post-synaptic potential
K ⁺	potassium ions
KIR	inward rectifying potassium (channel)
Na ⁺	sodium ions
PSP	post-synaptic potential
R	universal gas constant
R_{in}	input resistance
T	absolute temperature
TTX	tetrodotoxin
V	voltage
V_{AHP}	amplitude of AHP relative to V_{thresh}
V_{amp}	AP amplitude relative to V_{thresh}
V_m	membrane potential
V_{rest}	resting membrane potential
V_{thresh}	threshold membrane potential for eliciting an AP
$[X]_i$	intracellular concentration of ion species X
$[X]_o$	extracellular concentration of ion species X
ZD7288	4-(<i>N</i> -ethyl- <i>N</i> -phenylamino)-1,2-dimethyl-6-(methylamino) pyridinium chloride